

2005

Experimental validation of the angle-of-arrival estimation capabilities of a four-arm spiral antenna

Joshua Stephen Radcliffe
University of Dayton

Follow this and additional works at: https://ecommons.udayton.edu/graduate_theses

Recommended Citation

Radcliffe, Joshua Stephen, "Experimental validation of the angle-of-arrival estimation capabilities of a four-arm spiral antenna" (2005). *Graduate Theses and Dissertations*. 5063.
https://ecommons.udayton.edu/graduate_theses/5063

This Thesis is brought to you for free and open access by the Theses and Dissertations at eCommons. It has been accepted for inclusion in Graduate Theses and Dissertations by an authorized administrator of eCommons. For more information, please contact mschlange1@udayton.edu, ecommons@udayton.edu.

**Experimental Validation of the Angle-of-Arrival Estimation
Capabilities of a Four-arm Spiral Antenna**

THESIS

Submitted to

**The School of Engineering of the
UNIVERSITY OF DAYTON**

**In Partial Fulfillment of the Requirements for
The Degree
Master of Science in Electrical Engineering**

Joshua Stephen Radcliffe

UNIVERSITY OF DAYTON


Dayton, Ohio


December 2005

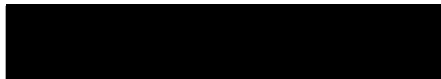
EXPERIMENTAL VALIDATION OF THE ANGLE-OF-ARRIVAL ESTIMATION
CAPABILITIES OF A FOUR-ARM SPIRAL ANTENNA


APPROVED BY:

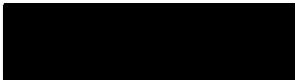
*Heckman -
Please Do Not
Remove This Note!
original*

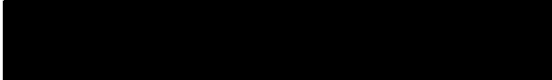

Krishna M. Pasala, Ph.D.
Advisory Committee Chairman
Professor, Electrical and
Computer Engineering Department


Robert P. Penno, Ph.D.
Committee Member
Associate Professor, Electrical and
Computer Engineering Department


Gary A. Thiele, Ph.D.
Committee Member
Professor Emeritus, Electrical and
Computer Engineering Department


Stephen W. Schneider, Ph.D.
Committee Member
Principle Engineer, Sensors
Directorate of the Air Force
Research Laboratory


Donald L. Moon, Ph.D.
Associate Dean
Graduate Engineering Programs & Research
School of Engineering


Joseph E. Saliba, Ph.D., P.E.
Dean, School of Engineering

Abstract

EXPERIMENTAL VALIDATION OF THE ANGLE-OF-ARRIVAL ESTIMATION
CAPABILITIES OF A FOUR-ARM SPIRAL ANTENNA

Radcliffe, Joshua Stephen

University of Dayton

Advisor: Dr. Krishna Pasala

There are presently two types of existing direction finding systems: wideband multi-mode antennas and interferometers. Wideband multi-mode systems allow for a large bandwidth but present a low resolution and high variance. Interferometers provide high accuracy and low variance but are narrow band and require a large number of single aperture antenna elements. A direction finding system enhancement is desirable—one that brings high accuracy (high resolution and low variance) but can perform over a wide range of frequencies. This thesis provides the groundwork for the formation of such a new direction finding system by presenting the results of extensive wideband measurements carried out on two four-arm spiral antennas and the associated modeformer. These measurements are used to assess and validate the angle estimation capability of the multi-arm spiral antenna using the comparison method.

Acknowledgements

This work is humbly dedicated to:

Mr. Todd A. Kastle
Dr. Krishna M. Pasala
Dr. Robert P. Penno
Dr. Stephen W. Schneider

Four brilliant men whose generous investment in my life as a professional and as an individual has been invaluable.

“As iron sharpens iron, so one man sharpens another.” -Proverbs 27:17

Special thanks to Mr. Ken Coss who worked hard daily to setup and take down the rigorous testbody measurement equipment in the compact range. Special thanks also to Mr. Jim Mudd and Dr. Dan Janning whose daily conversations, advice, and wisdom was very helpful in this work. Thanks to Mr. Michael “Cub” Corwin for his efforts in running and troubleshooting code to run angle estimation experiments. This research would not have been nearly as successful if it weren’t for the aid of these individuals.

Table of Contents

Abstract.....	iii
Acknowledgements.....	iv
Table of Contents.....	v
List of Illustrations.....	vii
List of Tables.....	xiii
I Introduction.....	1
1.1 Background and Motivation.....	1
1.2 Scope.....	4
II Theory of Angle Estimation.....	5
2.1 The Multi-arm Spiral Antenna.....	5
2.1.1 Frequency Independence.....	5
2.1.2 Radiation of Multi-arm Spirals.....	9
2.1.3 Multi-arm Multi-mode Spirals.....	13
2.2 Angle Estimation Techniques.....	16
2.2.1 Interferometry.....	16
2.2.2 Multi-mode Spiral Antennas.....	20
III Four-arm Spiral Measurements.....	22
3.1 Setup.....	22
3.2 4-arm Spiral Measurements.....	26
3.2.1 Azimuth Measurements.....	26
3.2.2 Elevation Measurements.....	49
IV Results.....	67
4.1 Calibration.....	67
4.2 Monte Carlo Azimuth Experimentation.....	70
4.2.1 Azimuth Experiment # 1.....	71

Table of Contents

(Continued)

4.2.2	Azimuth Experiment # 2.....	78
4.2.3	Azimuth Experiment # 3.....	80
4.3	Monte Carlo Elevation Experimentation.....	85
4.2.1	Elevation Experiment # 1.....	89
V	Conclusions.....	126
	Bibliography.....	131

List of Illustrations

2.1	Planar equiangular spiral geometry.....	7
2.2	Planar Archimedean Spiral Geometry.....	8
2.3	A self-complementary structure.....	9
2.4	Determining the active region of an N-arm spiral antenna.....	10
2.5	magnitude patterns for a 4-arm spiral antenna in the elevation plane.....	14
2.6	Modal phase patterns for a 4-arm spiral antenna in the azimuth plane with phase compensation.....	14
2.7	Modal phase versus azimuth, no compensation.....	15
2.8	Modal phase versus azimuth with phase compensation.....	16
2.9	Configuration of a basic interferometer baseline.....	17
2.10	Determining AoA for a single baseline.....	17
2.11	Improving AoA accuracy of estimates in interferometry.....	19
2.12	Typical interferometer “antenna farm”.....	19
2.13	Plane wave illumination of an N-arm spiral antenna.....	21
3.1	a) picture of the range and (b) RASCAL range set up.....	24
3.2	One of two identical 4-arm spiral antennas used in this validation.....	25
3.3	(a) Picture of the “almond” test body with encased spiral antenna in RASCAL and (b) the diagram of the test body.....	26
3.4	Spiral azimuth measurement setup in RASCAL.....	27
3.5	Azimuth data for all modes for antenna 1 at an elevation angle of 20° at 4GHz...28	
3.6	Azimuth data for all modes for antenna 1 at an elevation angle of 40° at 4GHz...29	
3.7	Azimuth data for all modes for antenna 1 at an elevation angle of 45° at 4GHz...30	
3.8	Azimuth data for all modes for antenna 2 at an elevation angle of 20° at 4GHz...31	
3.9	Azimuth data for all modes for antenna 2 at an elevation angle of 40° at 4GHz...32	
3.10	Azimuth data for all modes for antenna 2 at an elevation angle of 45° at 4GHz...33	

List of Illustrations
(Continued)

3.11	Azimuth data for all modes for antenna 1 at an elevation angle of 20° at 8GHz...	34
3.12	Azimuth data for all modes for antenna 1 at an elevation angle of 40° at 8GHz...	35
3.13	Azimuth data for all modes for antenna 1 at an elevation angle of 45° at 8GHz...	36
3.14	Azimuth data for all modes for antenna 2 at an elevation angle of 20° at 8GHz...	37
3.15	Azimuth data for all modes for antenna 2 at an elevation angle of 40° at 8GHz...	38
3.16	Azimuth data for all modes for antenna 2 at an elevation angle of 45° at 8GHz...	39
3.17	Azimuth data for both spirals, mode 1 at an elevation angle of 20° at 12GHz.....	40
3.18	Azimuth data for both spirals, mode 2 at an elevation angle of 40° at 12GHz.....	41
3.19	Azimuth data for both spirals, mode 3 at an elevation angle of 45° at 12GHz.....	42
3.20	Azimuth data, all modes for antenna 1 at an elevation angle of 20° at 12GHz.....	43
3.21	Azimuth data, all modes for antenna 1 at an elevation angle of 40° at 12GHz.....	44
3.22	Azimuth data, all modes for antenna 1 at an elevation angle of 45° at 12GHz.....	45
3.23	Azimuth data, all modes for antenna 2 at an elevation angle of 20° at 12GHz.....	46
3.24	Azimuth data, all modes for antenna 2 at an elevation angle of 40° at 12GHz.....	47
3.25	Azimuth data, all modes for antenna 2 at an elevation angle of 45° at 12GHz.....	48
3.26	Spiral elevation measurement setup in RASCAL.....	49
3.27	Elevation cut at mode 1 for both spiral antennas at 4GHz.....	50
3.28	Elevation cut at mode 2 for both spiral antennas at 4GHz.....	51
3.29	Elevation cut at mode 3 for both spiral antennas at 4GHz.....	52
3.30	Elevation cut at mode 1 for both spiral antennas at 8GHz.....	53
3.31	Elevation cut at mode 2 for both spiral antennas at 8GHz.....	54
3.32	Elevation cut at mode 3 for both spiral antennas at 8GHz.....	55
3.33	Elevation cut at mode 1 for both spiral antennas at 12GHz.....	56
3.34	Elevation cut at mode 2 for both spiral antennas at 12GHz.....	57
3.35	Elevation cut at mode 3 for both spiral antennas at 12GHz.....	58
3.36	Elevation cut patterns for antenna 1, all modes at 8GHz.....	59
3.37	Ratio of Elevation Patterns for Spiral one at 4GHz.....	61

List of Illustrations

(Continued)

3.38	Ratio of Elevation Patterns for Spiral one at 8GHz.....	62
3.39	Ratio of Elevation Patterns for Spiral one at 12GHz.....	63
3.40	Ratio of Elevation Patterns for Spiral two at 4GHz.....	64
3.41	Ratio of Elevation Patterns for Spiral two at 8GHz.....	65
3.42	Ratio of Elevation Patterns for Spiral two at 12GHz.....	66
4.1	Calibrated phase data for $\theta = 20^\circ$ at 8GHz.....	69
4.2	SNR vs. # of catastrophic failures for $\theta = 20^\circ$, spiral # 1, at 4GHz.....	72
4.3	SNR vs. # of catastrophic failures for $\theta = 40^\circ$, spiral # 1, at 4GHz.....	72
4.4	SNR vs. # of catastrophic failures for $\theta = 45^\circ$, spiral # 1, at 4GHz.....	73
4.5	SNR vs. # of catastrophic failures for $\theta = 20^\circ$, spiral # 2, at 4GHz.....	73
4.6	SNR vs. # of catastrophic failures for $\theta = 40^\circ$, spiral # 2, at 4GHz.....	74
4.7	SNR vs. # of catastrophic failures for $\theta = 45^\circ$, spiral # 2, at 4GHz.....	74
4.8	SNR vs. # standard deviation for $\theta = 20^\circ$, spiral # 1, at 4GHz.....	75
4.9	SNR vs. # standard deviation for $\theta = 40^\circ$, spiral # 1, at 4GHz.....	75
4.10	SNR vs. # standard deviation for $\theta = 45^\circ$, spiral # 1, at 4GHz.....	76
4.11	SNR vs. # standard deviation for $\theta = 20^\circ$, spiral # 2, at 4GHz.....	76
4.12	SNR vs. # standard deviation for $\theta = 40^\circ$, spiral # 2, at 4GHz.....	77
4.13	SNR vs. # standard deviation for $\theta = 45^\circ$, spiral # 2, at 4GHz.....	77
4.14	Mean of azimuth estimates for spiral # 1 at 4GHz.....	80
4.15	Mean of azimuth estimates for spiral # 1 at 8GHz.....	81
4.16	Mean of azimuth estimates for spiral # 1 at 12GHz.....	81
4.17	Mean of azimuth estimates for spiral # 2 at 4GHz.....	83
4.18	Mean of azimuth estimates for spiral # 2 at 8GHz.....	83
4.19	Mean of azimuth estimates for spiral # 2 at 12GHz.....	84
4.20	Ratio of modal elevation patterns of the form $r = f(\theta)$	87
4.21	Fitted polynomials to each side of the modal ratios of the form $\theta = g(r)$	88
4.22	SNR vs. # of catastrophic failures for $\theta = 20^\circ$, spiral # 1, at 4GHz.....	89

List of Illustrations

(Continued)

4.23	SNR vs. # of catastrophic failures for $\theta = 20^\circ$, spiral # 1, at 8GHz.....	90
4.24	SNR vs. # of catastrophic failures for $\theta = 20^\circ$, spiral # 1, at 12GHz.....	90
4.25	SNR vs. # of catastrophic failures for $\theta = 30^\circ$, spiral # 1, at 4GHz.....	91
4.26	SNR vs. # of catastrophic failures for $\theta = 30^\circ$, spiral # 1, at 8GHz.....	91
4.27	SNR vs. # of catastrophic failures for $\theta = 30^\circ$, spiral # 1, at 12GHz.....	92
4.28	SNR vs. # of catastrophic failures for $\theta = 40^\circ$, spiral # 1, at 4GHz.....	92
4.29	SNR vs. # of catastrophic failures for $\theta = 40^\circ$, spiral # 1, at 8GHz.....	93
4.30	SNR vs. # of catastrophic failures for $\theta = 40^\circ$, spiral # 1, at 12GHz.....	93
4.31	SNR vs. # of catastrophic failures for $\theta = 50^\circ$, spiral # 1, at 4GHz.....	94
4.32	SNR vs. # of catastrophic failures for $\theta = 50^\circ$, spiral # 1, at 8GHz.....	94
4.33	SNR vs. # of catastrophic failures for $\theta = 50^\circ$, spiral # 1, at 12GHz.....	95
4.34	SNR vs. # of catastrophic failures for $\theta = 60^\circ$, spiral # 1, at 4GHz.....	95
4.35	SNR vs. # of catastrophic failures for $\theta = 60^\circ$, spiral # 1, at 8GHz.....	96
4.36	SNR vs. # of catastrophic failures for $\theta = 60^\circ$, spiral # 1, at 12GHz.....	96
4.37	SNR vs. standard deviation for $\theta = 20^\circ$, spiral # 1, at 4GHz.....	98
4.38	SNR vs. standard deviation for $\theta = 20^\circ$, spiral # 1, at 8GHz.....	98
4.39	SNR vs. standard deviation for $\theta = 20^\circ$, spiral # 1, at 12GHz.....	99
4.40	SNR vs. standard deviation for $\theta = 30^\circ$, spiral # 1, at 4GHz.....	99
4.41	SNR vs. standard deviation for $\theta = 30^\circ$, spiral # 1, at 8GHz.....	100
4.42	SNR vs. standard deviation for $\theta = 30^\circ$, spiral # 1, at 12GHz.....	100
4.43	SNR vs. standard deviation for $\theta = 40^\circ$, spiral # 1, at 4GHz.....	101
4.44	SNR vs. standard deviation for $\theta = 40^\circ$, spiral # 1, at 8GHz.....	101
4.45	SNR vs. standard deviation for $\theta = 40^\circ$, spiral # 1, at 12GHz.....	102
4.46	SNR vs. standard deviation for $\theta = 50^\circ$, spiral # 1, at 4GHz.....	102
4.47	SNR vs. standard deviation for $\theta = 50^\circ$, spiral # 1, at 8GHz.....	103
4.48	SNR vs. standard deviation for $\theta = 50^\circ$, spiral # 1, at 12GHz.....	103
4.49	SNR vs. standard deviation for $\theta = 60^\circ$, spiral # 1, at 4GHz.....	104

List of Illustrations

(Continued)

4.50	SNR vs. standard deviation for $\theta = 60^\circ$, spiral # 1, at 8GHz.....	104
4.51	SNR vs. standard deviation for $\theta = 60^\circ$, spiral # 1, at 12GHz.....	105
4.52	SNR vs. # of catastrophic failures for $\theta = 10^\circ$, spiral # 1, at 4GHz.....	106
4.53	SNR vs. # of catastrophic failures for $\theta = 10^\circ$, spiral # 1, at 8GHz.....	107
4.54	SNR vs. # of catastrophic failures for $\theta = 10^\circ$, spiral # 1, at 12GHz.....	107
4.55	SNR vs. # of catastrophic failures for $\theta = 5^\circ$, spiral # 1, at 4GHz.....	108
4.56	SNR vs. # of catastrophic failures for $\theta = 5^\circ$, spiral # 1, at 8GHz.....	108
4.57	SNR vs. # of catastrophic failures for $\theta = 5^\circ$, spiral # 1, at 12GHz.....	109
4.58	SNR vs. # of catastrophic failures for $\theta = 0^\circ$, spiral # 1, at 4GHz.....	109
4.59	SNR vs. # of catastrophic failures for $\theta = 0^\circ$, spiral # 1, at 8GHz.....	110
4.60	SNR vs. # of catastrophic failures for $\theta = 0^\circ$, spiral # 1, at 12GHz.....	110
4.61	SNR vs. standard deviation for $\theta = 10^\circ$, spiral # 1, at 4GHz.....	111
4.62	SNR vs. standard deviation for $\theta = 10^\circ$, spiral # 1, at 8GHz.....	111
4.63	SNR vs. standard deviation for $\theta = 10^\circ$, spiral # 1, at 12GHz.....	112
4.64	SNR vs. standard deviation for $\theta = 5^\circ$, spiral # 1, at 4GHz.....	112
4.65	SNR vs. standard deviation for $\theta = 5^\circ$, spiral # 1, at 8GHz.....	113
4.66	SNR vs. standard deviation for $\theta = 5^\circ$, spiral # 1, at 12GHz.....	113
4.67	SNR vs. standard deviation for $\theta = 0^\circ$, spiral # 1, at 4GHz.....	114
4.68	SNR vs. standard deviation for $\theta = 0^\circ$, spiral # 1, at 8GHz.....	114
4.69	SNR vs. standard deviation for $\theta = 0^\circ$, spiral # 1, at 12GHz.....	115
4.70	SNR vs. # of catastrophic failures for $\theta = 70^\circ$, spiral # 1, at 4GHz.....	116
4.71	SNR vs. # of catastrophic failures for $\theta = 70^\circ$, spiral # 1, at 8GHz.....	116
4.72	SNR vs. # of catastrophic failures for $\theta = 70^\circ$, spiral # 1, at 12GHz.....	117
4.73	SNR vs. # of catastrophic failures for $\theta = 75^\circ$, spiral # 1, at 4GHz.....	117
4.74	SNR vs. # of catastrophic failures for $\theta = 75^\circ$, spiral # 1, at 8GHz.....	118
4.75	SNR vs. # of catastrophic failures for $\theta = 75^\circ$, spiral # 1, at 12GHz.....	118
4.76	SNR vs. # of catastrophic failures for $\theta = 80^\circ$, spiral # 1, at 4GHz.....	119

List of Illustrations

(Continued)

4.77	SNR vs. # of catastrophic failures for $\theta = 80^\circ$, spiral # 1, at 8GHz.....	119
4.78	SNR vs. # of catastrophic failures for $\theta = 80^\circ$, spiral # 1, at 12GHz.....	120
4.79	SNR vs. standard deviation for $\theta = 70^\circ$, spiral # 1, at 4GHz.....	120
4.80	SNR vs. standard deviation for $\theta = 70^\circ$, spiral # 1, at 8GHz.....	121
4.81	SNR vs. standard deviation for $\theta = 70^\circ$, spiral # 1, at 12GHz.....	121
4.82	SNR vs. standard deviation for $\theta = 75^\circ$, spiral # 1, at 4GHz.....	122
4.83	SNR vs. standard deviation for $\theta = 75^\circ$, spiral # 1, at 8GHz.....	122
4.84	SNR vs. standard deviation for $\theta = 75^\circ$, spiral # 1, at 12GHz.....	123
4.85	SNR vs. standard deviation for $\theta = 80^\circ$, spiral # 1, at 4GHz.....	123
4.86	SNR vs. standard deviation for $\theta = 80^\circ$, spiral # 1, at 8GHz.....	124
4.87	SNR vs. standard deviation for $\theta = 80^\circ$, spiral # 1, at 12GHz.....	124

List of Tables

4.1	Azimuth Experiment #2 statistics for spiral #1.....	79
4.2	Azimuth Experiment #2 statistics for spiral #2.....	79
4.3	Azimuth Experiment #3 average bias for spiral #1.....	82
4.4	Azimuth Experiment #3 average bias for spiral #2.....	84

CHAPTER I

INTRODUCTION

1.1 Background and Motivation

Direction Finding (DF) has been an important survival skill of human history, though few have probably given much consideration to the concept. Direction finding is traditionally defined as the ability to locate the angle-of-arrival (AoA) of a distant emitter source. Our human eyes detect radiation from only a small frequency band of the electromagnetic spectrum; however, this propagating radiation, the visible spectrum, holds a vast quantity of information used by each one of us moment by moment. Our keen optical system and associated processing unit tells us the intensity, direction of the source, and the spectral dispensation of the incoming light—thus allowing us to determine wonderful or perilous environments, recognize objects and people, and orienteer our way through the day.

Analogous to our eyes, our ears detect and filter aural radiation. The dual antenna system God created us with is an extraordinary, accurate system for estimating the direction of origin of acoustic sources. Our brains can then process these audio signals to provide us with information from quiet settings to loud concerts and from close conversation to distant echoes.

Mankind has long strived to improve upon our God-given DF sensors. From primitive man's first attempt to cup his hands to enhance auditory directivity, acoustic technology has evolved into seismic detection systems and underwater sonar with the ability to identify submerged vessels over miles of ocean. Galileo invented the first telescope in 1609; he was the first human to view the surface of the moon, he discovered moons orbiting Jupiter and he discovered what later came to be known as Saturn's rings. English Physicist Michael Faraday first demonstrated the phenomenon of electromagnetism in 1831 with an experiment consisting of a magnet and a coil of copper

wire: by moving the magnet towards the coil of wire, an electric current started up in the wire; when he held the magnet still, the current stopped. Faraday demonstrated that electricity was more than just a force moving down a wire; it could also be brought into existence by an invisible force that stretched across empty space generated from a moving magnet. Years later in 1864, Scottish Physicist James Clerk Maxwell proposed the specific behavior of these electromagnetic fields proposed by Faraday, summarized by four differential equations. Heinrich Hertz, a German Physicist, proved the existence of the electromagnetic fields predicted by Maxwell by experimentation in 1887; using sparks between two metal balls, Hertz transmitted invisible waves across a large auditorium and created a spark between two coat hanger wires on the opposite side of the auditorium.

In 1934, fearing the ever increasing clandestine behavior of the Germans, the British government began to investigate possible new military technologies. They approached Robert Watson-Watt, a Scottish Physicist who was the supervisor of a National Radio Research Laboratory in Britain, about the possibility of "death ray" radio wave attacks against impinging bombers. Watson-Watt's response was that death ray attacks were not practical to destroy targets; however, Watson-Watt suggested that radio waves could be bounced off enemy planes to detect them. After a brief demonstration months later, the Radio Detection and Ranging, or radar, system was born. Years later in 1940, it was Watson-Watt's simple radar systems installed along the coastlines of England which gave Britain advanced warning of the invading Germans in the Battle of Britain.

Radar has since advanced in a plethora of areas including weather forecasting, ocean navigation, commercial airline traffic control, and advanced military technology. Direction finding systems for radar application have long been an area of intense research within the Air Force Research Laboratory. In modern avionics applications, it is becoming ever more important to accurately estimate the AoA of a received signal from an airborne platform.

In recent years, a variety of approaches have been investigated to estimate the AoA of a distant emitter source. A few of these methods include interferometry [1], beam-forming techniques [2], and parameter estimation via signal processing techniques

[3-4]. Beam-forming and parameter estimation techniques require increasing amounts of signal processing, making real time angle estimation more of a challenge. However, advances in digital processing technology is making it increasingly more possible to use these techniques that demand greater signal processing abilities. While these systems are complex and the size of the arrays required drives up the cost, reliability and maintainability, they also make it possible to perform more demanding tasks. For example, interferometry fails when multiple targets are present; beam-forming and parameter estimation techniques are designed to identify multiple sources in dense signal environments.

Historically, the lack of computational power coupled with the need for real time estimates made it difficult to use the more sophisticated systems required for beam-forming and parameter estimation techniques. Since at present computational capabilities are increasing at an enormous rate, these techniques are becoming increasingly more practical. However, the cost, size, reliability, and maintainability of these complex systems are constant drawbacks to these direction finding techniques.

Interferometers, the most prevalent DF systems aboard airborne platforms today, provide high accuracy and low variance but are narrow band and require a large number of single aperture antenna elements in order to cover a wide frequency band of operation.

In this multi-faceted trade space, single aperture multi-mode antennas possess a lucid niche—multiple elements are not required, wideband performance is achievable, parameter estimation techniques are still applicable, and the cost of such antennas is relatively low.

A single aperture multi-mode antenna is an attractive solution for use in deriving AoA estimates over a wide bandwidth [5]. More specifically, a multi-arm spiral antenna provides an attractive alternative to this problem. A multi-arm (and thereby multi-mode) spiral antenna possesses frequency independent characteristics including constant pattern, impedance, polarization, and phase center over a wide band of frequencies [6]. A considerable amount of work exists analyzing the multi-arm spiral antenna [6-12]. The frequency independent characteristics of these antennas bolster the feasibility of spiral antennas as an attractive solution in deriving AoA estimates. Utilizing these antennas consists of combining the terminal outputs of the multiple arms into a Butler matrix

“modeformer” and then deriving angle information from the outputs of the modeformer. Comparison of the phase of the modeformer outputs produces an estimate of the azimuth angle of an incoming signal, while the comparison of the magnitude of the modeformer outputs gives an estimate of the elevation angle of an incoming signal. In addition, this single aperture multi-mode spiral antenna is capable of providing AoA estimates over a wide bandwidth.

The objective of this work is to validate, by actual measurements, the angle estimation performance of a four-arm spiral antenna using the “comparison” method. This thesis presents the results of extensive wideband measurements carried out on two four-arm spiral antennas and the associated modeformer. The actual measurements are used to assess and validate the angle estimation capability of the multi-arm spiral antenna over a wide bandwidth. The measurement data, along with synthetic noise, is integrated into a robust algorithm for determining AoA. Statistics from this experimentation are gathered and the AoA determination ability of the four-arm spiral antenna is evaluated. The AoA determination statistics of each of the two four-arm spiral antennas are compared and contrasted.

1.2 Scope

The material in this thesis is organized as follows. Chapter 2 will outline the theory of angle estimation including the theory and performance of spiral antennas, existing DF techniques, and the multi-arm spiral antenna “comparison” angle estimation technique. Chapter 3 will present the actual measurement data obtained for two four-arm spiral antennas and illustrate the congruence and element by element variations between the antennas. Chapter 4 will present the results of azimuth and elevation angle estimation experimentation using the obtained measurement data and compare the angle estimation statistics for both four-arm spiral antennas. Chapter 5 will present the final conclusions of this research.

CHAPTER II

THEORY OF ANGLE ESTIMATION

This chapter will present the theory of frequency independent antennas, multi-arm spiral antennas, and current angle estimation techniques.

2.1 The Multi-arm Spiral Antenna

In 1954, an electrical engineer at Wright-Patterson Air Force Base named Edwin Turner wound the arms of a dipole antenna in the shape of an Archimedean spiral and conducted some experiments. The results that he observed were phenomenal—an antenna that possessed circular polarization, nearly constant impedance, and beamwidth independent of frequency [13]. At that current time, Victor Rumsey, the head of the Antenna Laboratory at the University of Illinois, was already diving into the theory of “frequency independent antennas.” In the following section, we will discuss the frequency independent properties of generic 2-arm spirals before diving into 4-arm spiral characteristics.

2.1.1 Frequency Independence

A multi-arm spiral antenna is defined as any N -arm spiral where N is greater than two. Spiral antennas are identified under the category of frequency independent antennas, which boast constant pattern, impedance, polarization, and phase center over a wide band of frequencies. According to Rumsey, an antenna must satisfy two criteria to be considered frequency independent: the shape of the antenna is determined entirely by angles and the current decreases to zero as the distance from the feed increases [6].

The concept of angular dependence has been well exploited over the past few decades; the basic concepts and theory of spiral antenna designs' angular dependence will be discussed here. Each individual spiral's geometry is represented by governing equations which delineate the shape, and intuitively the performance, of that individual spiral antenna. An equiangular spiral curve is generated by the mathematical equation:

$$r = r_o e^{a\phi} \quad (2.1)$$

Where r_o is the radius of one side of the spiral curve for the angle $\phi = 0$ and a is a constant controlling the flare rate of the spiral, determined by the designer. The value of a is more conveniently represented through an expansion ratio, which describes the increase factor of the radius for one single turn of an equiangular spiral.

$$\epsilon = \frac{r(\phi + 2\pi)}{r(\phi)} = \frac{r_o e^{a(\phi + 2\pi)}}{r_o e^{a\phi}} = e^{a2\pi} \quad (2.2)$$

A planar equiangular spiral displaying these parameters can be conveniently seen in figure 2.1. Note the four edges of the metallic curves are expanding exponentially, as described by equation 2.1.

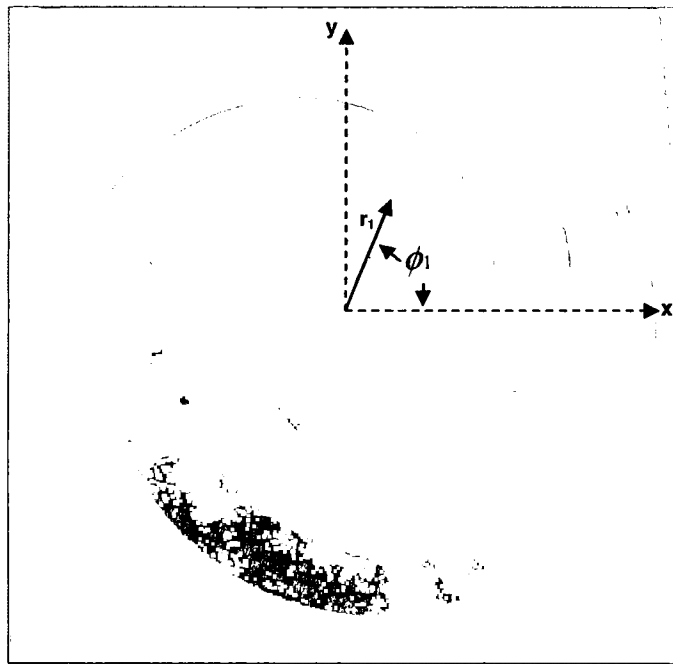


Figure 2.1: Planar equiangular spiral geometry.

The impedance, pattern, and polarization of a planar equiangular spiral antenna remain nearly constant over a wide band of frequencies. Like any spiral, the feed points at the center, the overall radius, and the flare rate, a , affect the overall performance.

Another form of the planar spiral is the Archimedean spiral antenna. This is the spiral type used in testing and measurement for the research contained in this paper. The Archimedean spiral is generated by the equation:

$$r = r_o \phi_o \quad (2.3)$$

As noted in equations 2.1 and 2.3, the Archimedean spiral is linearly proportional to the polar angle rather than exponentially proportional like the equiangular spiral; thus, the Archimedean spiral flares more slowly than the equiangular spiral. Figure 2.2 displays a typical Archimedean spiral antenna.

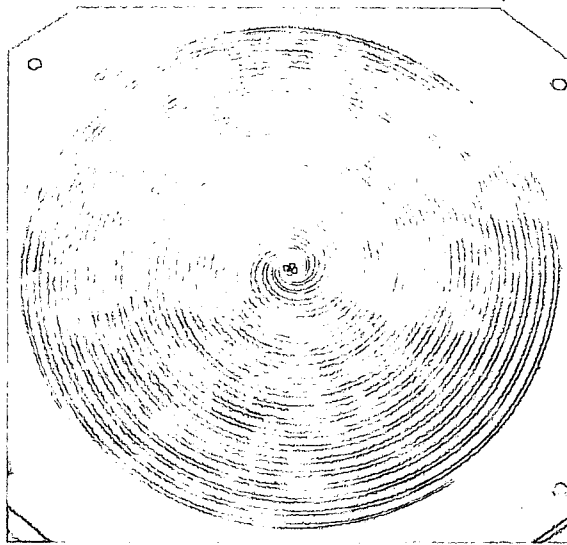


Figure 2.2: Planar Archimedean Spiral Geometry.

It has also been suggested that two additional properties lead to frequency independent behavior and broadband performance: self-complementarity and thicker metal [14]. Self-complementary structures refer to antennas where a dual structure can be formed by replacing metal with air and air with metal. They are specifically identified as those which can be described by the self-complementary property. This precept states that the product of the impedances of an antenna and its own complement is equal to $\eta^2/4$ where η is the intrinsic impedance of free space (using η_0 here assumes that no dielectric or magnetic materials are present). If an antenna is its own complement, frequency independent impedance behavior is achieved. An example of a complementary periodic surface is found in figure 2.3.

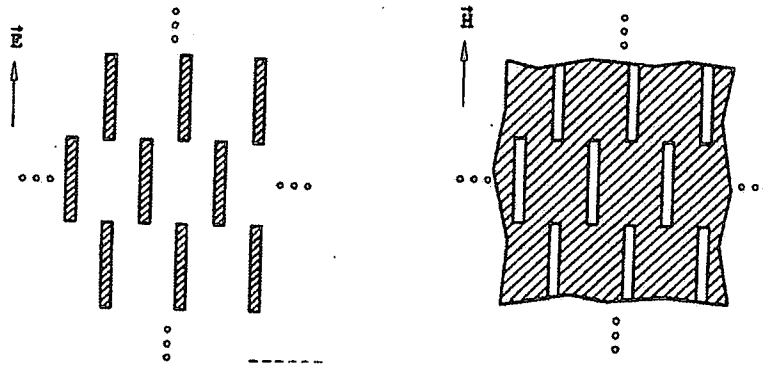


Figure 2.3: A complementary structure.

Increasing the wire diameter or wire thickness of resonant antennas can dramatically increase the bandwidth. Even the increase in wire diameter of a resonant dipole widens its bandwidth significantly. The same is true of multi-arm spirals and like frequency independent antennas—thickening the width of respective feed lines allows for an increase in bandwidth of the antenna.

Another distinguishing feature of frequency independent antennas is their self-scaling behavior. This principle refers to the manner in which these antennas radiate. Spiral antennas in particular have a very unique way of radiating RF energy that is dependent upon wavelength. To a first order, radiation occurs from a circular region on the spiral antenna whose circumference is equal to one wavelength. This so-called “active region” is different for each frequency radiated—as frequency decreases, the active region moves to a larger portion of the antenna and as the frequency increases, the active region moves to a smaller portion of the antenna. The main beam is maximally directed normal to the plane of the antenna at the active region. The frequency independent characteristics of angular dependence and thicker metal yield the utmost liberty in current distribution adjustment over a range of active regions as frequency changes.

2.1.2 Radiation of Multi-arm Spirals

Two-arm spirals produce a “transmission line” mode when the current through the two arms are 180° out of phase, similar to the radiation of a simple dipole. Observing the

behavior of the current as it travels through the arms of this spiral gives us an in-depth look into how spirals radiate and the effect that the phase difference at the feed has on the radiation the spiral. The following equation describes the behavior of the current through a single spiral arm:

$$I(s) = I_0 e^{-j\beta s} \quad (2.4)$$

Here I_0 is the measured initial current at the feed point of the antenna, s is the length along the spiral, and β is the propagation constant, which can also be represented by the quantity $2\pi/\lambda$. As the current progresses along the arm of the spiral, the phase factor will change with location. Though these currents on this spiral are initially out of phase, the relative phase difference between corresponding points on the arms changes as the currents on the arms travel outwards. As a result, regions on the antenna exist where currents are in phase—this is the “active region.”

Consider an N-arm Archimedean spiral with points $P_1, P_2, P_3, \dots, P_N$ which are adjacent to each other on each of the N arms of a spiral antenna at a distance of radius “ r ” from the center of the antenna [15]. The spiral arms are considered to be tightly wound and the separation between adjacent arms, Δr , is given to be negligible. Figure 2.4 below displays this case.

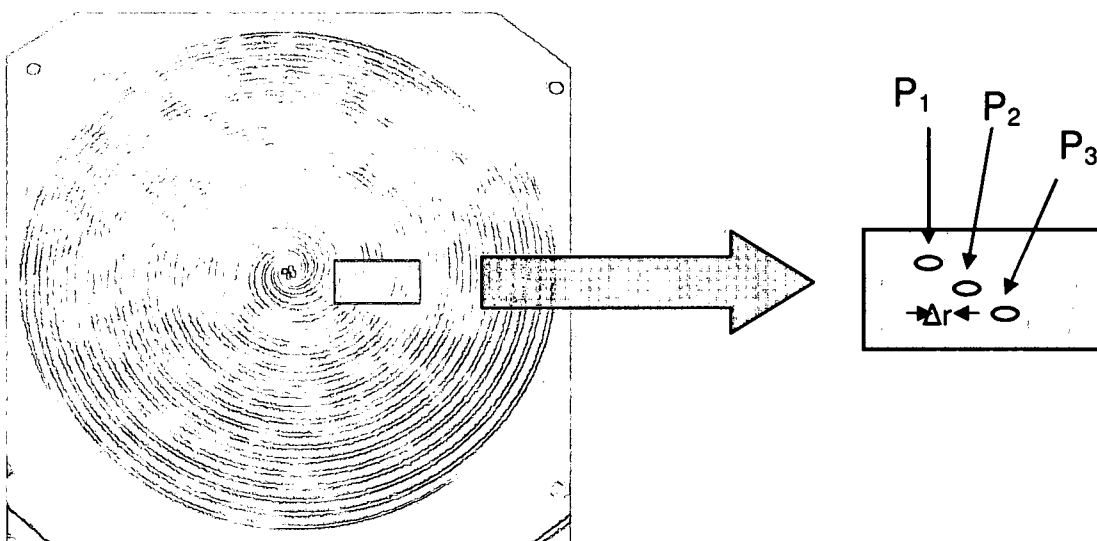


Figure 2.4: Determining the active region of an N-arm spiral antenna.

The difference in length between the points P_1 and P_k on the first and the k^{th} spiral arms is given by:

$$\Delta l = (k-1) \frac{2\pi \cdot r}{N} \quad (2.5)$$

Where N is the total number of spiral arms on the antenna, r is the radius from the center of the antenna, and k is the specific spiral arm in question. Now that we know the difference in length between two points on two adjacent spirals, we can now calculate the phase difference, α , of this specific difference in length between the 1^{st} and k^{th} spiral arms.

$$\Delta \alpha_k = -\beta \Delta l = -\left(\frac{2\pi}{\lambda}\right) \Delta l \quad (2.6)$$

To find the total phase difference between arms including the initial phase of the terminal current, we must find $\Delta \alpha$ at the feeds.

$$\Delta \alpha_{\text{feed}} = \frac{2\pi}{N} (k-1) \quad (2.7)$$

Now we can solve for the total phase difference between spiral arms:

$$\Delta \alpha = \Delta \alpha_k + \Delta \alpha_{\text{feed}} = -\frac{2\pi}{\lambda} (k-1) \frac{2\pi \cdot r}{N} + \frac{2\pi}{N} (k-1) \quad (2.8)$$

$$\Delta \alpha = \frac{2\pi}{N} (k-1) \left[1 - \frac{2\pi}{\lambda} r\right] \quad (2.9)$$

Equation 2.8 puts all the elements together and equation 2.9 simplifies the equation. By looking at the last two equations, it is observed that when $\Delta\alpha$ is zero, there is no phase difference between the two comparable spiral arms—that is, the current of the two arms are in phase. By looking closely at equation 2.9, it is also observed that a simple solution to this case exists:

$$r = \frac{\lambda}{2\pi} \therefore \Delta\alpha = 0 \quad (2.10)$$

When $r = \lambda/2\pi$, the currents of P_1 and P_k are in phase. Therefore, the active region is constituted by a circular region on the multi-arm spiral whose radius is equal to $\lambda/2\pi$, which corresponds to a circumference of λ . Similarly, it is possible to shift the active region outward to a larger circular region by simply changing the initial phase progression of the terminal currents. This is what is referred to as the forming of multi-arm spiral “modes” of operation, or modes of excitation. When the phase progression of the terminal currents is shifted from $2\pi/N$ to $2k\pi/N$, the active region shifts outward to a circular region of circumference $2k\lambda$. Therefore, mode one is defined as the mode of operation in which the terminal current phase progression is $2\pi/N$ and possesses an active region circumference of λ ; mode two is the mode of operation in which the terminal current phase progression is $2*2\pi/N$ and possesses an active region circumference of 2λ ; mode three is the mode of operation in which the terminal current phase progression is $3*2\pi/N$ and possesses an active region circumference of 3λ , and so on. Mode k is attained by phasing the terminal currents to possess a phase progression of $k*2\pi/N$ and boasts a circular active region of circumference $k\lambda$. For an N -arm spiral, N distinct modes of radiation exist; however, it must be noted that each N -arm spiral antenna only boasts $N-1$ usable modes of operation. This is due to the fact that terminal current phase progressions must sum to zero to possess a balanced feed; in mode N , all the arms of a spiral antenna are in phase and do not sum to zero—this creates an unbalanced feed. A balanced feed is defined as a feed where the vector sum of all the individual currents is zero—this allows the feedline radiation to be suppressed.

2.1.3 Multi-arm Multi-mode Spirals

As was discussed in the previous section, frequency independent spiral antennas are not limited to two arms only; adding more arms to a spiral antenna introduces new modes of operation. These different and distinct modes of operation are of great interest in the realm of direction finding and angle estimation. Now that the formation of these modes has been intricately described, let us consider the effects the aforementioned modal formations have on the actual antenna pattern radiated for each modal case.

To attain the proper phase progressions between terminals for specific modes, the spiral is used with a hardware device known as a "modeformer." These phase progressions between the ports of each arm of the spiral antenna create "modal patterns" which are unique from each other, much like the uniqueness of the physical formation of each mode on the antenna. These modal patterns are best described starting from the current in the active region. The current in the active region may be expressed as:

$$I^n(\phi) = I_o^n e^{-jn\phi} \hat{\phi} \quad (2.11)$$

Where:

$$I_o^n = I_o e^{j\psi_n} \quad (2.12)$$

In the above equations, n is the mode number, ϕ is a value in the range of $0 \leq \phi \leq 2\pi$, and ψ is the phase of the active region current at a particular value of ϕ . Notice in equation 2.11 that the current is moving in the ϕ direction. Beginning with this equation modeling the active region current, it is possible to obtain closed-form expressions for the voltages induced at the modeformer output by an incident plane wave that is either θ - or ϕ -polarized [5]. These closed-form expressions are given here:

$$M_\theta^n = E_o e^{j\psi_n} \left(\frac{n\lambda}{2\pi}\right) \pi j^n e^{-jn\phi_o} \times [\cos \theta_o (J_{n-1}(n \sin \theta_o) + J_{n+1}(n \sin \theta_o))] \quad (2.13)$$

$$M_\phi^n = E_o e^{j\psi_n} \left(\frac{n\lambda}{2\pi}\right) \pi j^{n+1} e^{-jn\phi_o} \times [J_{n+1}(n \sin \theta_o) - J_{n-1}(n \sin \theta_o)] \quad (2.14)$$

In the above equations, $J_n(x)$ is a Bessel function of order n . Note that the magnitude of the modal output in both expressions depends only on the elevation angle, θ_o , while the phase of the output depends only upon the azimuth, ϕ_o , and the phase factor, $e^{j\psi}$. Figure 2.5 shows the normalized modal output magnitude variation for a 4-arm spiral antenna and figure 2.6 shows the modal output phase variation.

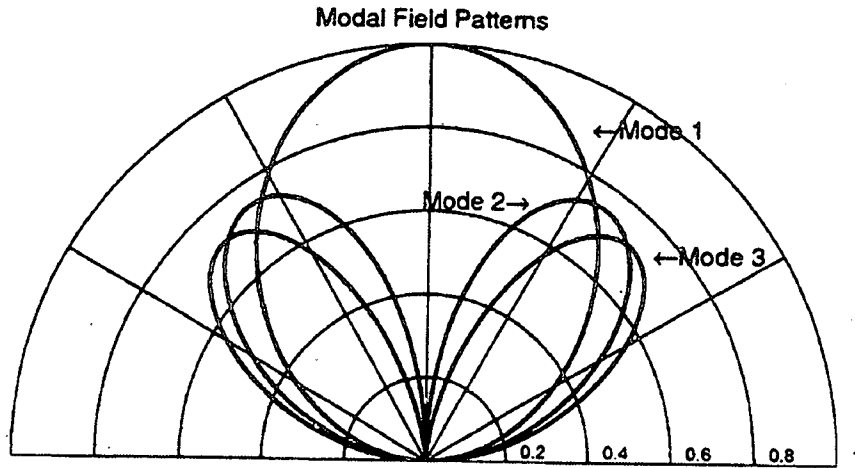


Figure 2.5: Modal magnitude patterns for a 4-arm spiral antenna in the elevation plane.

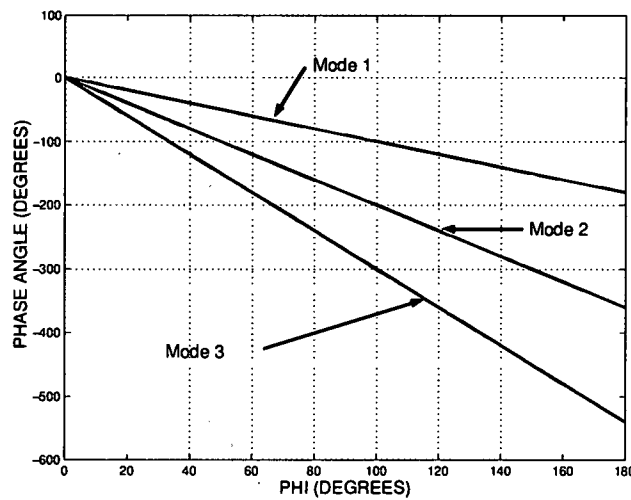


Figure 2.6: Modal phase patterns for a 4-arm spiral antenna in the azimuth plane (with phase compensation).

The elevation patterns produced by a four-arm spiral antenna, as shown in figure 2.5, are constant with azimuth. One could visualize this phenomenon better by rotating the elevation patterns about the z-axis where $\theta = 0^\circ$.

With the aid of a modeformer, any radiation pattern that a spiral produces is a particular vector summation of each of the ports of the antenna. Mode one is known as a sum mode; as observed from figure 2.5, mode one is prominent in the boresight direction with a very wide beam and a high power level. On the contrary, mode two and three are known as difference modes—a null exists at the boresight axis perpendicular to the plane of the spiral, the beam widths are much smaller, and power distribution is angular in nature and much less in quantity than mode one. Notice that as the mode number increases, the beams continue to approach endfire.

Looking back at equation 2.12, the phase of the active region current at $\varphi = 0$, ψ_n , depends upon the mode number, n . As a result, the phase reference of the currents in the active region is not common to all the modes [5]. The phase, ψ_n , depends only upon the geometry of the spiral and the mode number itself. Figure 2.7 shows the relationship between phase and mode number for a 4-arm spiral antenna (three usable modes). The phases with relationship to mode number can be calibrated as part of a calibration process to compensate for different shifts in phase due to antenna geometry. This calibration process is known as phase compensation. These same phases as shown in figure 2.7 are shown after phase compensation in figure 2.8. For both figures, mode one is shown in blue, mode two in red, and mode three in green.

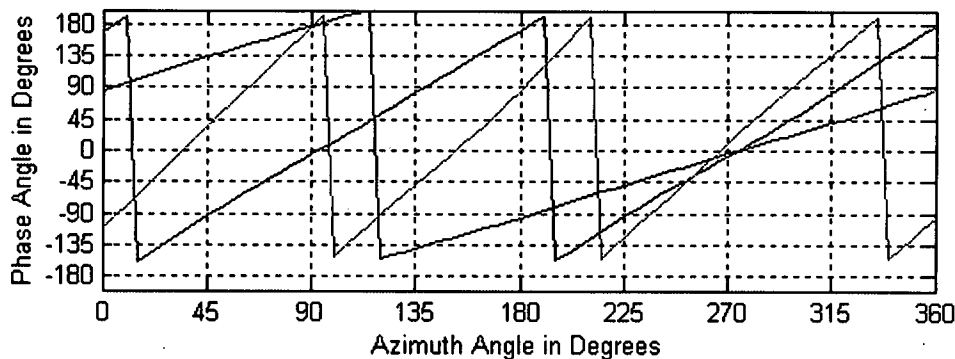


Figure 2.7: Modal phase versus azimuth, no compensation.

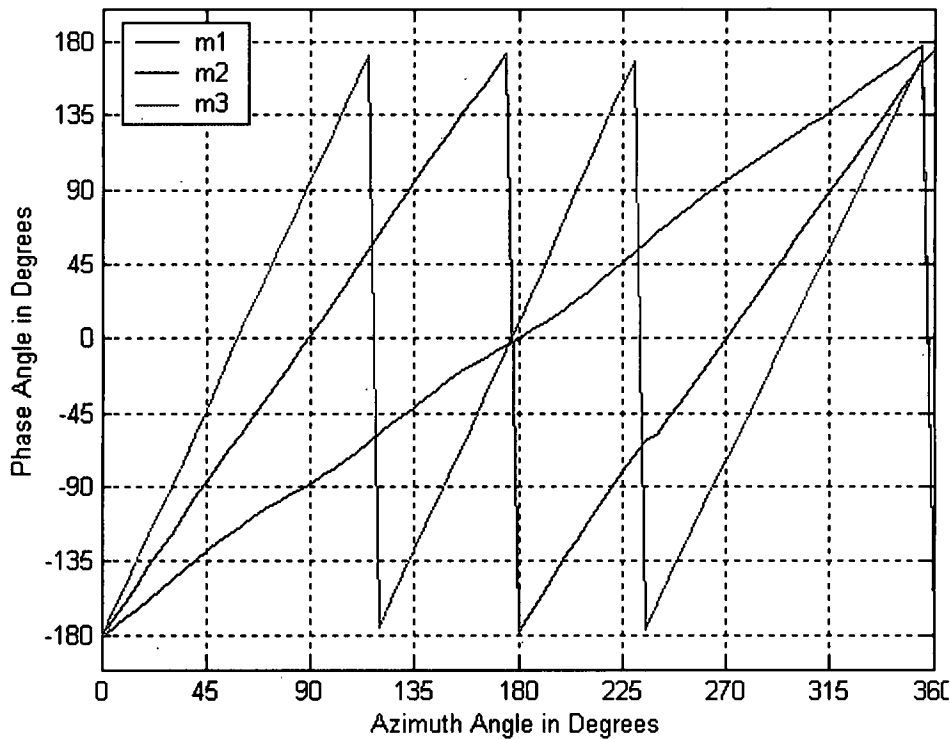


Figure 2.8: Modal phase versus azimuth with phase compensation.

It should be observed that a simple linear relationship exists between the azimuth and the phase of the modeformer outputs after phase compensation. This relationship is to be exploited in order to estimate the AoA of incident radiation.

2.2 Angle Estimation Techniques

Interferometry is the most prevalent of existing angle estimation techniques. This process will be described and discussed in this section along with the multi-mode spiral antenna comparison technique which is being tested in this research.

2.2.1 Interferometry

The most commonly used angle estimation technique in practice is interferometry. The interferometer is a high-accuracy system which determines the emitter location by measuring the AoA along multiple baselines. A baseline is composed of two identical

antennas a known distance apart, two identical receivers, and a phase comparator. Each baseline receives a signal, the phase difference between the two receiving antennas is computed, and the AoA is determined relative to the orientation of the two antennas (the baseline) [16]. The basic configuration of an interferometer baseline is shown in figure 2.9.

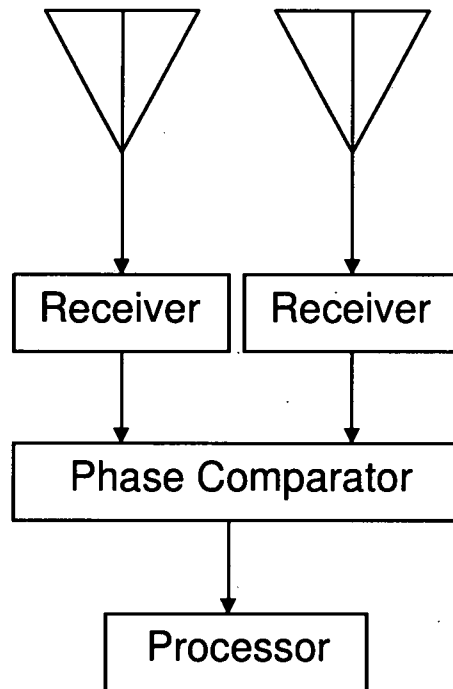


Figure 2.9: Configuration of a basic interferometer baseline.

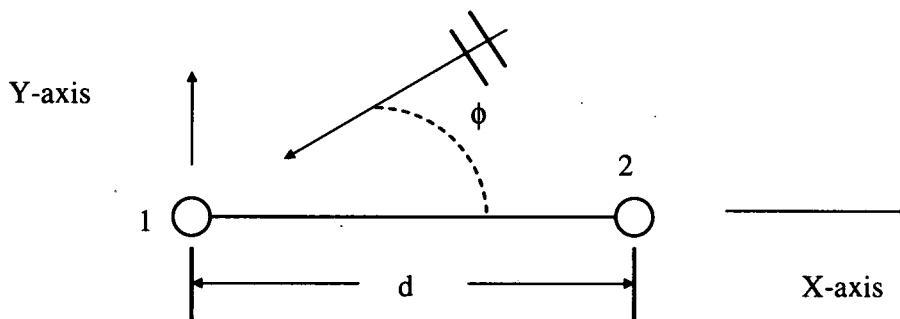


Figure 2.10: Determining AoA for a single baseline.

Figure 2.10 shows the geometry of AoA determination of a single baseline, where an incoming signal is approaching at an angle, ϕ , from the baseline. The value d is one-half of a wavelength and the phase difference between the two antenna elements, ψ , is a simple computation:

$$\psi = \beta \cdot d \cos(\phi) \quad (2.15)$$

In the above equation, β is the known propagation constant, or $2\pi/\lambda$. The AoA can then be calculated by:

$$\phi = \cos^{-1}\left(\frac{\psi}{\beta \cdot d}\right) \quad (2.16)$$

A considerable problem in interferometry is keeping the lengths of the electrical paths through the two antennas and receivers equal. The AoA accuracy of an interferometer system depends on the accuracy of the phase difference measured between the two antennas. This requires cables of exactly the same length from the antennas to the phase comparator for all signal strengths in any environmental setting.

Each baseline within an interferometer system only gains the AoA information for one plane of space; obviously, two planes are required for 3-D coverage. Therefore, an interferometer system must contain at least two baselines to obtain both azimuth and elevation angle estimates.

Also, two antennas per baseline spaced half a wavelength apart provides a very low accuracy of estimates. Therefore, it is profitable to space the two antennas a greater distance apart (approximately 10λ) to achieve a higher accuracy of estimates. However, with this distance between antennas being so electrically large, it causes ambiguities due to the total phase being greater than 2π —it produces multiple AoA estimates. These ambiguous solutions must be discarded in favor of the one correct solution. To resolve the ambiguity, a third antenna element is needed in each baseline a distance of $\lambda/2$ or less from the reference antenna. This electrically short distance between elements allows for a coarse AoA estimate which makes it possible to select the correct solution from the

possibilities available from the long baseline pair. In figure 2.11 below, b represents the short baseline where $b = \lambda/2$ and d is the long baseline where $d \approx 10\lambda$.

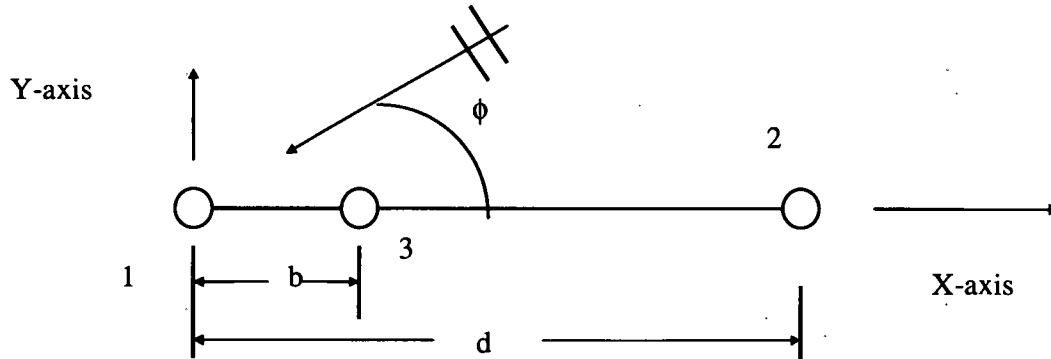


Figure 2.11: Improving AoA accuracy of estimates in interferometry.

This brings our total number of antennas for each baseline to three—a total of five antennas for full 3-D coverage using an interferometer system. This five-element system is known as the Linear Phase Interferometer (LPI). The LPI works well when the long baseline is long enough to provide the required accuracy and the short baseline is electrically short enough to remain unambiguous [17].

A final significant problem with the interferometer method is that each of these baselines is narrowband. It takes numerous LPI's to add bandwidth to the entire system! Each LPI allows for only one frequency band. A full interferometer system can easily contain up to three LPI's which is fifteen antennas or more—an entire “antenna farm.” Figure 2.12 shows the typical setup of a full interferometer DF system used to determine AoA over a wide band of frequencies.

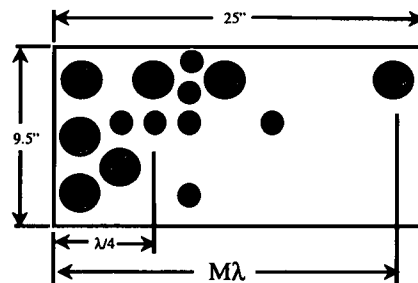


Figure 2.12: Typical interferometer “antenna farm.”

The field-of-vision (FoV) of these interferometers is very limited and several “antenna farms” may be needed on an aircraft to assure coverage on either side, downward, forward, and rearward. Practical considerations such as maintainability, reliability, and application versatility in conjunction with cost, size, and weight make it highly desirable to minimize the number of apertures on the platform that are required to determine AoA [17].

2.2.2 Multi-Mode Spiral Antennas

In the previous section, it is evident that certain disadvantages exist within modern interferometry methods of direction finding which make an alternative solution desirable. A single aperture, multimode antenna is an attractive alternative for deriving accurate AoA estimates over a wide bandwidth [5].

As defined in the previous section, a multimode spiral antenna is defined as any N-arm spiral (where N is greater than two). When used with a hardware device known as a “modeformer”, the terminal outputs of the spiral are phase shifted in designated amounts between each port. These phase progressions between the ports of each arm of the spiral antenna create “modal patterns” which are unique from each other. Figure 2.5 shows these modal patterns for a 4-arm spiral antenna.

By comparing the magnitude of these modal outputs, an estimate of elevation angle (with respect to antenna boresight) is obtained, while comparison of the phase of these modeformer outputs provides an estimate of azimuth. Figure 2.13 shows the plane wave illumination of an N-arm spiral antenna where θ is the elevation and ϕ is azimuth. As shown in the figure, the elevation angle, θ , is measured from the z-axis (boresight) and the azimuth angle, ϕ , is measured counter-clockwise from the x-axis.

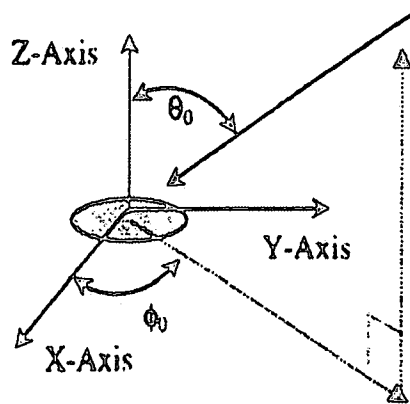


Figure 2.13: Plane wave illumination of an N-arm spiral antenna.

The modeformer concept has long been used with linear or planar arrays of single-mode antennas; here, the modeformer is being applied to a single-aperture antenna. The multi-arm spiral boasts an additional advantage of being frequency independent over a wide band of frequencies because in multi-mode spiral antennas, the electromagnetic characteristics are determined by angular relationships, not lengths or widths. Simply stated, a single multi-mode spiral antenna can give us 3-D spatial coverage (FoV) over a wideband of frequencies.

This “comparison” approach, as it is aptly named, when used with a 4-arm spiral antenna in conjunction with modeformer hardware is adept to provide AoA estimates whose accuracy is comparable to that of two single-mode antennas separated by one-half wavelength (a half-wave interferometer). The prominent catalyst in using a 4-arm spiral instead of a half-wave interferometer is the bandwidth of the AoA estimates; for a 4-arm spiral, these estimates remain constant over the entire band of frequencies for which the spiral antenna is devised.

CHAPTER III

FOUR-ARM SPIRAL MEASUREMENTS

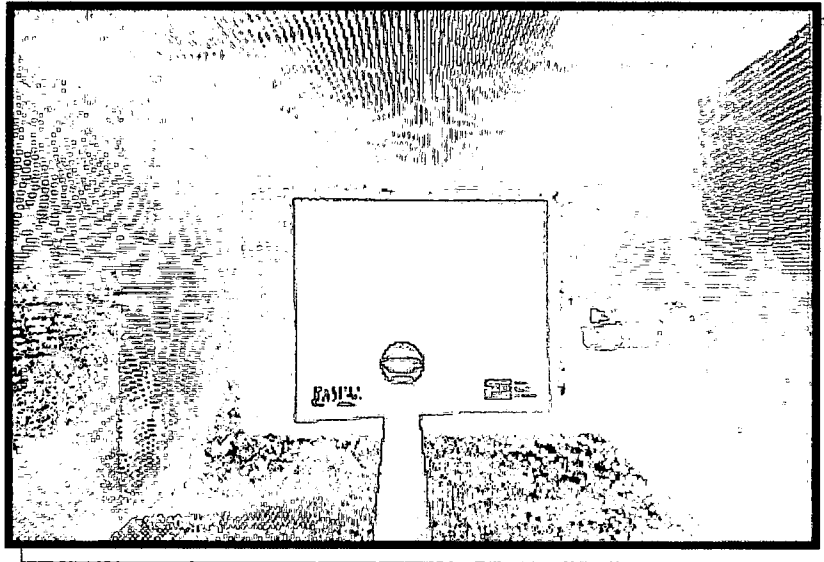
This chapter will present the measurement setup, the measurements performed, and the data from each set of four-arm spiral measurements. The measurement processes will be described in detail accompanied by observations and characteristics of the data obtained in each respective measurement.

3.1 Setup

As stated in the introduction of this work, the objective of this effort is to demonstrate the proposed theory with measured data. All measurements for this effort were performed in the Sensors Directorate's Radiation and Scattering Compact Antenna Laboratory (RASCAL). RASCAL is a compact far-field range used for smaller sized antenna aperture pattern and radar cross section (RCS) measurements. Frequency and axis scans are available for antenna pattern measurements. The range offers a 3' by 4' quiet zone, vertical and horizontal polarization, and a frequency range of 2-18 GHz. The compact range uses a parabolic reflector to create a constant phase front plane wave which then illuminates the antenna under test (AUT) as shown in figure 3.1.

In order to obtain accurate data from each spiral antenna, a phase-stationary test body was used in all 4-arm spiral measurements. When considering a (conformal) antenna in the presence of a conducting surface, one must make a careful evaluation of the performance of that antenna in an appropriate environment. An antenna test body is required to close the distance between a (conformal) antenna host surface and the designer's infinite ground plane model. The "almond" shaped test body owned by RASCAL and used for all 4-arm spiral measurements in this project is a documented,

proven, and patented device for high performance antenna measurements [18]. This "almond" test body incorporates a unique positioning system which provides a phase-stationary antenna aperture center under rotation of both azimuth and elevation. The result is that all 4-arm spiral measurements can be performed with the center of the spiral in a fixed position in the antenna test range incorporated in a test body of high performance with ground plane characteristics.



(a)

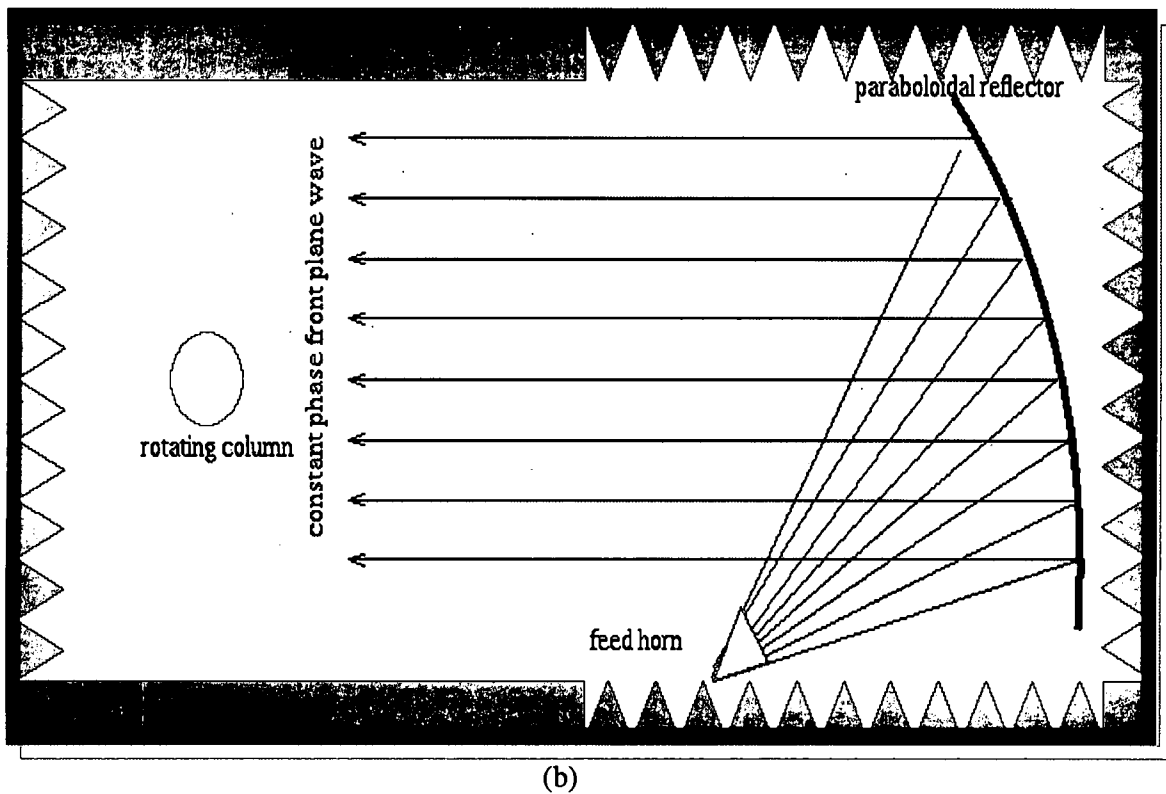


Figure 3.1: (a) picture of the range and (b) RASCAL range set up.

One of the two 4-arm Archimedean spirals under test is shown in figure 3.2. Note the surrounding body and holes made specifically to mount to the “almond” test body. The characterization of the “almond” test body can be noted in figure 3.3 [18]. The “almond” has optimal performance when the pointed tip is directed towards the illuminating field. In figure 3.3, one can note the axes of rotation for both azimuth and elevation. The azimuth rotation involving the “almond” test body is a rotating “can” that spins 360° around the AUT center axis (aperture center of rotation). The elevation rotation is a 90° spin via the septum where the axis of rotation runs through the phase-stationary AUT center point except this axis is orthogonal to the azimuth rotation axis and the axis of symmetry of the test body itself. The septum allows an exiting antenna signal (for an active AUT) from the underside of the test body.

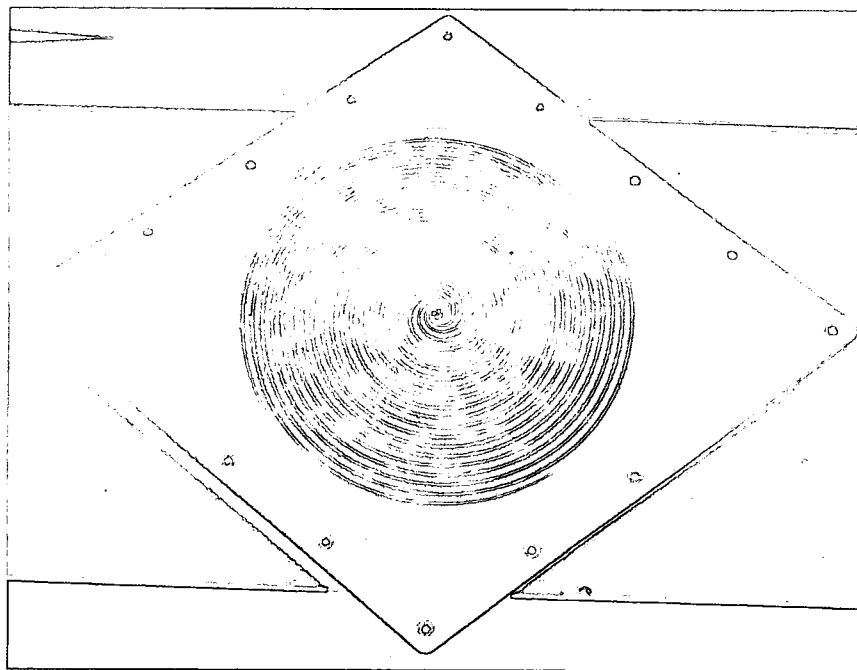
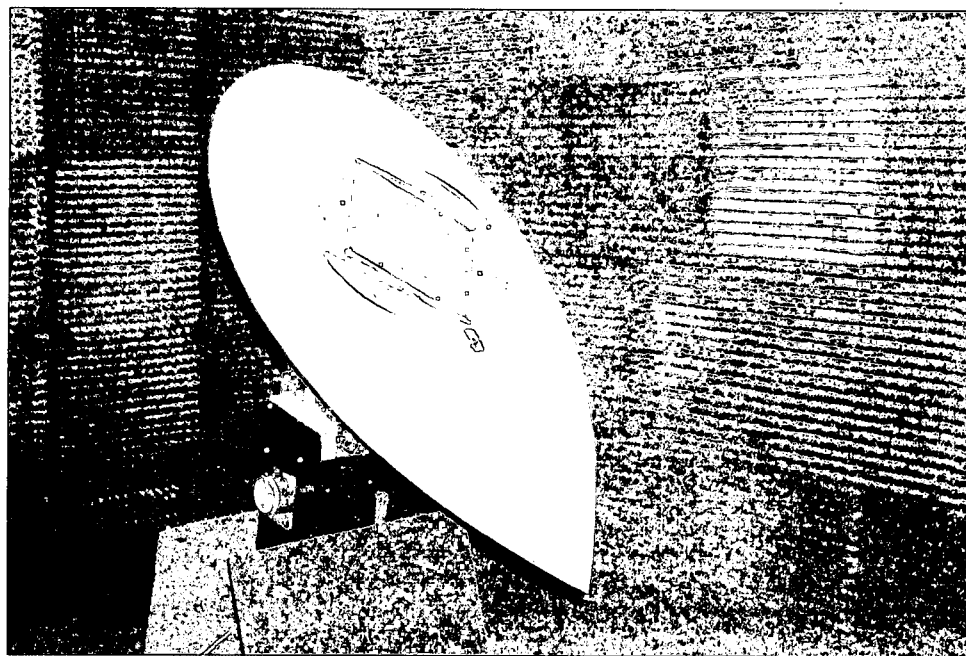
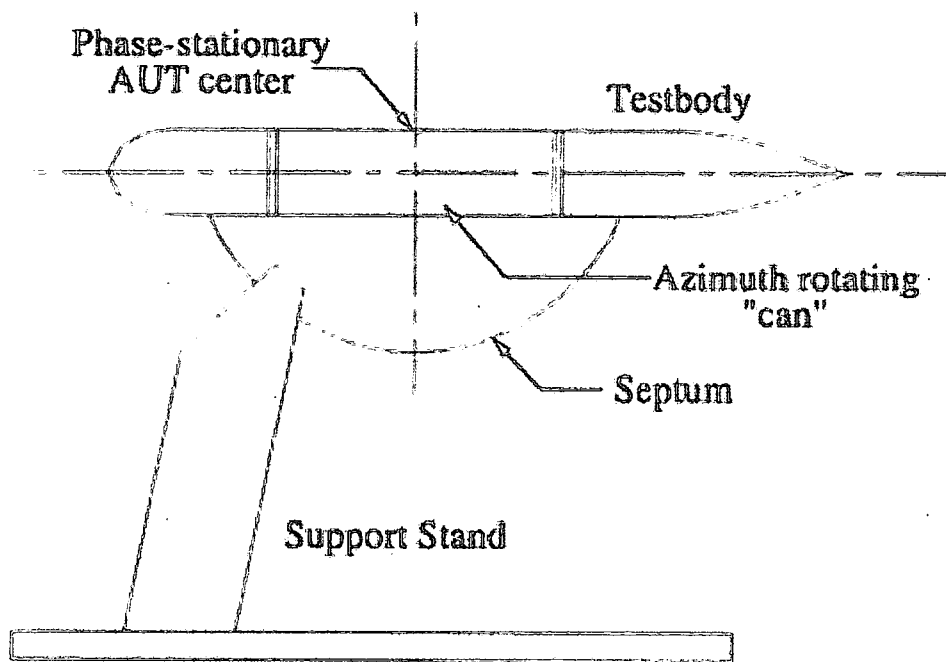


Figure 3.2: One of two identical 4-arm spiral antennas used in this validation.



(a)



(b)

Figure 3.3: (a) Picture of the “almond” test body with encased spiral antenna in RASCAL and (b) the diagram of the test body.

3.2 4-arm Spiral Measurements

In the previous section of this chapter, the measurement setup environment and parameters were described in detail. This section describes the layout, process, and data collected of each specific measurement performed on each of the two 4-arm spiral antennas.

3.2.1 Azimuth Measurements

Obtaining phase data as a function of azimuth is arguably the most important data to be collected for the validation of accurate AoA determination. This 360° azimuth data reveals much information about the multi-mode antenna performance.

The setup for azimuth magnitude and phase data collection is shown in figure 3.4. The axis of rotation of the phase-stationary test body is set up at a specific elevation angle from the parabolic reflector (boresight). As noted, the spiral antenna is then rotated 360° around the axis of symmetry, the ϕ axis, as magnitude and phase data are collected at 5° azimuth increments. This process is repeated for modes 1, 2, and 3 for both 4-arm spiral antennas and was used to collect data at elevation angles of $\theta = 20^\circ, 40^\circ$, and 45° at frequencies of 4-12 GHz. Elevation angles of $\theta = 40^\circ$ and 45° are near the main beam peaks for modes 2 and 3, respectively. We determined the peaks of these modal main beams by performing elevation cuts.

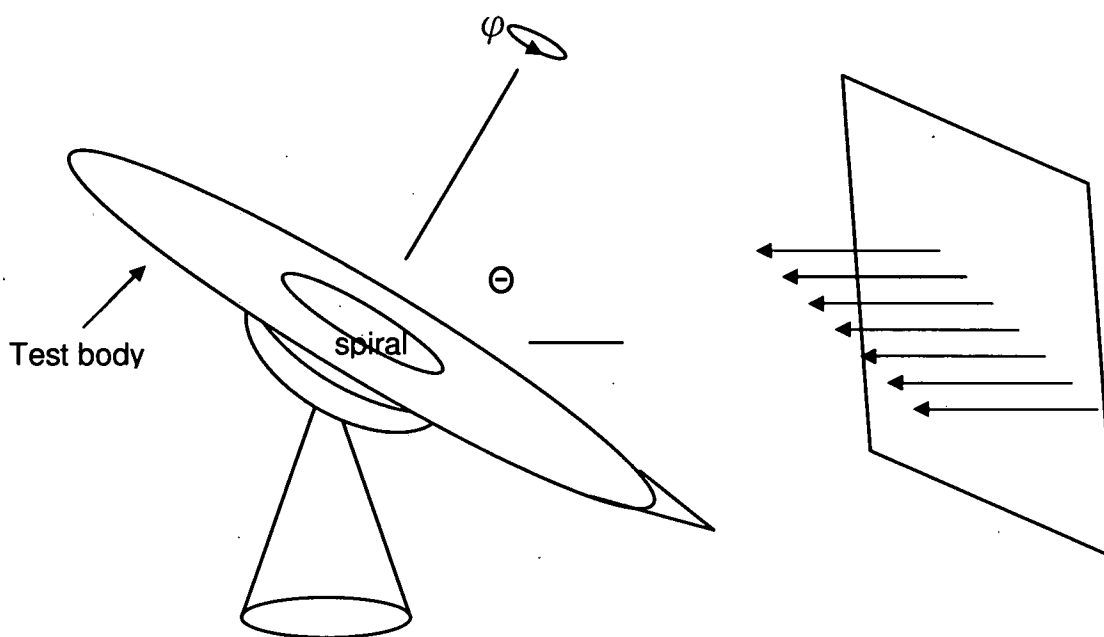


Figure 3.4: Spiral azimuth measurement setup in RASCAL.

Figures 3.5-3.16 illustrate the 4 and 8GHz acquired magnitude and phase data from each mode of the aforementioned azimuth measurements. All data shown corresponds to the case of vertical polarization for all modes of both four-arm spirals. The purpose of this graph setup is to show the change in output as the mode number changes and to demonstrate the element to element differences. Note that the theory presented in chapter 2 calls for the amplitude of the modal outputs to be constant with azimuth; however, in practice this is only approximately true as seen specifically

throughout the actual measured data shown in the figures below. It is also of interest to note the difference in gain levels of the three modes at different elevation angles. As per theory discussed in chapter 2, the phases of the modal outputs vary linearly with azimuth and the slopes are directly related to the corresponding modal numbers. As may be seen from the experimental data, these relationships do hold, though the linearity is not perfect. These imperfections will lead to errors in the angle estimation.

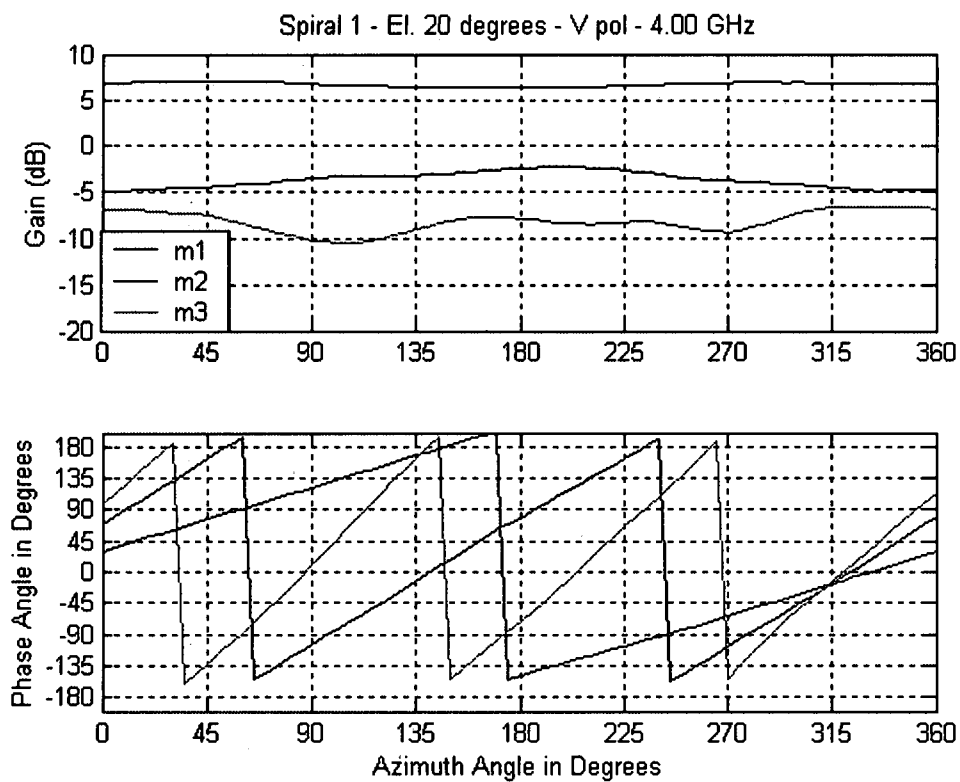


Figure 3.5: All modes for antenna 1 at an elevation angle of 20°.

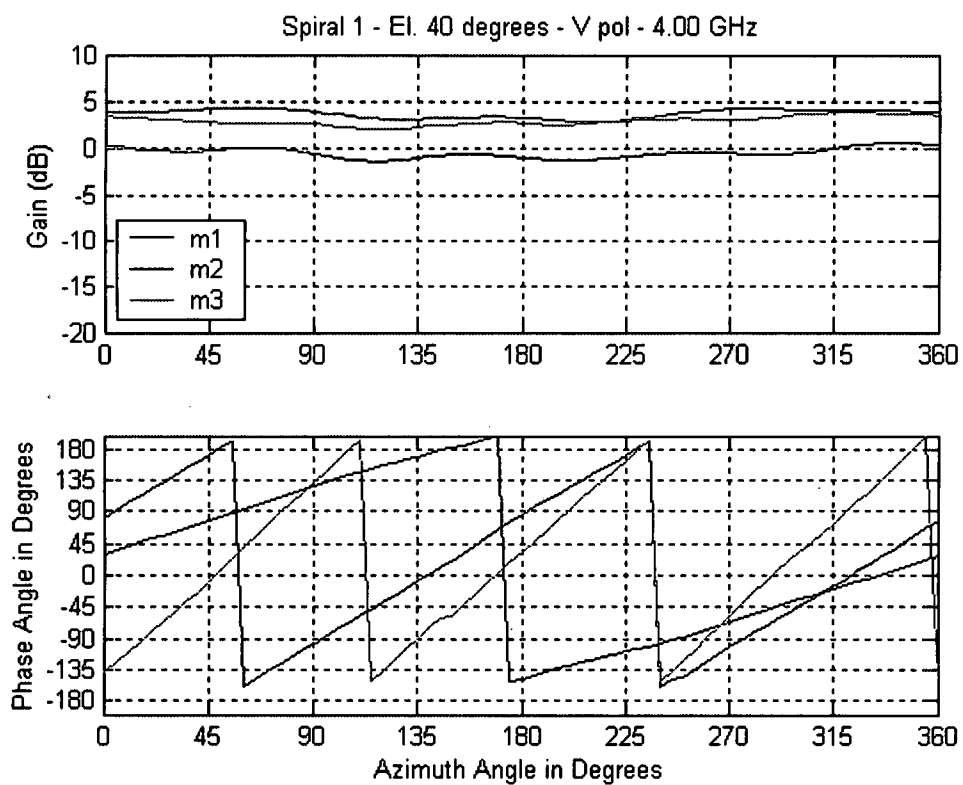


Figure 3.6: All modes for antenna 1 at an elevation angle of 40°.

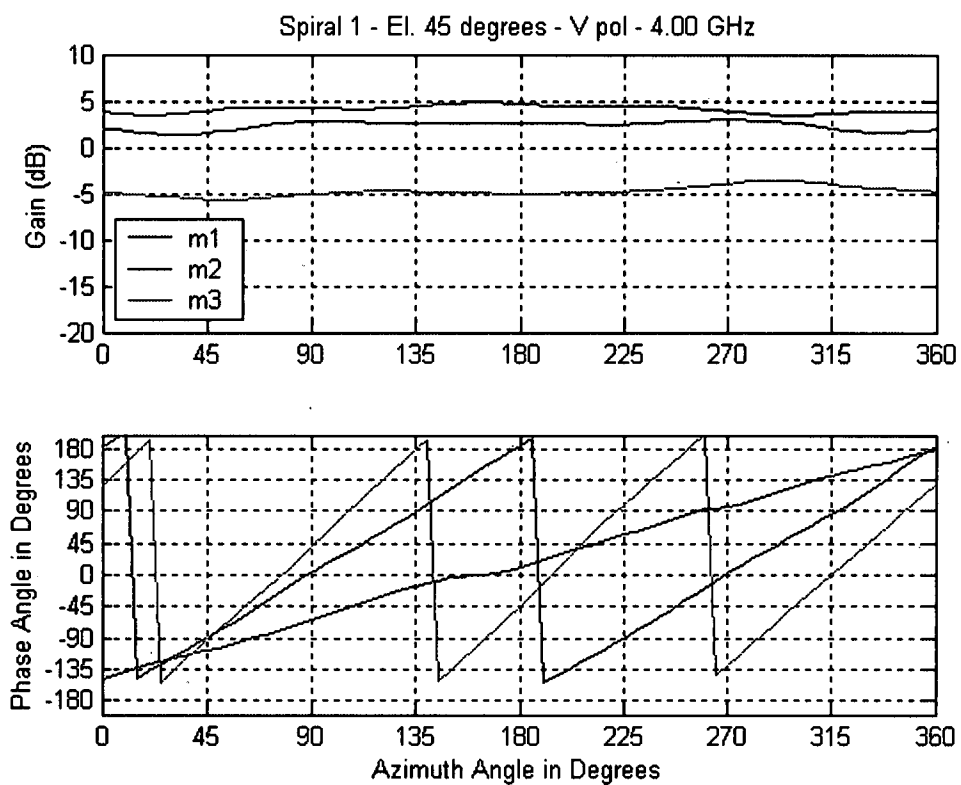


Figure 3.7: All modes for antenna 1 at an elevation angle of 45°.

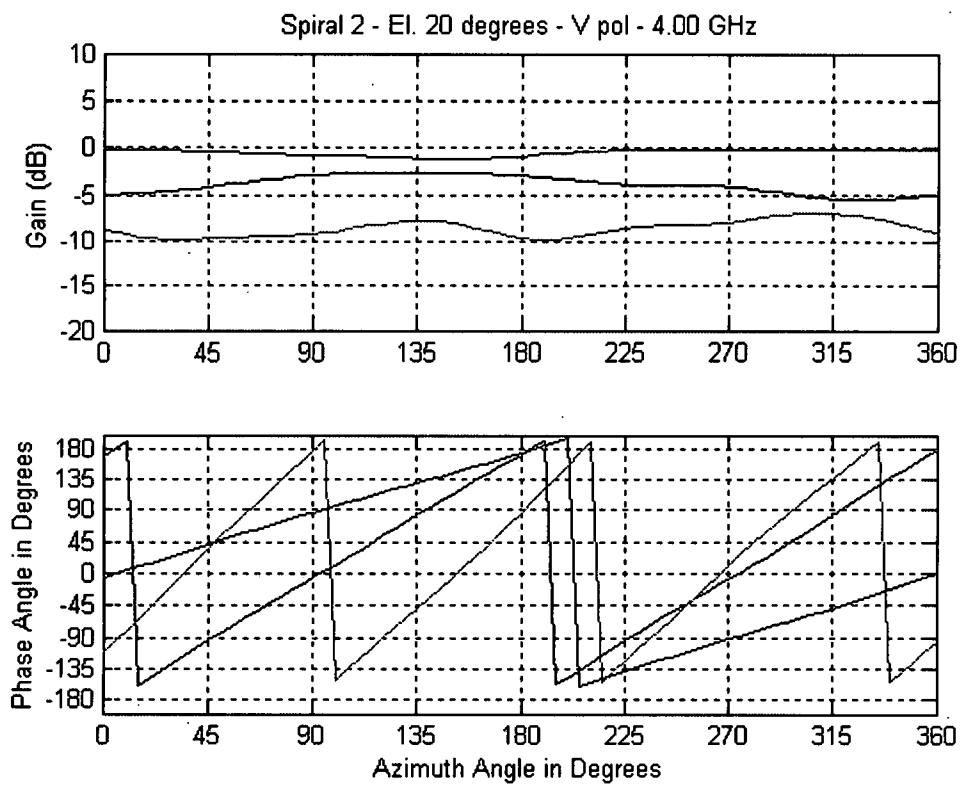


Figure 3.8: All modes for antenna 2 at an elevation angle of 20°.

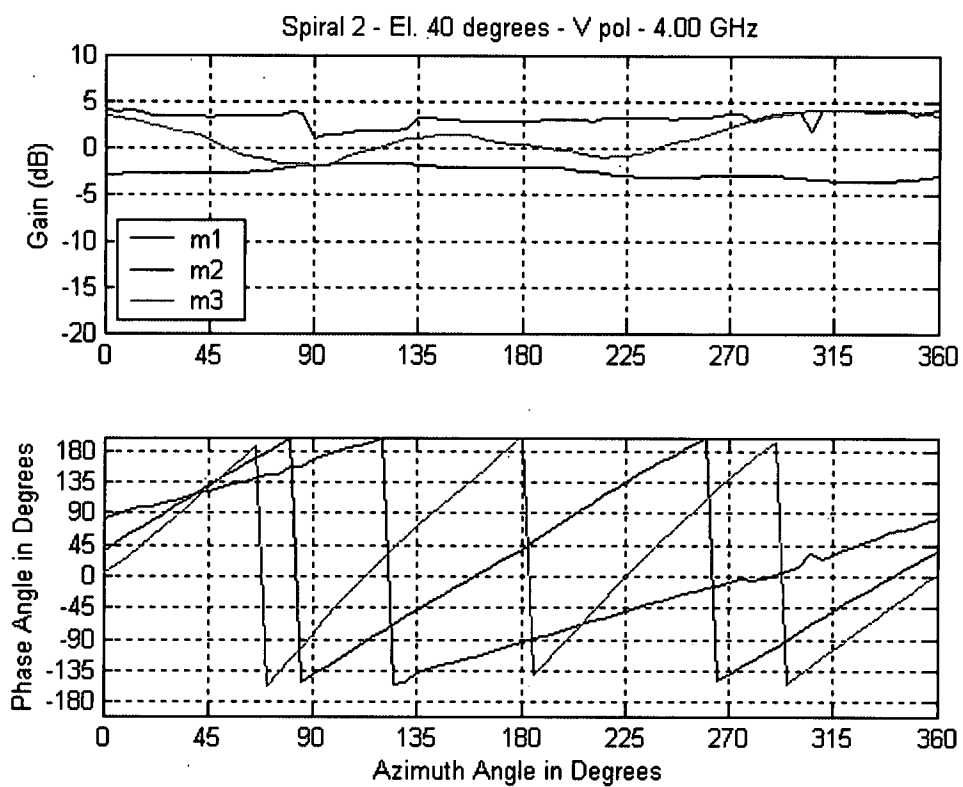


Figure 3.9: All modes for antenna 2 at an elevation angle of 40°.

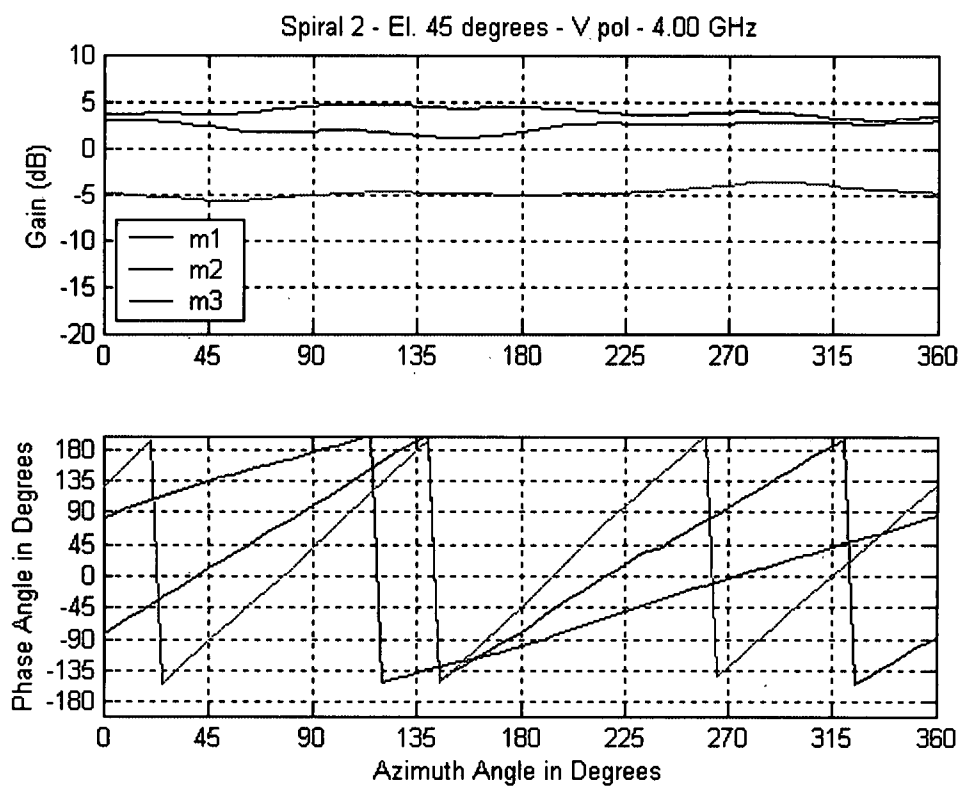


Figure 3.10: All modes for antenna 2 at an elevation angle of 45°.

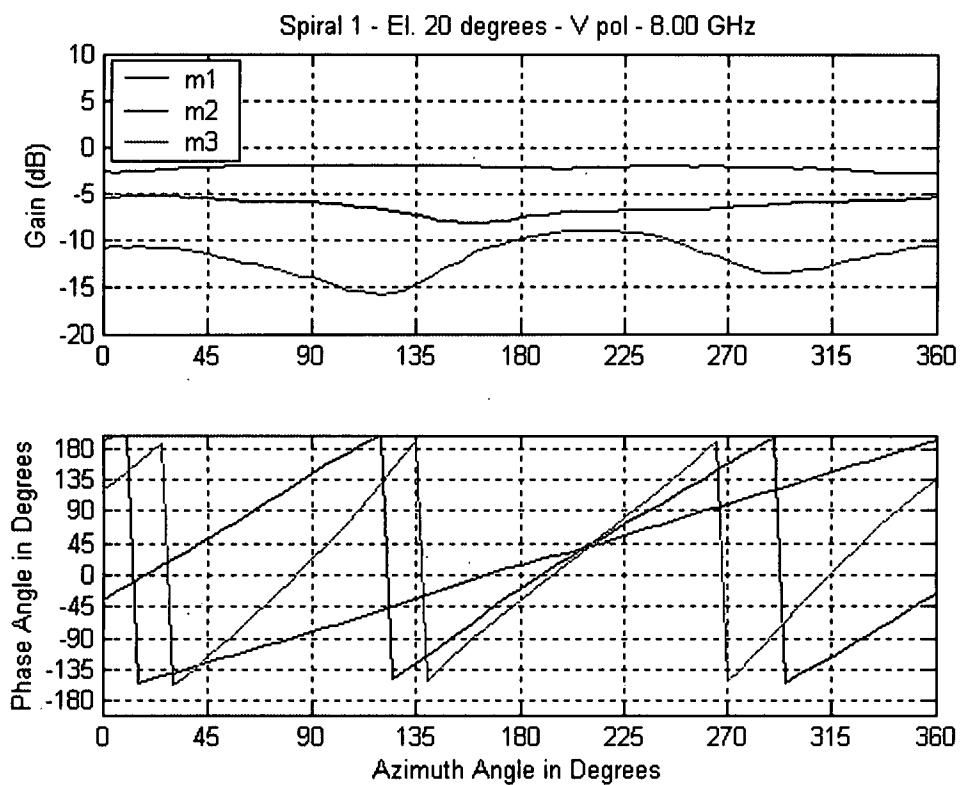


Figure 3.11: All modes for antenna 1 at an elevation angle of 20°.

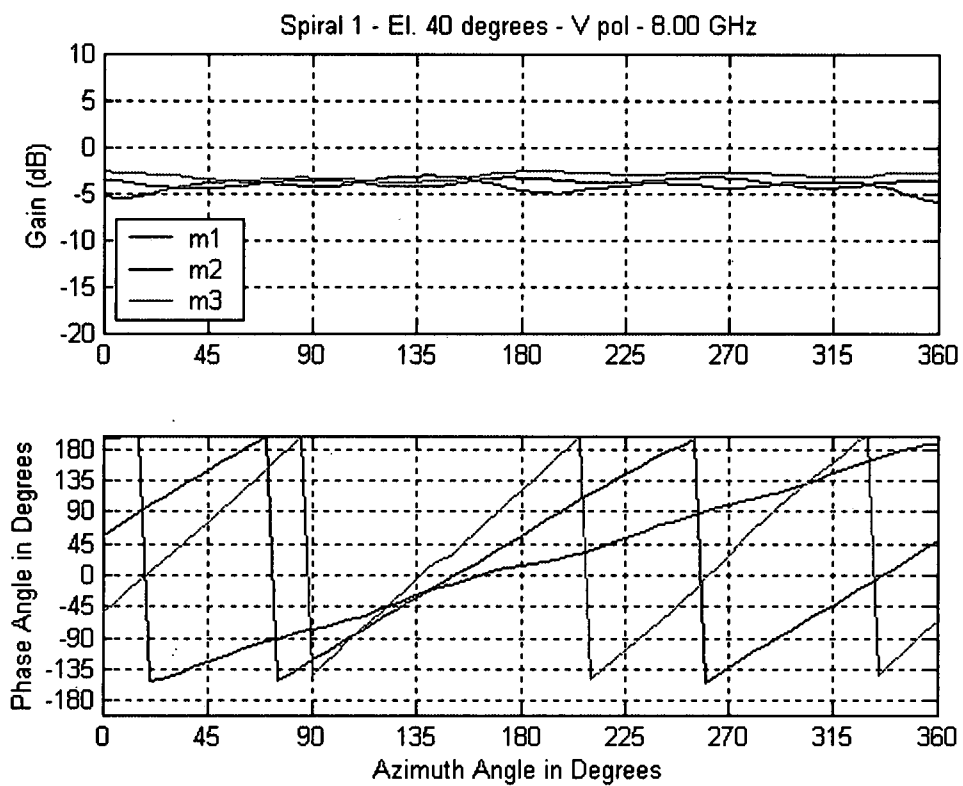


Figure 3.12: All modes for antenna 1 at an elevation angle of 40°.

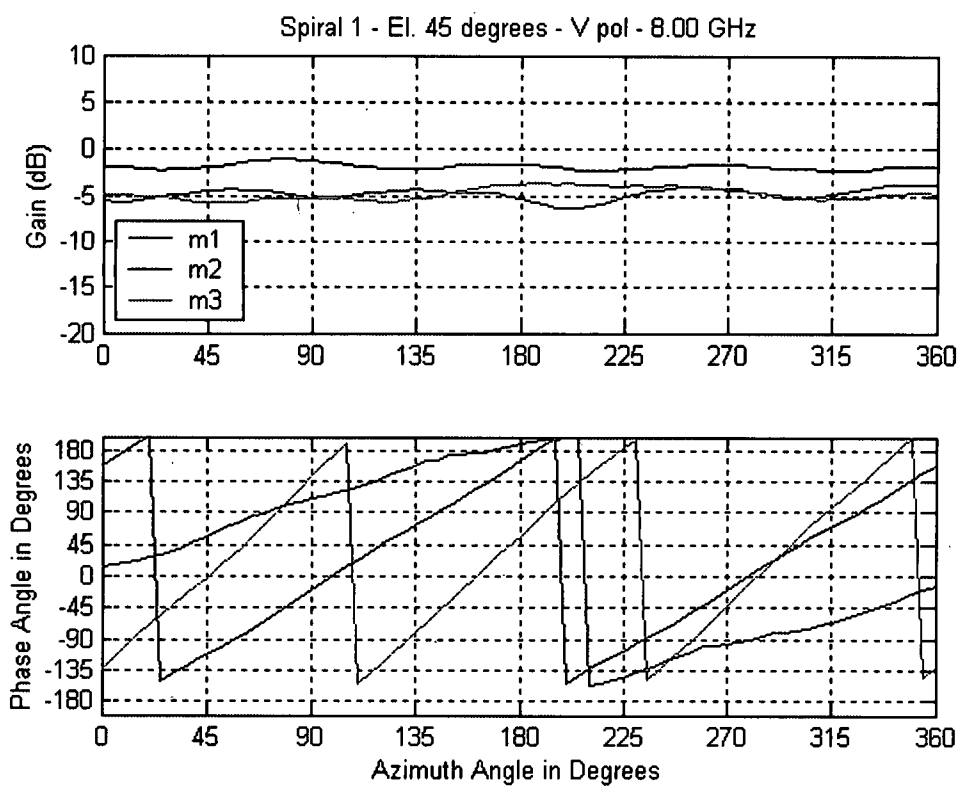


Figure 3.13: All modes for antenna 1 at an elevation angle of 45°.

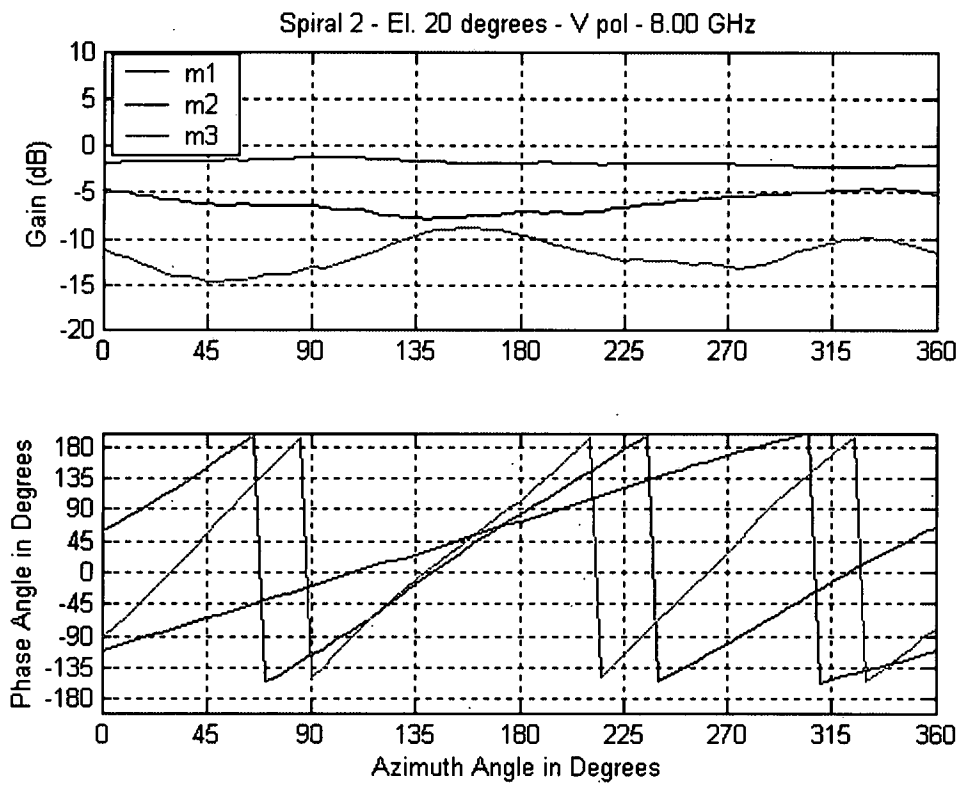


Figure 3.14: All modes for antenna 2 at an elevation angle of 20°.

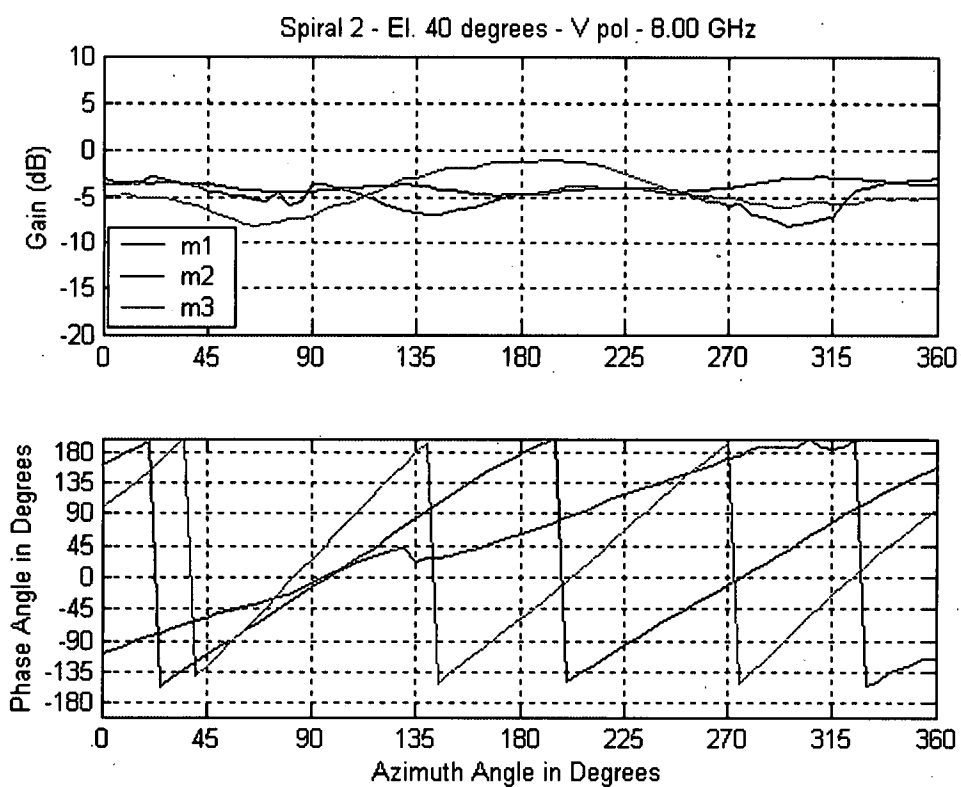


Figure 3.15: All modes for antenna 2 at an elevation angle of 40°.

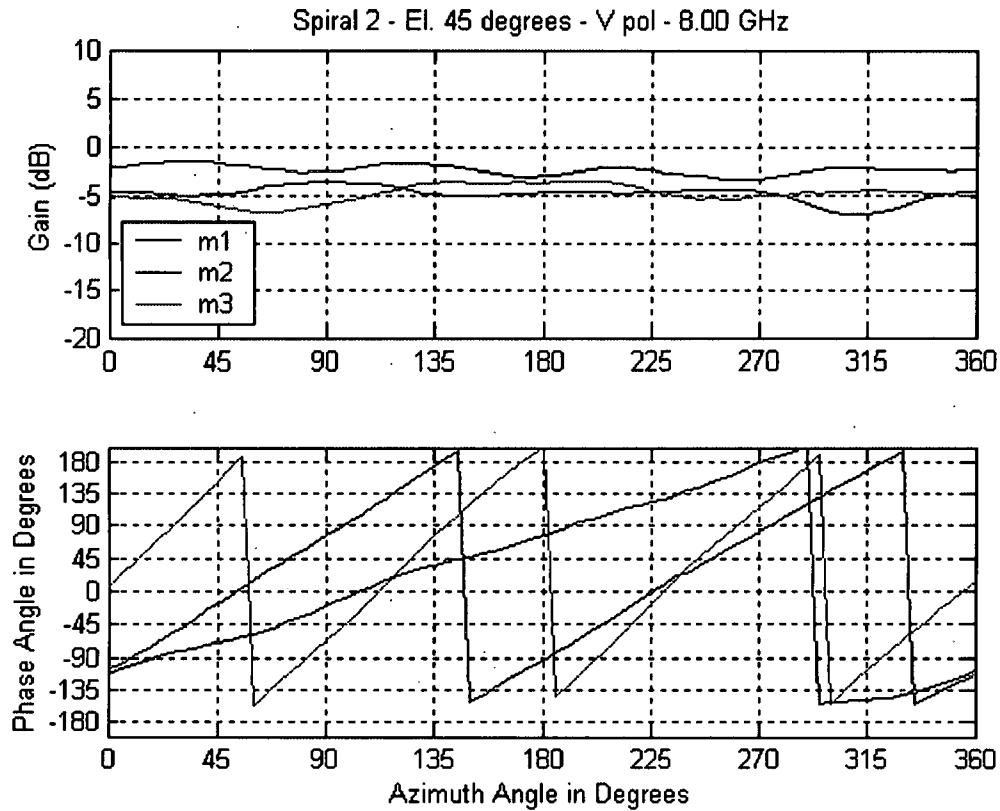


Figure 3.16: All modes for antenna 2 at an elevation angle of 45°.

From figures 3.5-3.16, one can clearly see the strong congruence between both 4-arm spiral antennas. Referring to figures 3.5 and 3.8 ($\theta=20^\circ$, 4GHz, Spiral 1 and 2 respectively), the discrepancy in the gain of mode 1 may be noted. It appears that this discrepancy may be attributed to a calibration error during the measurement. From an analysis of the data shown in figures 3.5-3.16, one can forge the following observations:

- The magnitudes of the modal outputs are relatively invariant with respect to azimuth, as predicted by theory discussed in chapter 2.
- The phase angles of the modal outputs change linearly with azimuth as predicted by theory. Indeed, this is the crucial result that makes possible the determination of azimuth from the modal output measurements. It may be noted, however, that the linearity is not perfect and leads to errors in azimuth angle estimation.

- The data clearly shows the differences in the outputs of the two “identical” four-arm spiral antennas, demonstrating the need and importance of calibration. The data clearly shows the differences in modal phase starting points for each mode at $\phi = 0^\circ$; this observation demonstrates the need and importance of calibration. The incident field at the phase reference (especially the phase) is different for each measurement and must be properly accounted for to obtain reliable AoA measurements.

Figures 3.17-3.25 show the data for the three modal outputs at 12GHz and exemplify the experimental data in the upper portion of the 8-12GHz band. Note the phase difference between the two antennas in figures 3.17-3.19. As mentioned before, this demonstrates the need for calibration.

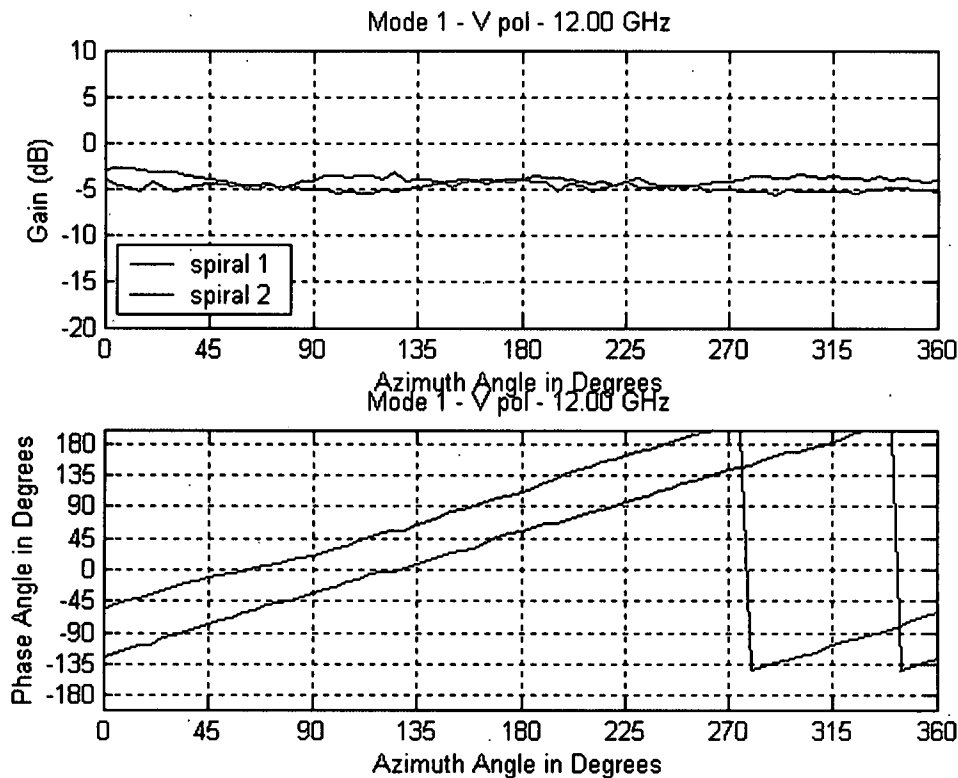


Figure 3.17: Both spiral antennas for mode 1 at an elevation angle of 20° .

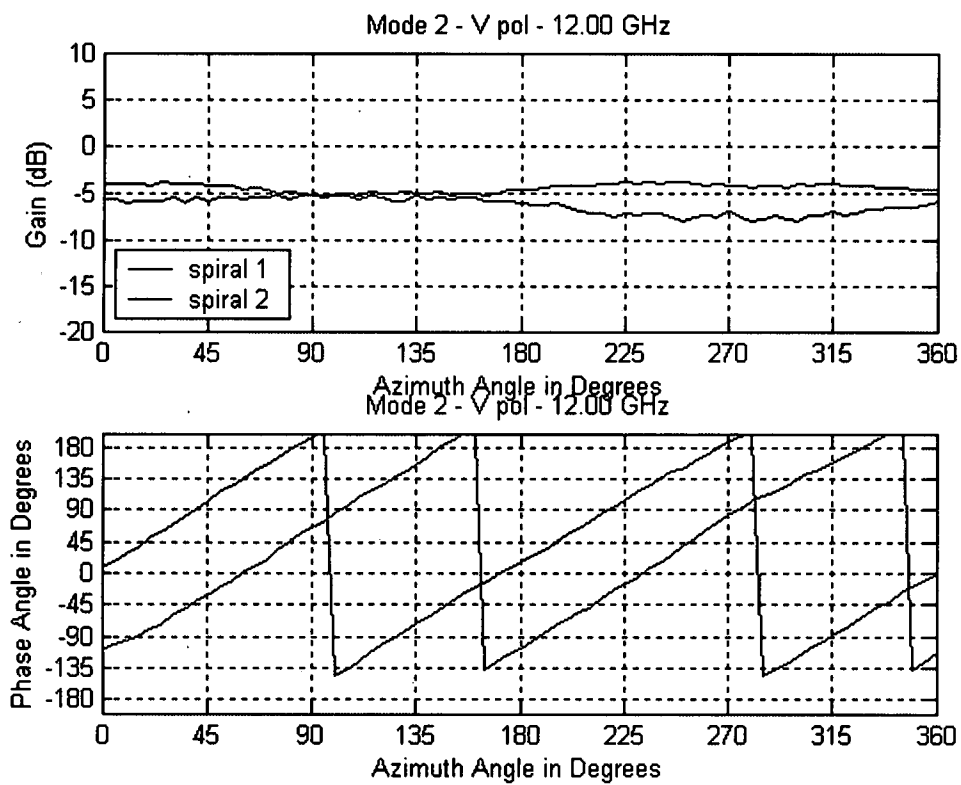


Figure 3.18: Both spiral antennas for mode 2 at an elevation angle of 40°.

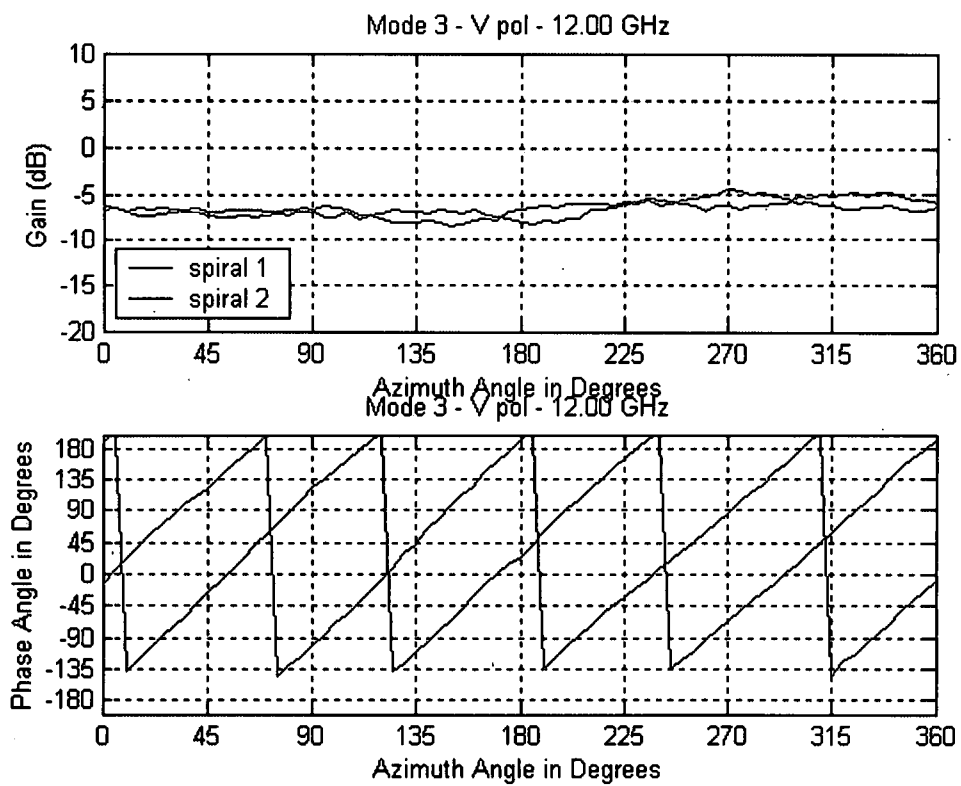


Figure 3.19: Both spiral antennas for mode 3 at an elevation angle of 45°.

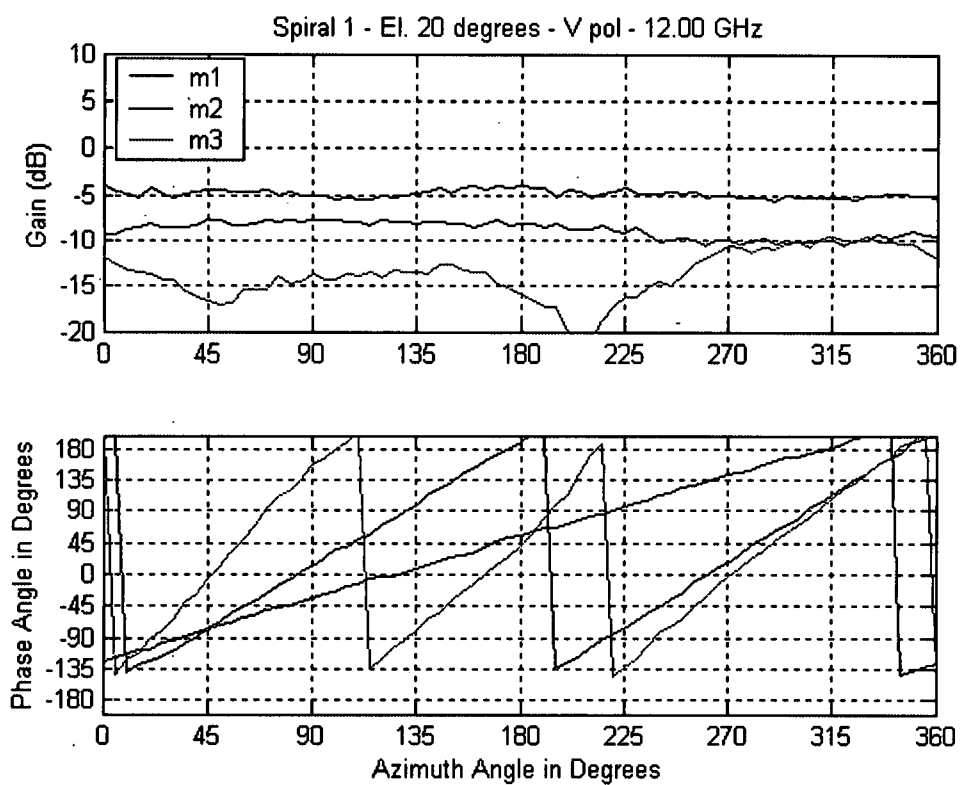


Figure 3.20: All modes for antenna 1 at an elevation angle of 20°.

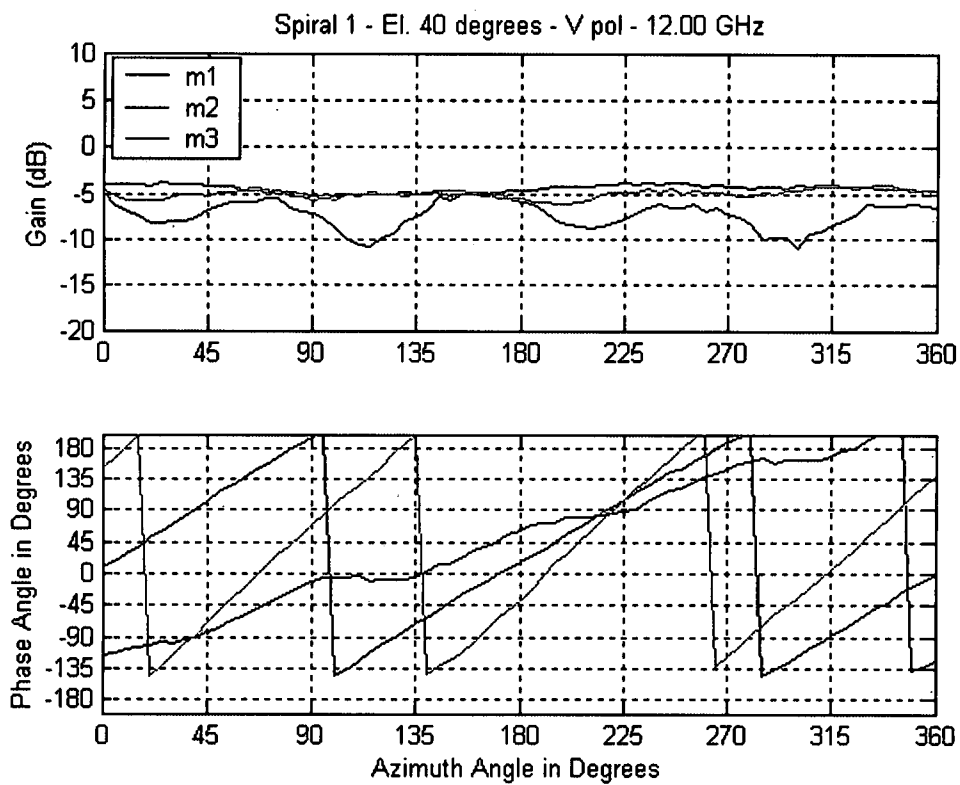


Figure 3.21: All modes for antenna 1 at an elevation angle of 40°.

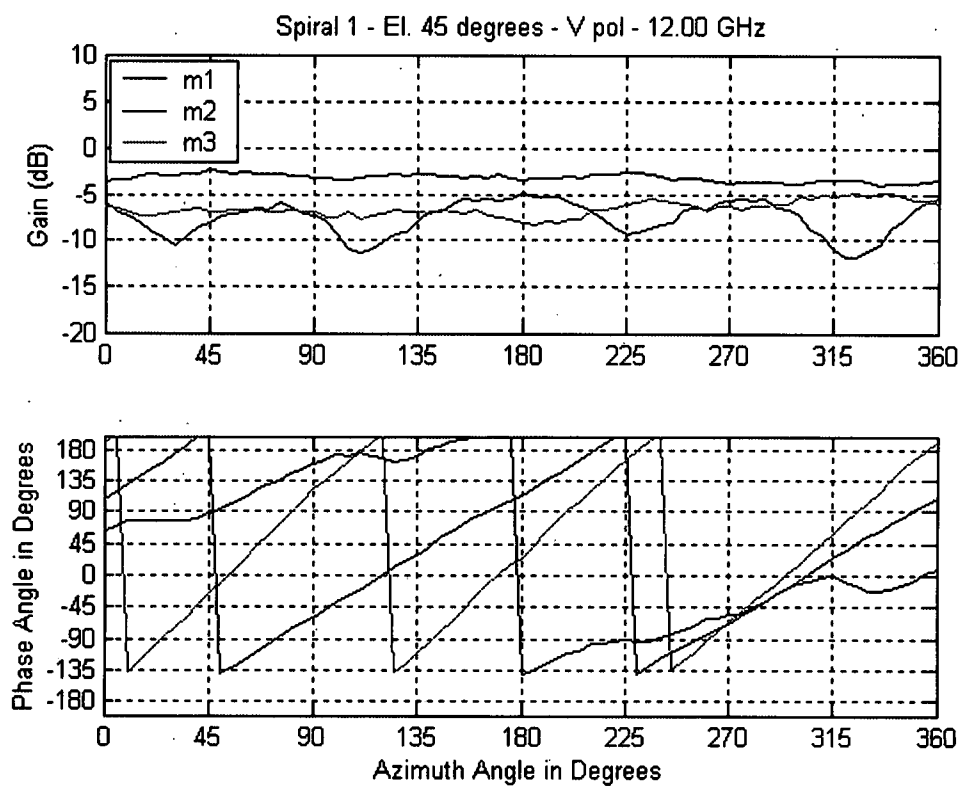


Figure 3.22: All modes for antenna 1 at an elevation angle of 45°.

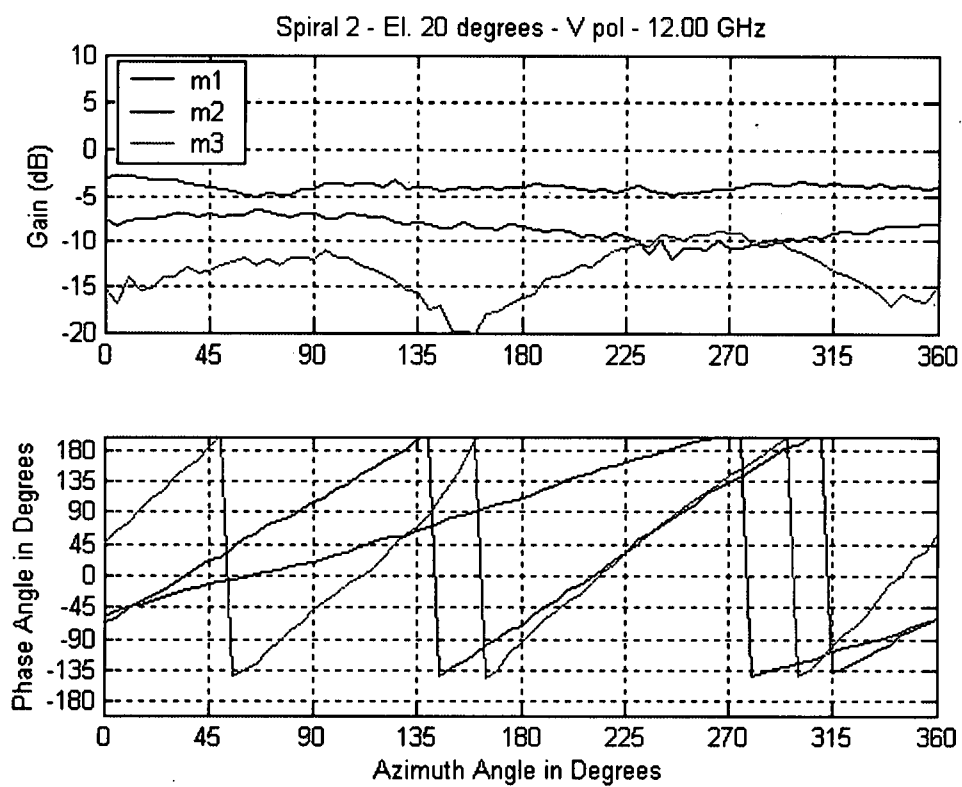


Figure 3.23: All modes for antenna 2 at an elevation angle of 20°.

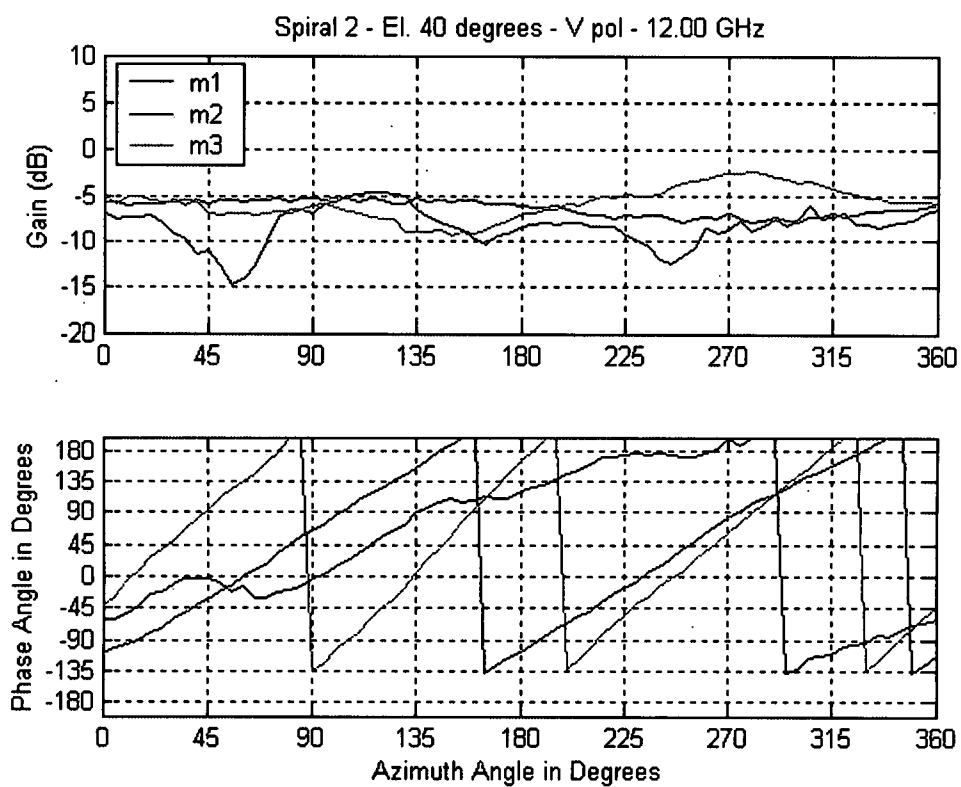


Figure 3.24: All modes for antenna 2 at an elevation angle of 40°.

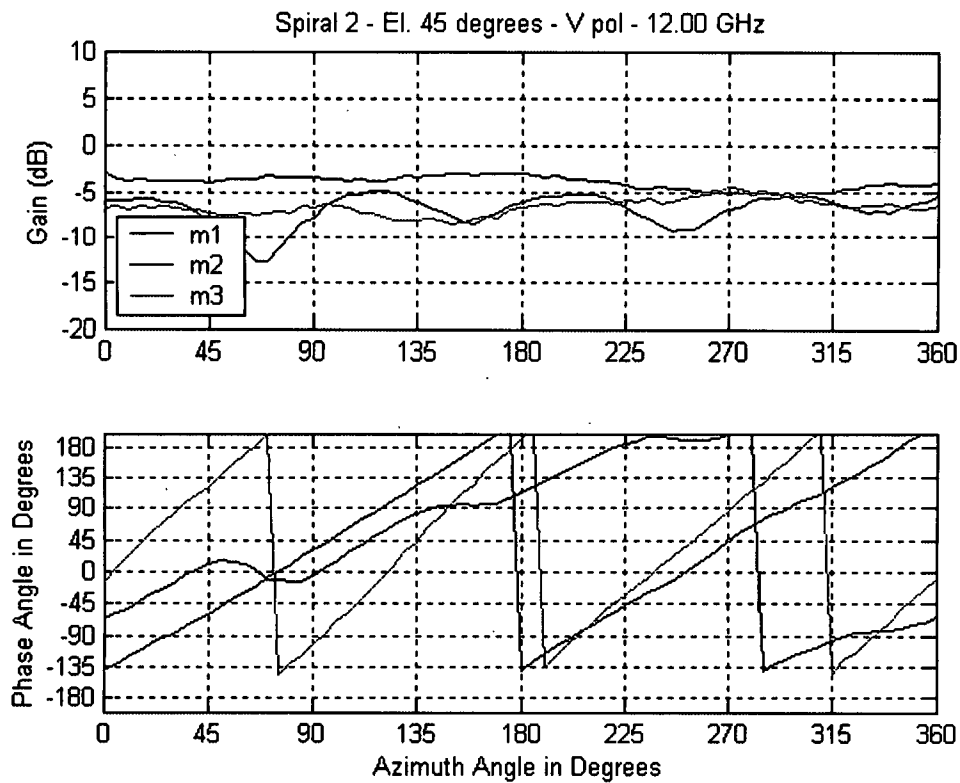


Figure 3.25: All modes for antenna 2 at an elevation angle of 45°.

The observations made earlier for the 4-8 GHz band continue to be valid except for a more pronounced appearance of ripple. It is reasonable to expect this increased "ripple" in phase to manifest as increased variance in the azimuth angle estimates at the higher end of the band. This "ripple" is observed in particular at the high end of the band and may be due to the active region approaching the feed region, as discussed in chapter 2. Any small asymmetries or imperfections in the feed are likely to affect the active region, especially for mode 1, at higher frequencies. Also notice that the "ripple" in the mode 1 phase tends to increase in the upper band when the elevation AoA is outside of the mode 1 main pattern coverage area, which is observable in figures 3.21-3.22 and figures 3.24-3.25. It is reasonable to expect this increased "ripple" to manifest as increased variance in the azimuth angle estimates at the higher end of the band.

3.2.2 Elevation Measurements

The range setup for elevation data collection is shown in figure 3.26. The phase-stationary test body begins positioned at $\theta = 90^\circ$ elevation. The test body then rotates via the septum (see figure 3.3b) a full 90° and terminates when the spiral is boresight to the parabolic reflector. The spiral is then itself rotated 180° , via the can (see figure 3.3b), and the elevation position reset to $\theta = 90^\circ$. The original scan sequence is then repeated: The test body rotates via the septum another full 90° and terminates when the spiral is boresight to the parabolic reflector. This process was carried out for modes 1, 2, and 3 for both 4-arm spiral antennas from 4-12 GHz; the magnitude data obtained was joined for each respective mode and full 180° elevation slices were obtained for an azimuth angle of $\phi = 0^\circ$. The data was taken in at 5° elevation increments.

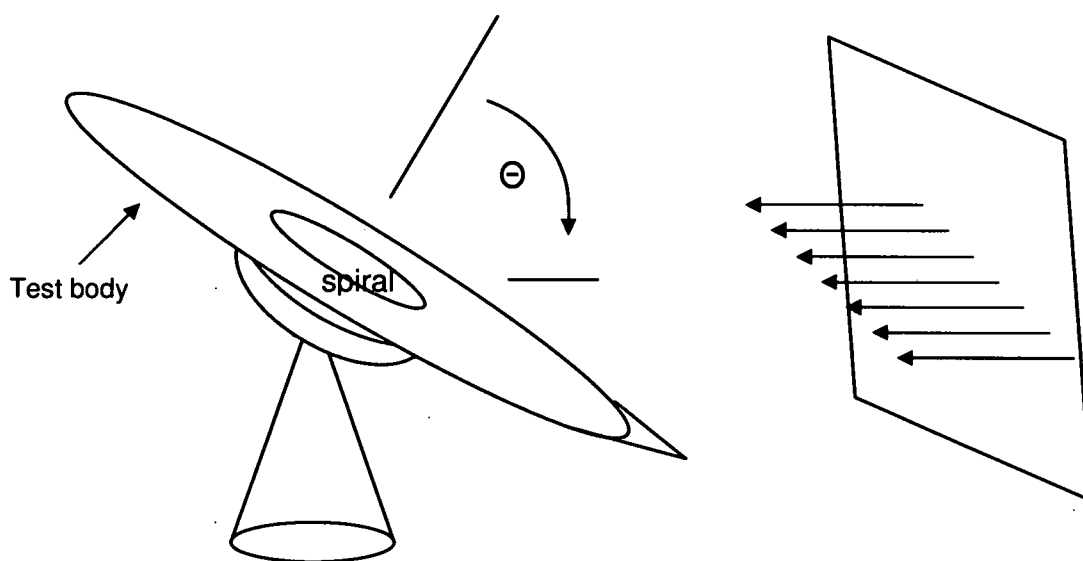


Figure 3.26: Spiral elevation measurement setup in RASCAL.

Figures 3.27-3.35 show the acquired magnitude data from each mode of the aforementioned elevation cuts. All data shown is for vertical polarization of both four-arm spirals. It should also be noted that the x-axis scale ranges from 0° to 180° rather than -90° to 90° in figures 3.21-3.42 and in elevation plots in chapter 4; boresight in these plots will be defined as the elevation angle of 90° . Elevation angles in this text

described as 20° , 40° , or 45° , should be inferred to mean 90° plus 20° , 40° , or 45° in figures 3.21- 3.42 and elevation plots in chapter 4.

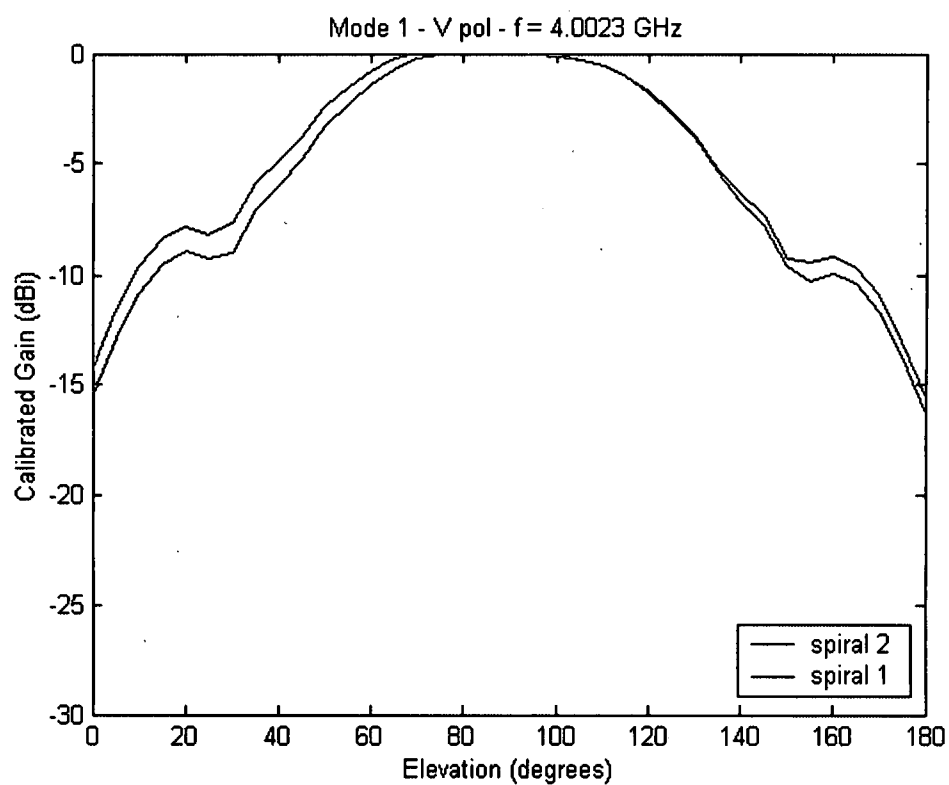


Figure 3.27: Elevation cut at mode 1 for both spiral antennas.

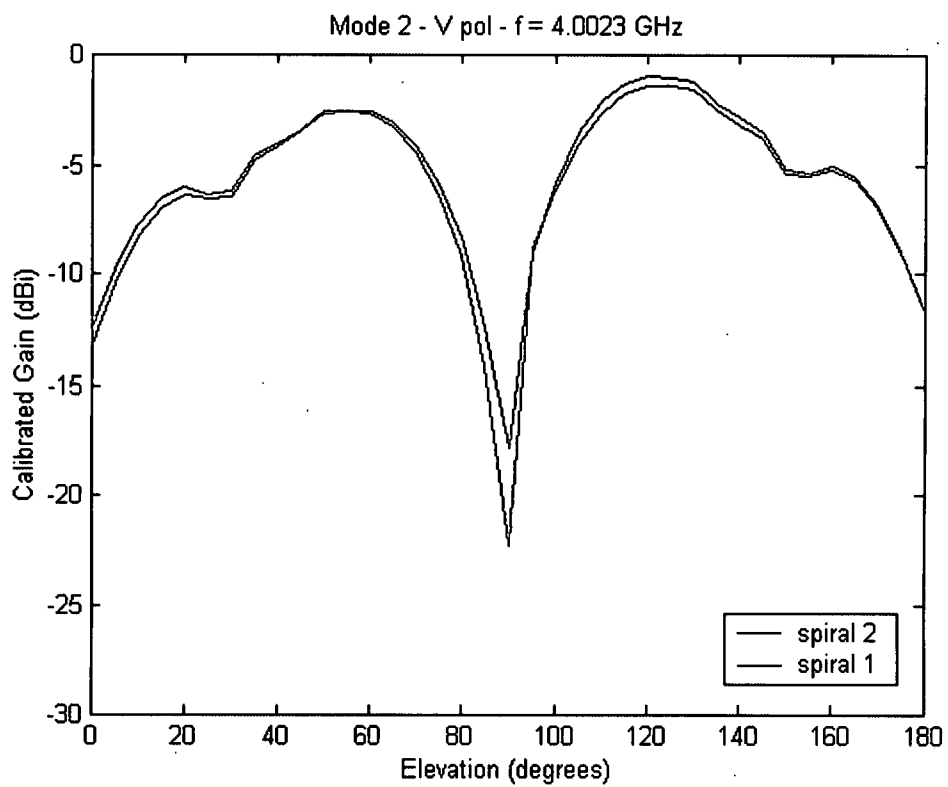


Figure 3.28: Elevation cut at mode 2 for both spiral antennas.

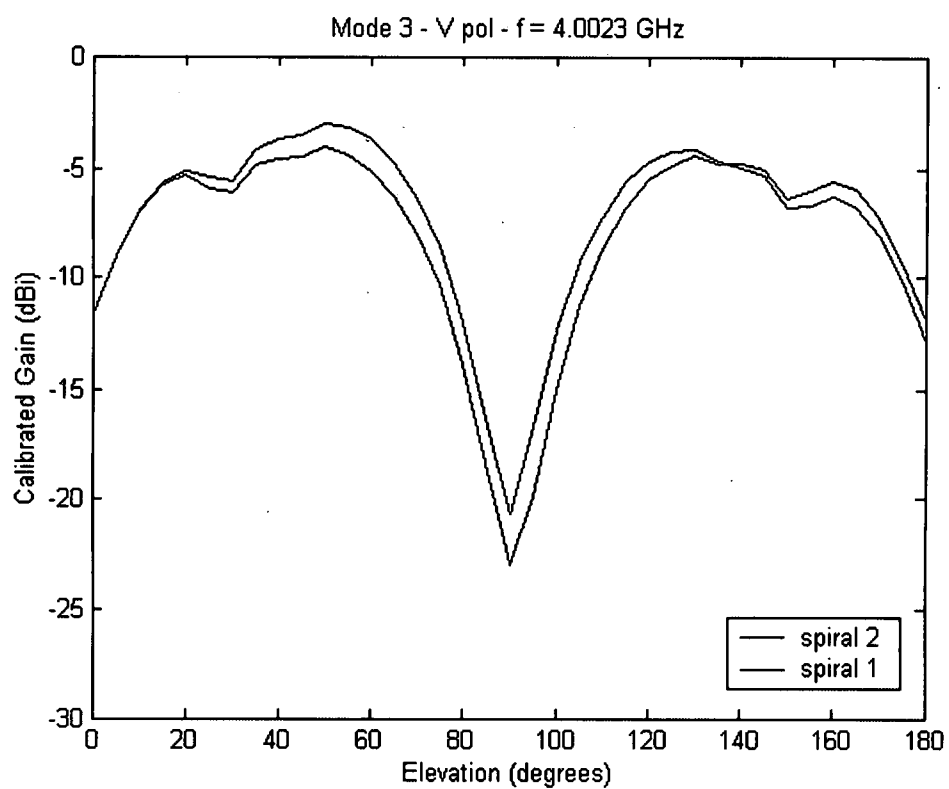


Figure 3.29: Elevation cut at mode 3 for both spiral antennas.

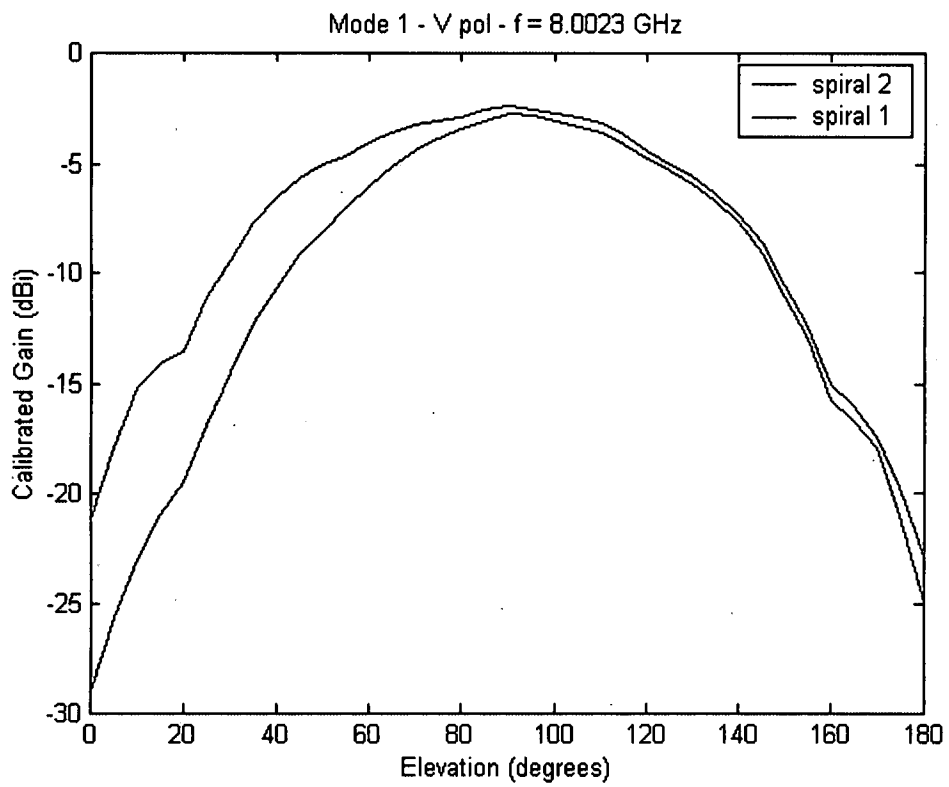


Figure 3.30: Elevation cut at mode 1 for both spiral antennas.

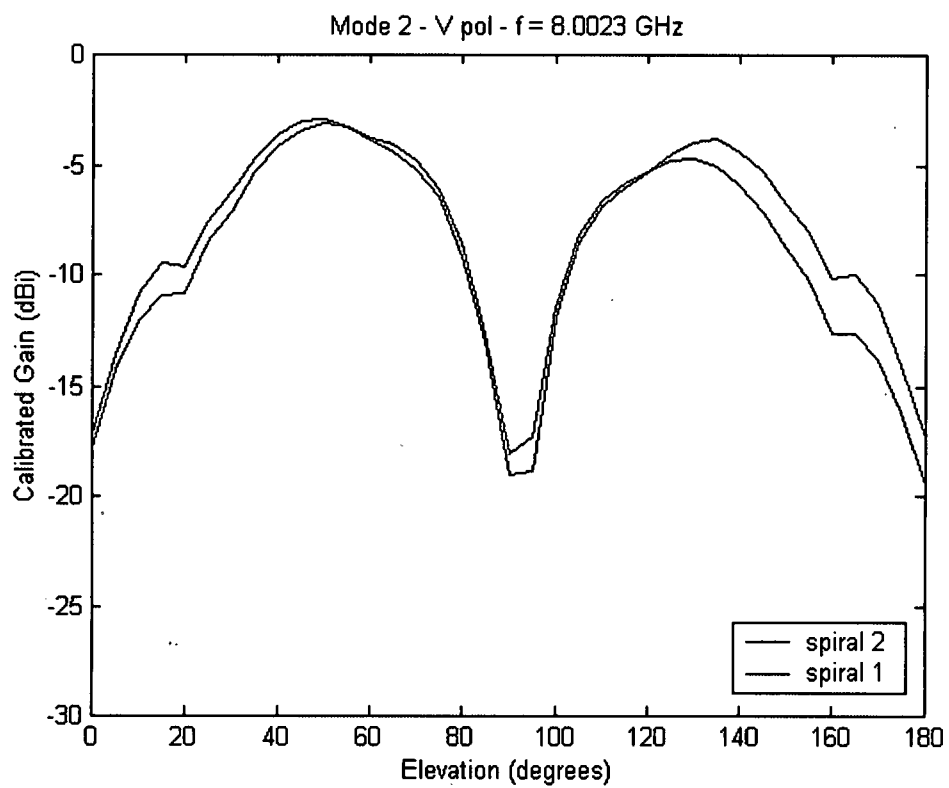


Figure 3.31: Elevation cut at mode 2 for both spiral antennas.

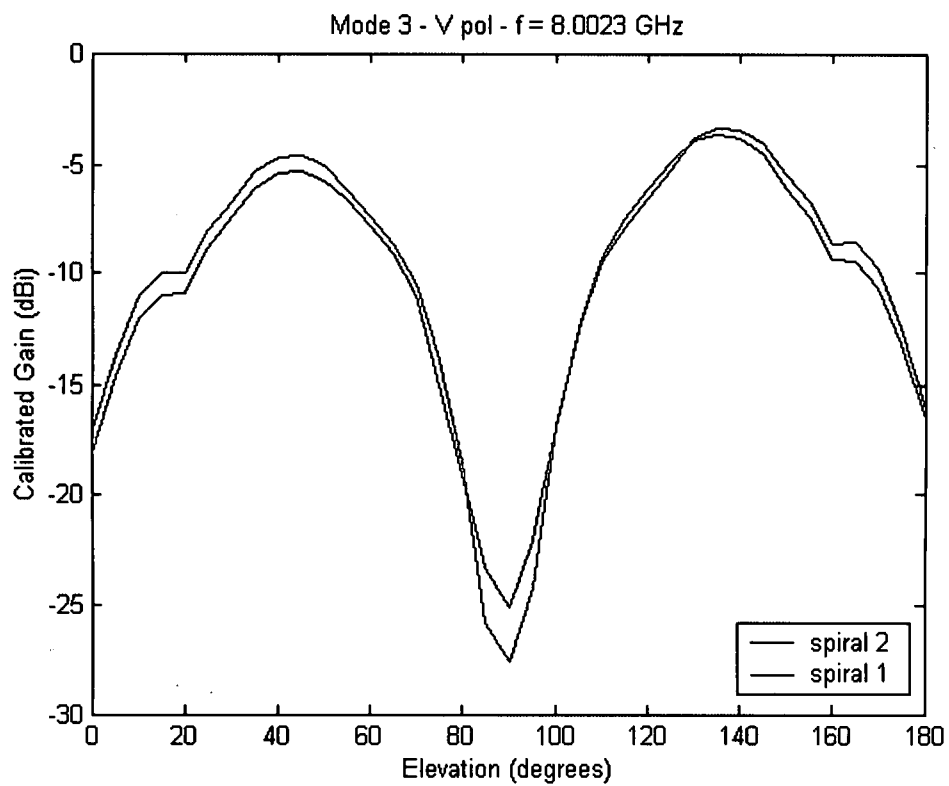


Figure 3.32: Elevation cut at mode 3 for both spiral antennas.

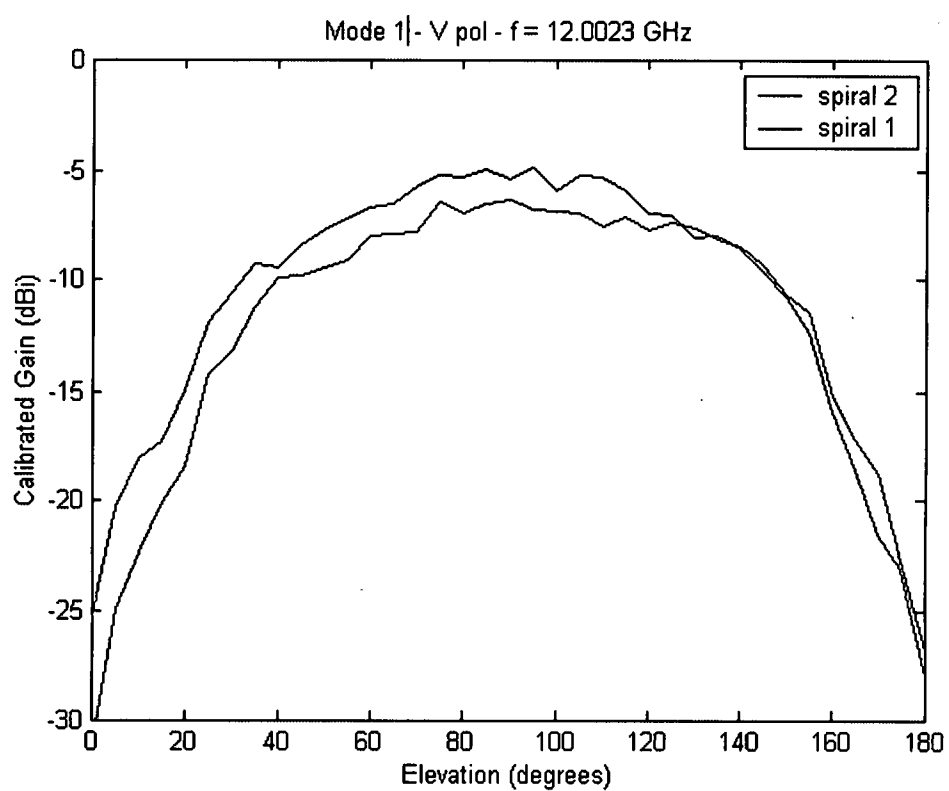


Figure 3.33: Elevation cut at mode 1 for both spiral antennas.

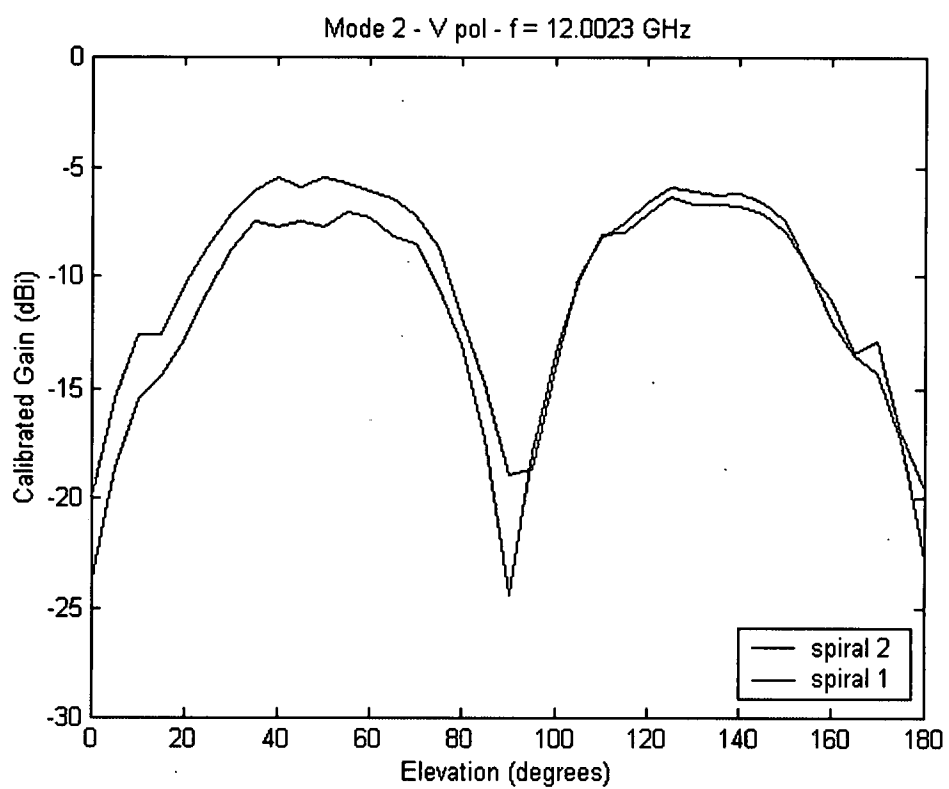


Figure 3.34: Elevation cut at mode 2 for both spiral antennas.

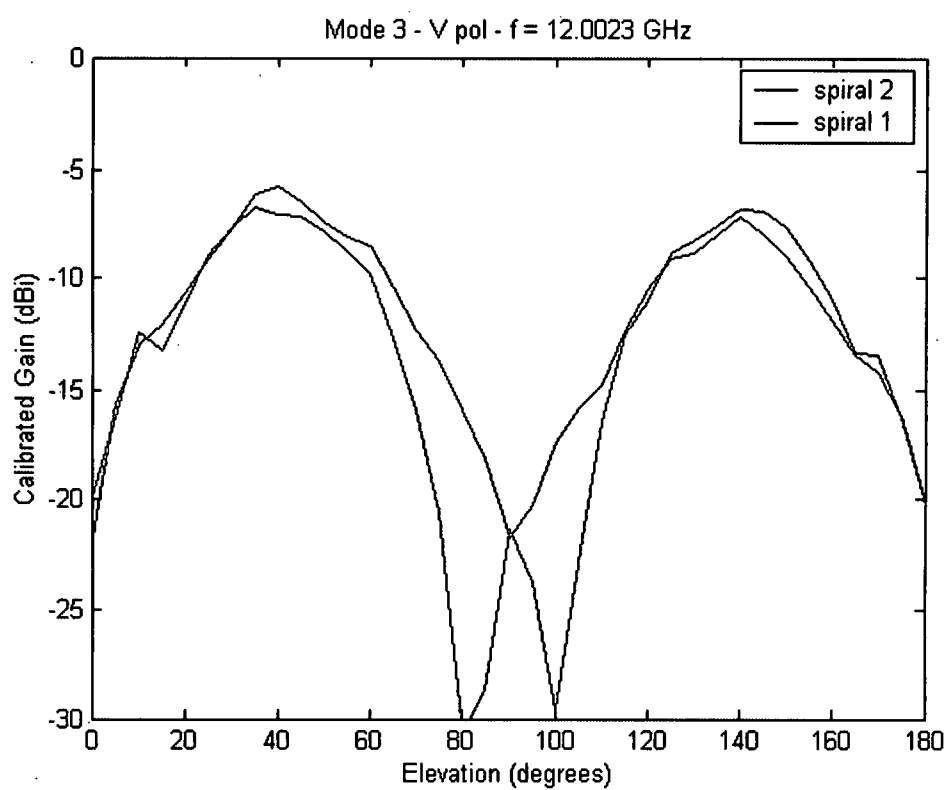


Figure 3.35: Elevation cut at mode 3 for both spiral antennas.

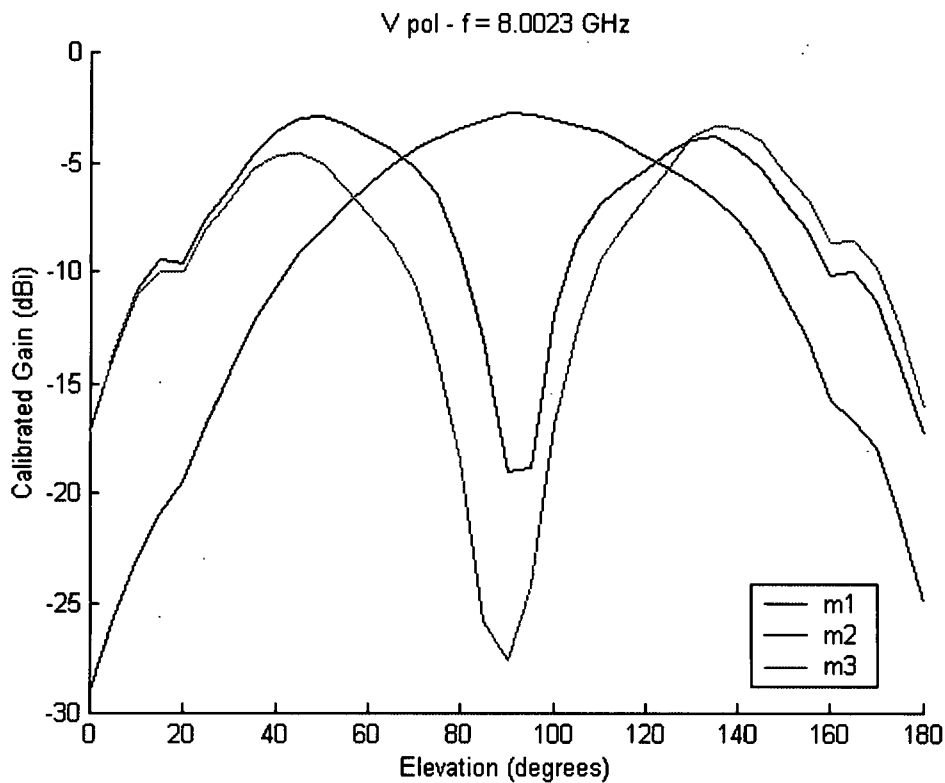


Figure 3.36: Elevation cut patterns for antenna 1, all modes.

Though the data is not exactly identical, figures 3.27-3.35 clearly show the strong congruence between both 4-arm spiral elevation patterns. Figure 3.36 shows the tri-modal elevation patterns for antenna 1 at 8GHz, for a better glimpse at the geometry of the three radiated patterns (as noted in figure 2.5 of chapter 2). From an analysis of the data shown in these figures, one can forge the following observations:

- The shapes of the modal elevation patterns are aptly congruent with theory, as discussed in chapter 2.
- The elevation pattern for mode 1 boasts the peak gain level at boresight with a wide coverage area again as precisely predicted by theory.
- The elevation pattern for mode 2 boasts a null in pattern at boresight with a wide coverage area approaching endfire again as precisely predicted by theory.

- The elevation pattern for mode 3 boasts a null in pattern at boresight with a wide coverage area approaching closer to endfire than mode 2 again as precisely predicted by theory.
- As frequency increases, mode patterns for modes 2 and 3 respectively approach closer to endfire as predicted by theory.
- As the elevation patterns approach the horizon on each side ($\theta = 0^\circ - 20^\circ$ on the above elevation plot scales, $\theta = 70^\circ - 90^\circ$ in typical elevation scales), small ripple idiosyncrasies are noticeable (most noticeable in modes 2 and 3). This is due in part to the test body ground plane not being "infinite." These ripples will therefore affect the elevation modal ratios near the horizon, which will affect the accuracy of elevation AoA estimates near the horizon to be sure.
- As frequency increases, the appearance of ripple in the elevation patterns is noticeable. This ripple is sure to affect the elevation modal ratios, which is sure to affect the elevation angle estimates at the high end of the frequency band.
- Due to element by element variations, antenna tolerances, and range inconsistencies clearly visible in the elevation pattern data demonstrated above, it is quite evident that the need for data calibration exists.

In order to accumulate the elevation measurement data into a form which is useful to obtain elevation AoA estimates, it is desirable to calculate the ratio of elevation magnitudes between mode 3 and mode 1, and mode 2 and mode 1. The ratios are computed and then plotted, as shown in figures 3.37-3.42.

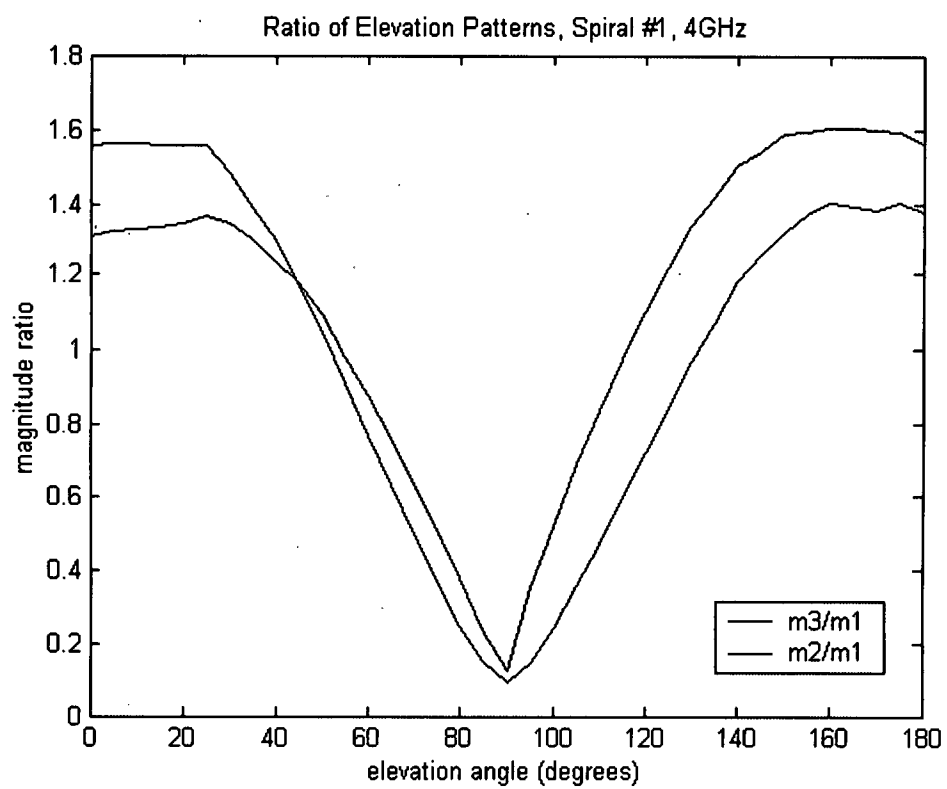


Figure 3.37: Ratio of Elevation Patterns for Spiral one at 4GHz.

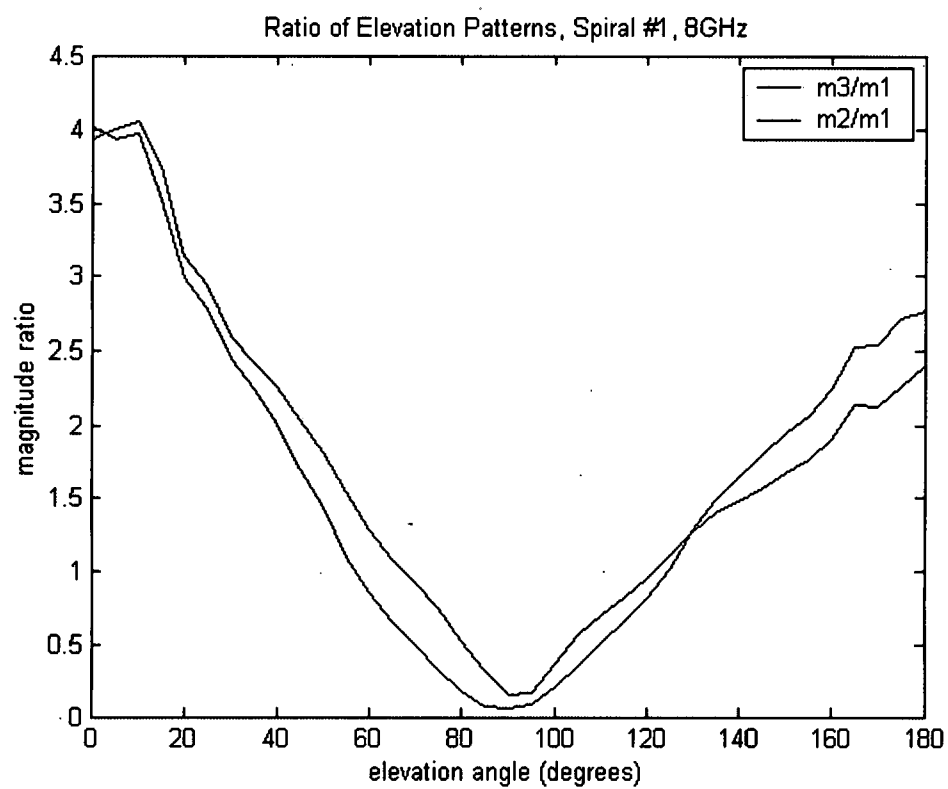


Figure 3.38: Ratio of Elevation Patterns for Spiral one at 8GHz.

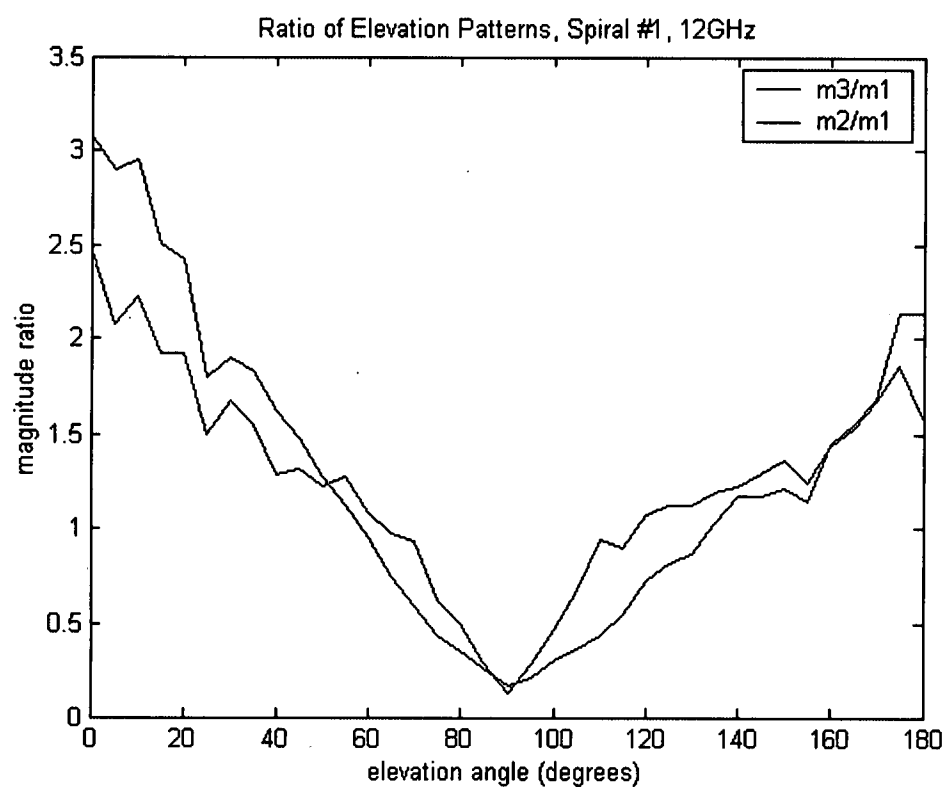


Figure 3.39: Ratio of Elevation Patterns for Spiral one at 12GHz.

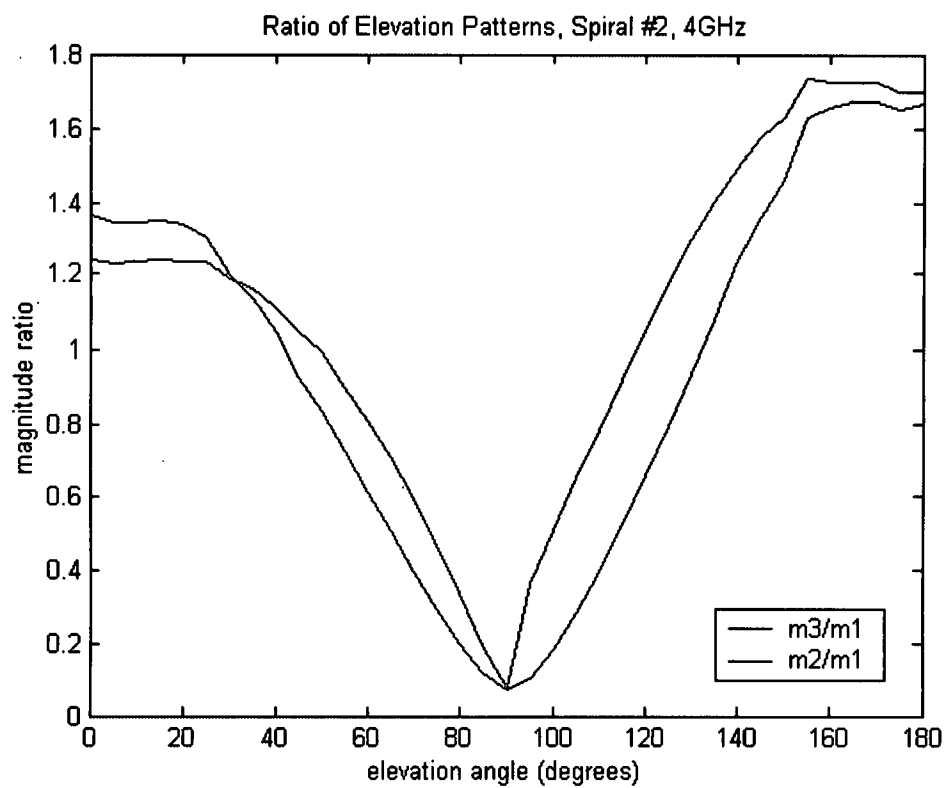


Figure 3.40: Ratio of Elevation Patterns for Spiral two at 4GHz.

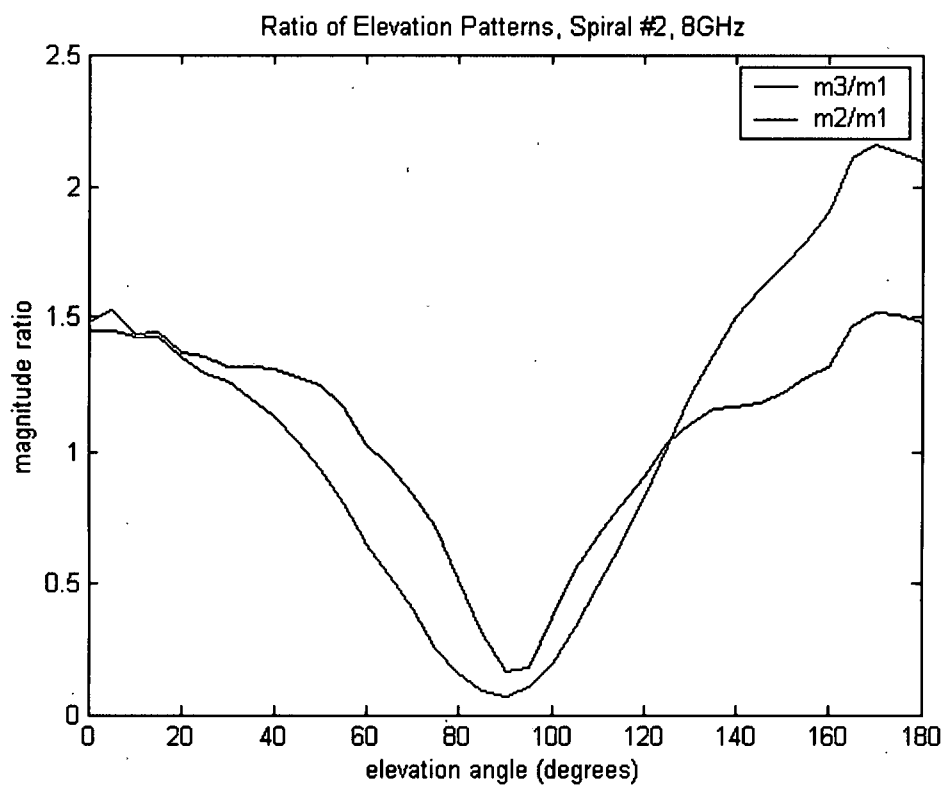


Figure 3.41: Ratio of Elevation Patterns for Spiral two at 8GHz.

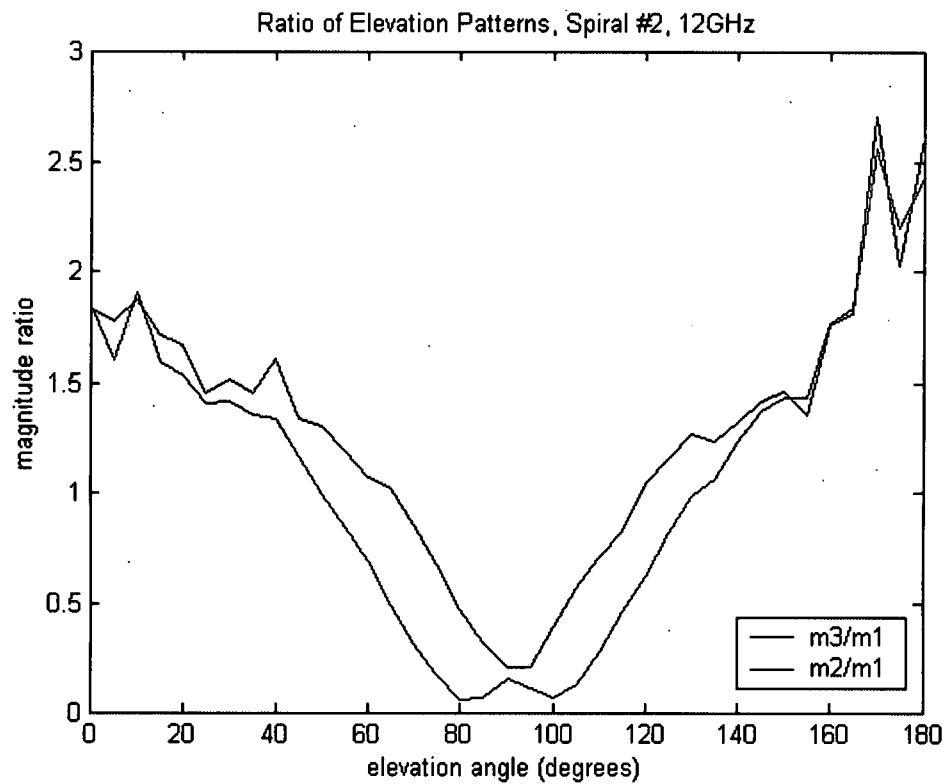


Figure 3.42: Ratio of Elevation Patterns for Spiral two at 12GHz.

It is evident that increased “ripple” in the elevation ratios exist as frequency increases. This is not a complete surprise, as we have observed this “ripple” in the upper frequency band of the elevation measurements of figures 3.27-35. It is this elevation pattern ratio data that we will use to compute elevation angle estimates in the next chapter. The increased ripple visible near the horizon of the ratios will undoubtedly lead to inconsistencies in elevation angle estimates near the horizon.

CHAPTER IV

RESULTS

This chapter describes the process of estimating the AoA from the measurements detailed in chapter 3 and also analyzes the dependence of the AoA estimates on SNR, frequency, and angular coverage. The measured data must be calibrated before AoA estimates may be obtained from this data. The need for this calibration and its implementation are discussed in this chapter. A Monte Carlo analysis is carried out to determine the statistics of AoA estimates. The measured data is considered pristine and noise is artificially injected into the measured data in order to obtain any given signal-to-noise ratio. The results of these Monte Carlo experiments are discussed here.

4.1 Calibration

The calibration of the collected phase data, or phase compensation as mentioned in chapter 2, is a necessity as part of the process of determining azimuth AoA for a four-arm spiral antenna. As mentioned in chapter 2, the phase comparison of the modeformer output of a spiral is how azimuth is estimated. The differences in the phase offset at $\phi_o = 0$ present in figures 3.5-3.25 demonstrate the need for calibration. Only by knowing the actual position of each linear modal phase progression can one obtain an accurate estimate of azimuth.

The azimuth angle is deduced from the measured data by comparing the phases of the received modal output signals. Recalling from chapter 2 equation 2.13, the modal output signal is given by:

$$M_{\theta}^n = E_o e^{j\psi_n} \left(\frac{n\lambda}{2\pi} \right) \pi j^n e^{-jn\phi_o} \times [\cos \theta_o (J_{n-1}(n \sin \theta_o) + J_{n+1}(n \sin \theta_o))] \quad (4.1)$$

Above, ψ_n depends upon the geometry of the spiral and also the mode number as mentioned in chapter 2. Assuming, for the moment, that the incident field (magnitude and phase) E_o is known, the phase of $j^n e^{-j\psi_n} M_{\theta}^n$ in equation 4.1 is simply:

$$\text{angle}(j^{-n} e^{-j\psi_n} M_{\theta}^n) = -n\phi_o \quad (4.2)$$

As clearly shown in figure 4.1, ϕ_o the azimuth angle, can be readily estimated from the measured phase values. In effect, the phase of all the modal outputs at $\phi_o = 0$ is zero. This "phase compensation" is obtained in practice by determining the phase of the measured data for $\phi_o = 0$ and using this information to calibrate the measured data such that phases at $\phi_o = 0$ is zero for all modal outputs. It may be noted that the reference phase of the current in the active region is different for different modes and necessitates calibration of measured data to estimate the azimuth angle.

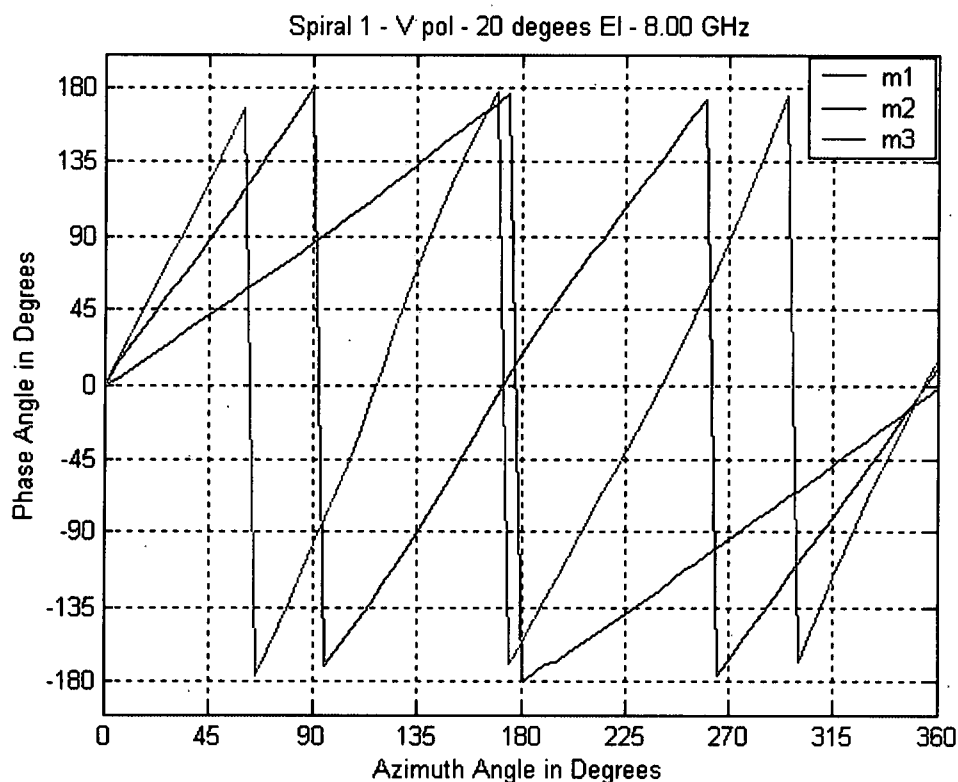


Figure 4.1: Calibrated phase data for $\theta = 20^\circ$ at 8GHz.

Note that, in practice, the incident field, E_o , is unknown and will cost one degree of freedom; angles are estimated from ratios of modal outputs, thus eliminating E_o . Since the measurements reported here did not measure the modal outputs simultaneously, the incident field is different for different modes; for azimuth angle estimations, the phase of E_o is calibrated out for each of the modal outputs. This made possible three separate estimates corresponding to three different modes.

After calibration, one can clearly observe the new common reference point (starting point) for the phase at $\phi = 0^\circ$ and more clearly observe the unique slopes respective to each mode that increase as the mode number increases.

As aforementioned in chapter 2, it is these unique linear phase progressions that allow azimuth angle estimation using the "comparison" approach described in the introduction. An incoming signal is received by the spiral antenna at a specific elevation angle and a specific azimuth angle. The accuracy of an angle estimate is dependent on the amount of spatial coverage the antenna exhibits; this is demonstrated by the antenna

pattern of the spiral. As observed in the azimuth measurements of chapter 3, the four-arm spiral antenna magnitude stays relatively constant over 360° azimuth coverage but elevation pattern coverage, as noted in figure 3.36, varies by mode. Where the gain is low, corresponding angle estimates are not as accurate. For example, an incoming signal at an elevation angle near the horizon will not receive very good spatial coverage from any mode, while an incoming signal at an elevation angle near boresight will receive spatial coverage from mode 1 only. Thus, the elevation angle of an incoming signal will determine which mode may provide the most accurate azimuth estimate.

Azimuth is estimated by comparing the modeformer phase outputs of the spiral antenna. The compensated phase of mode 1 may be used to provide a coarse estimate of the azimuth AoA. Recognizing that higher rates of phase change, or steeper slopes of phase, with respect to azimuth produce better accuracy of the estimate, a more accurate estimate may be obtained by using the phase corresponding to a higher mode. However, azimuth estimation using a higher order mode is ambiguous. For example, mode n provides n number of azimuth estimates over of 360° of azimuth. This ambiguity may be resolved using the coarse estimate provided by mode 1 [5].

Using this described process and the actual calibrated phase data from the phase measurements performed, it is possible to conduct an experiment to test the accuracy and validity of this AoA determination technique.

4.2 Monte Carlo Azimuth Experimentation

In order to test the accuracy and validity of the comparison technique of AoA determination, multiple Monte Carlo experiments were conducted using the actual azimuth measurement data collected in the RASCAL compact range. Signal-to-noise ratio (SNR), frequency, azimuth angle, and elevation angle are the four independent parameters considered for these experiments. One parameter is varied while all others are kept constant in order to analyze the effects of each on the model. Noise is synthetically added to the experimental data, which is considered to be "pristine." For

each experiment, statistics are recorded including mean, standard deviation, bias, and the number of catastrophic failures. Catastrophic failures are defined as AoA estimates that are greater than 7.5° (azimuth) away from the true azimuth AoA. When these catastrophic failures are identified, they are not included in the final statistical analysis for each measurement set.

4.2.1 Azimuth Experiment # 1

The first experiment conducted varied SNR from 0 to 40 dB in 2.5 dB increments. Statistics were recorded at three elevation angles ($\theta = 20^\circ, 40^\circ$, and 45°) and at a frequency of 4GHz, for each of the three usable modes. This Monte Carlo experiment generated 100 ($N=100$, the number of iterations) azimuth angles, each at $\phi = 60^\circ$ (with unique noise each iteration) and the statistics were recorded from the obtained data. The following figures show the effect of SNR on the number of catastrophic failures present in the azimuth estimates of the comparison method. As predicted in the previous section, when the elevation gain of the spiral is low for a particular elevation AoA, the number of catastrophic failures in the azimuth estimates skyrocket. Mode 1 in figure 4.4 is a perfect example of this trend. Also noticeable is the drastic decrease of the number of catastrophic failures as SNR increases for each elevation angle case; this alludes to the increase in accuracy for all estimates. The standard deviation is also shown below as a function of and possesses similar traits as those of the catastrophic failures. Figures 4.2-4 show the results for spiral one, while figures 4.5-7 show the results for spiral two; figures 4.2-4.7 are cases at 4GHz for SNR vs. the number of catastrophic failures. Figures 4.8-10 show the results for spiral one, while figures 4.11-4.13 show the results for spiral two; figures 4.8-4.13 are cases at 4GHz for SNR vs. standard deviation.

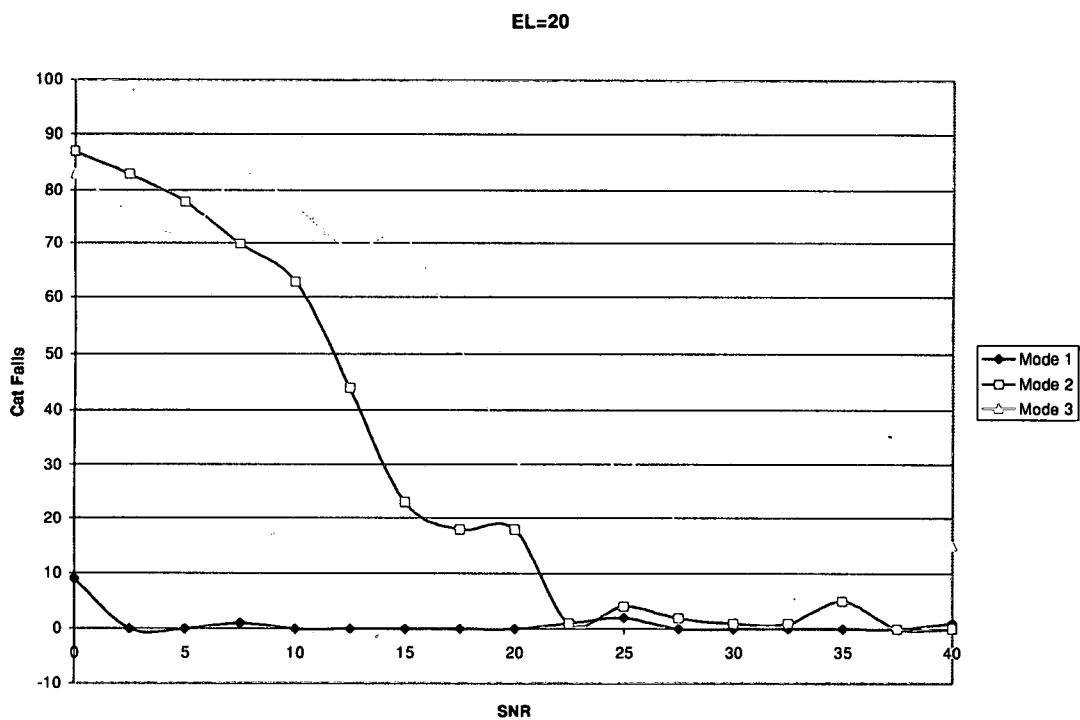


Figure 4.2: SNR vs. # of catastrophic failures for $\theta = 20^\circ$, spiral # 1, at 4GHz.

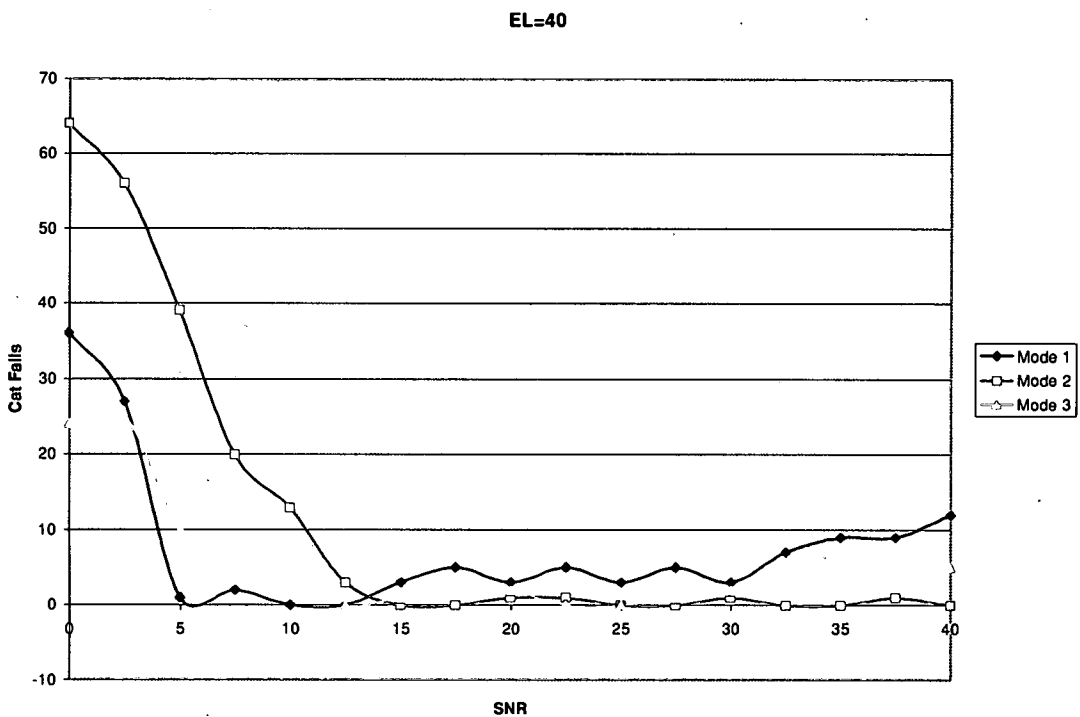


Figure 4.3: SNR vs. # of catastrophic failures for $\theta = 40^\circ$, spiral # 1, at 4GHz.

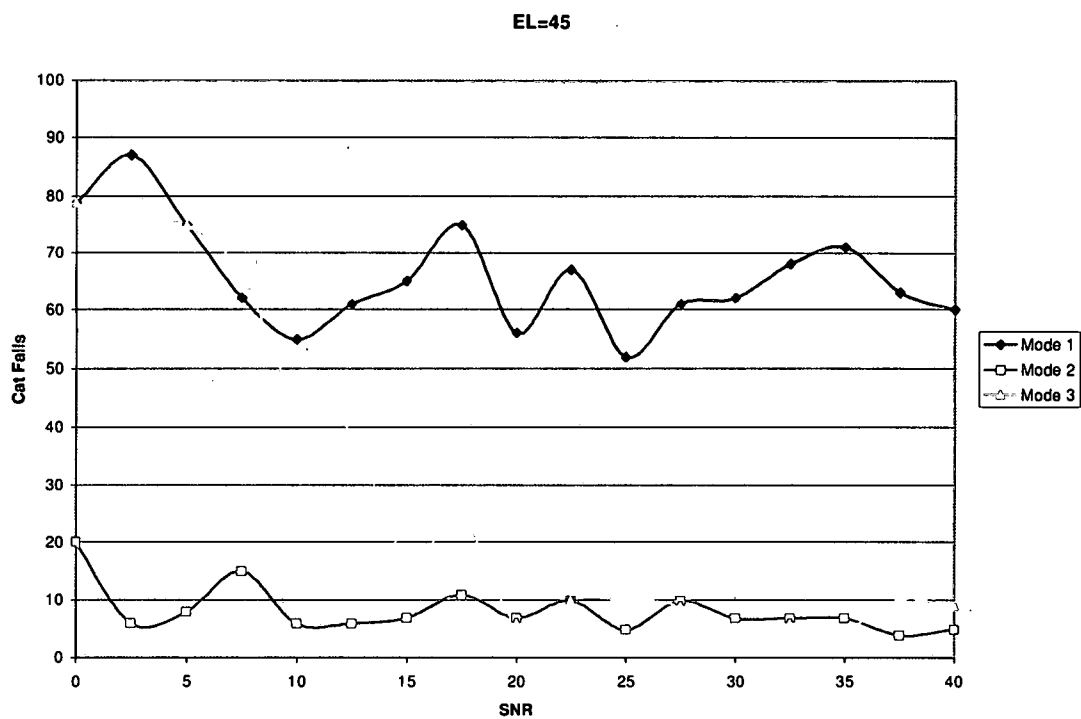


Figure 4.4: SNR vs. # of catastrophic failures for $\theta = 45^\circ$, spiral # 1, at 4GHz.

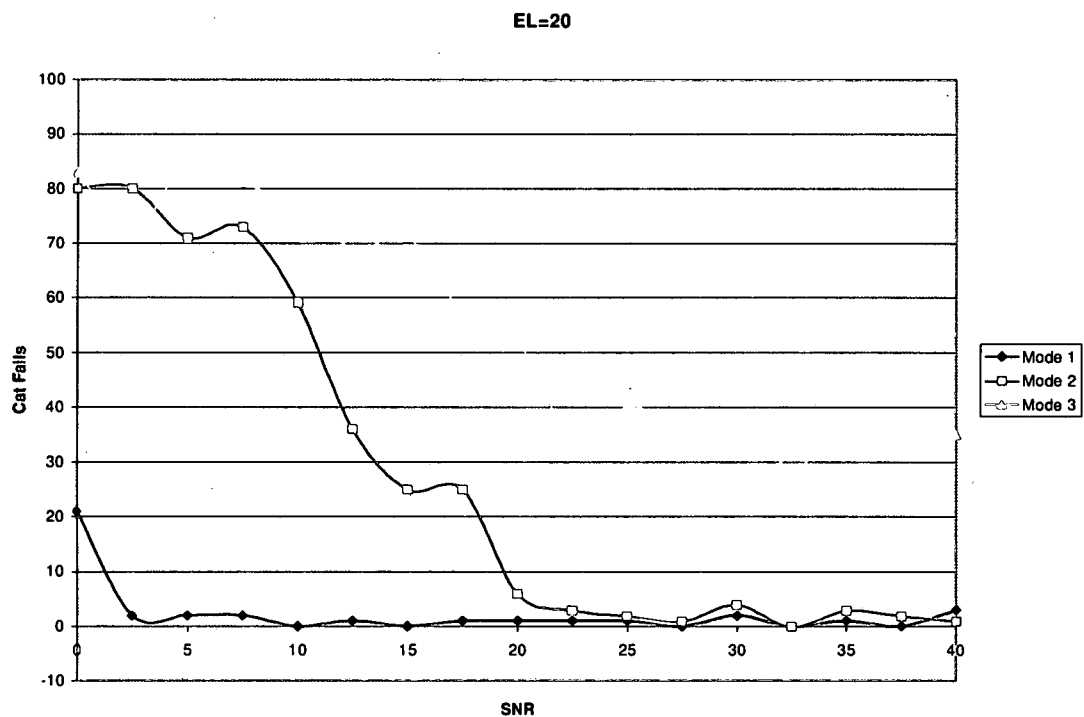


Figure 4.5: SNR vs. # of catastrophic failures for $\theta = 20^\circ$, spiral # 2, at 4GHz.

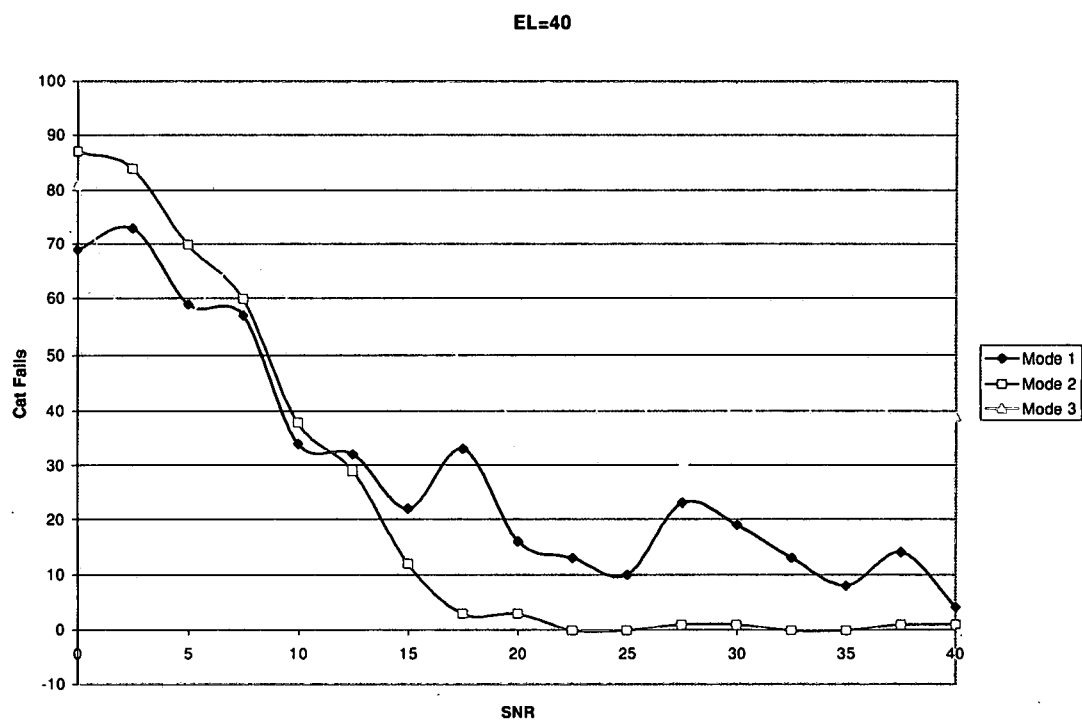


Figure 4.6: SNR vs. # of catastrophic failures for $\theta = 40^\circ$, spiral # 2, at 4GHz.

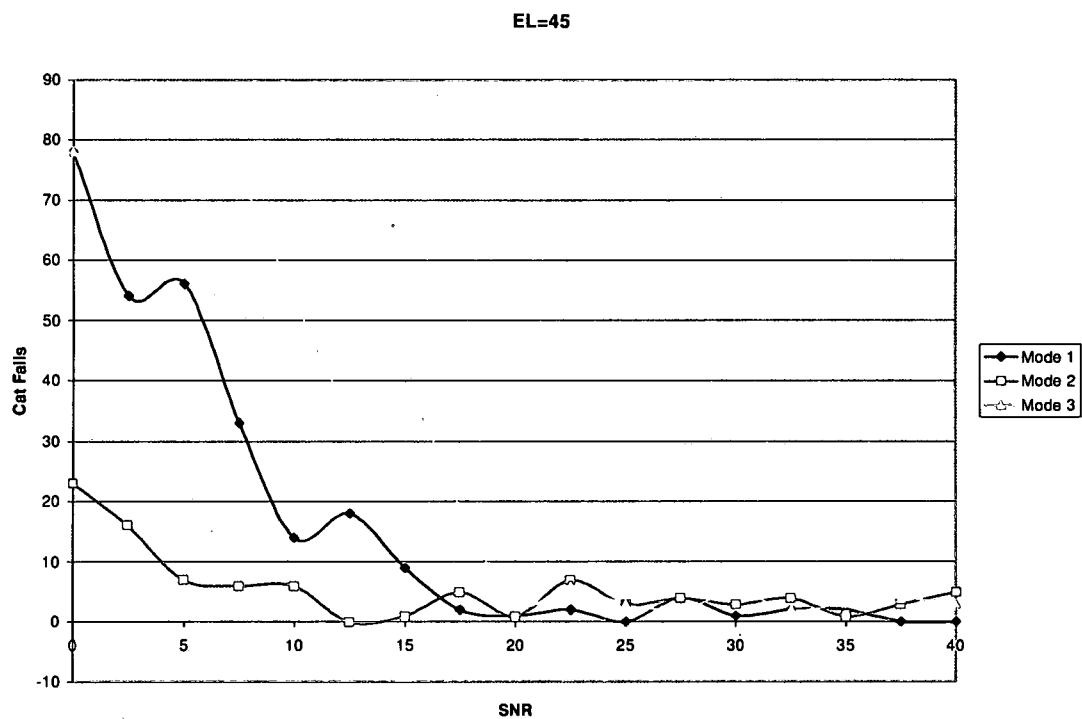


Figure 4.7: SNR vs. # of catastrophic failures for $\theta = 45^\circ$, spiral # 2, at 4GHz.

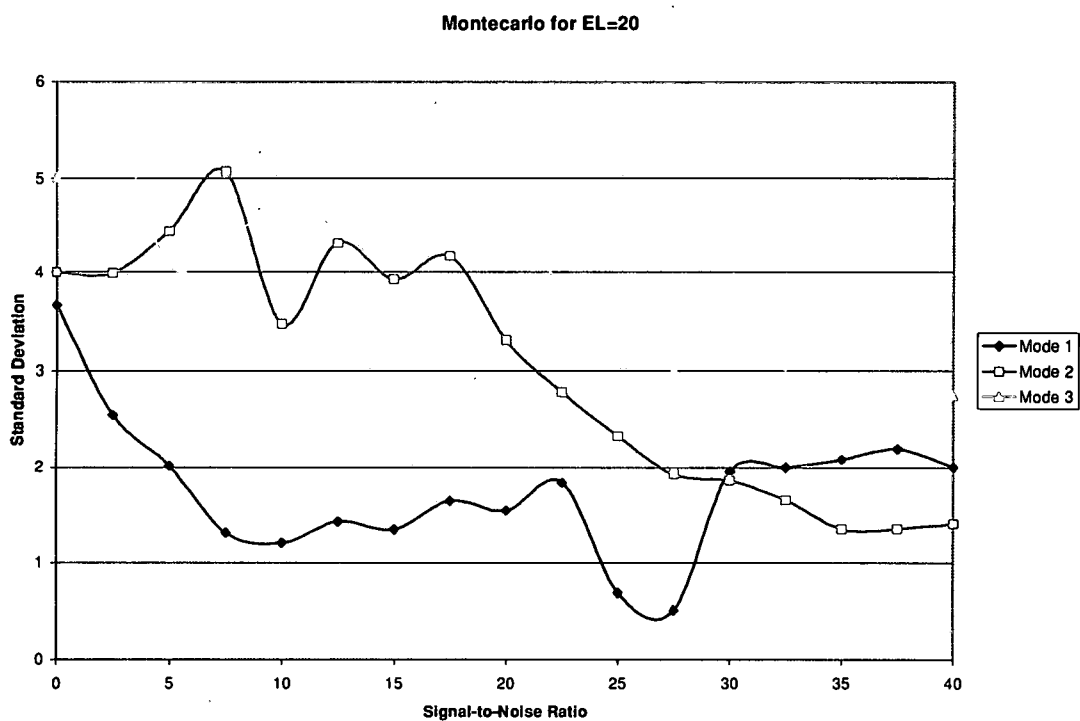


Figure 4.8: SNR vs. # standard deviation for $\theta = 20^\circ$, spiral # 1, at 4GHz.

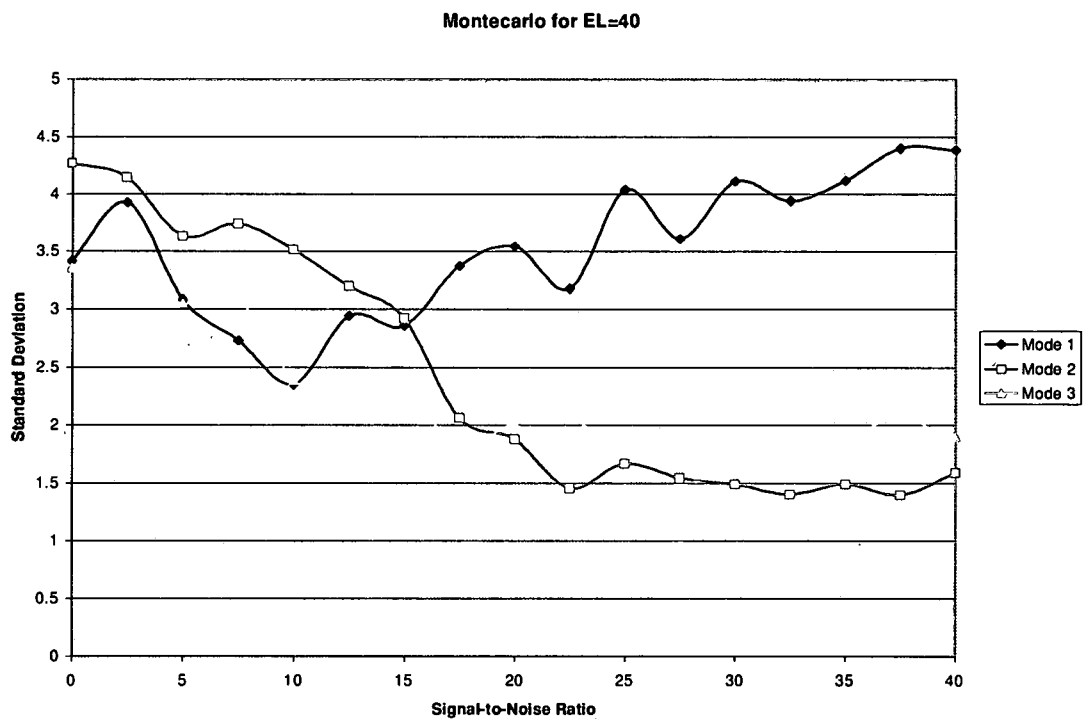


Figure 4.9: SNR vs. # standard deviation for $\theta = 40^\circ$, spiral # 1, at 4GHz.

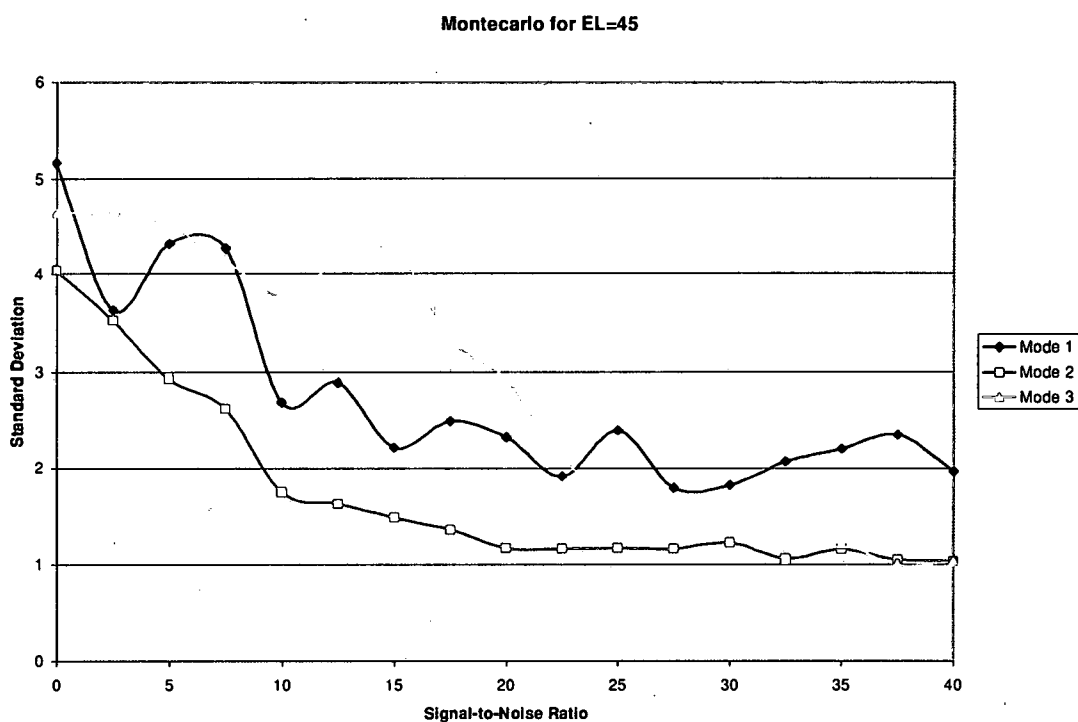


Figure 4.10: SNR vs. # standard deviation for $\theta = 45^\circ$, spiral # 1, at 4GHz.

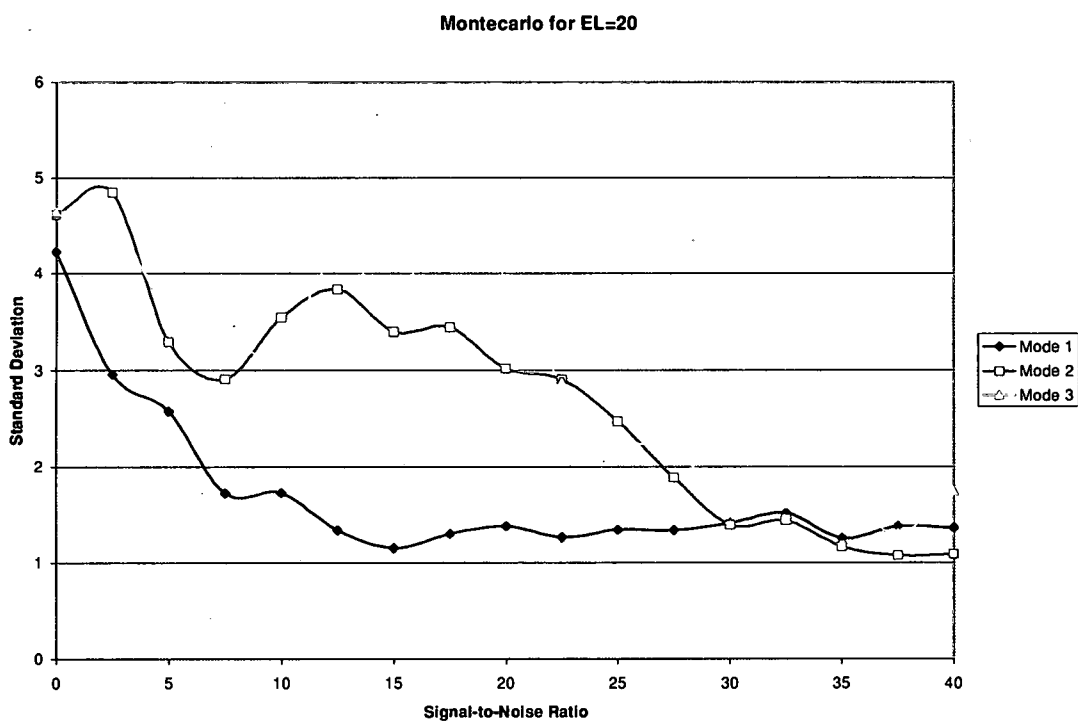


Figure 4.11: SNR vs. # standard deviation for $\theta = 20^\circ$, spiral # 2, at 4GHz.

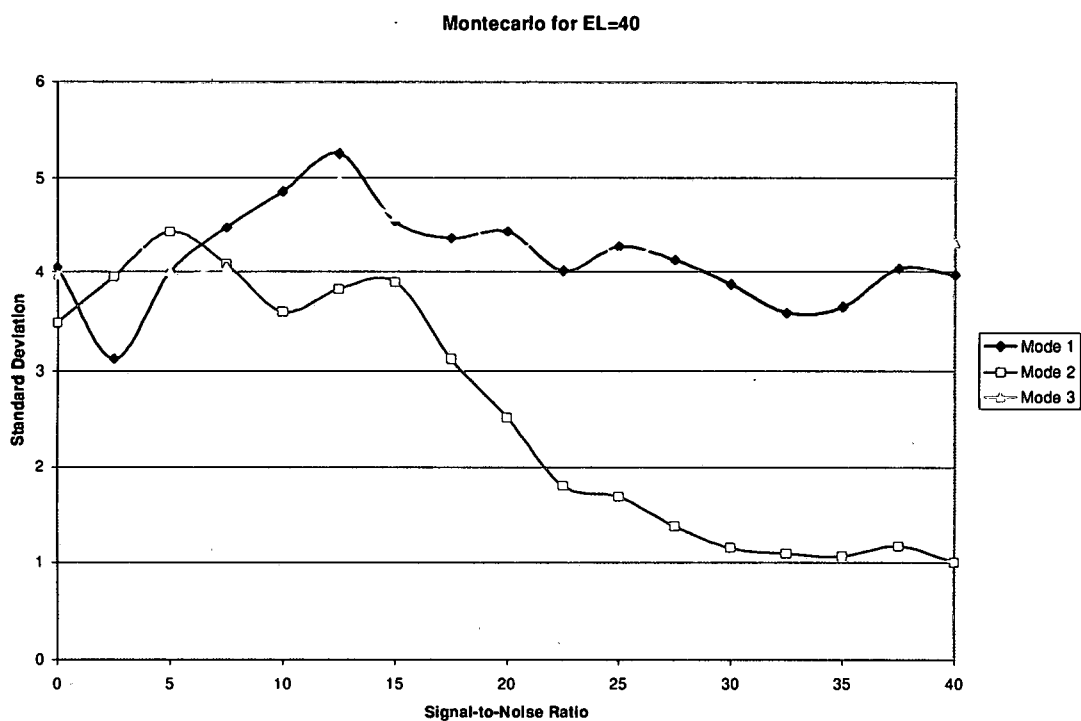


Figure 4.12: SNR vs. # standard deviation for $\theta = 40^\circ$, spiral # 2, at 4GHz.

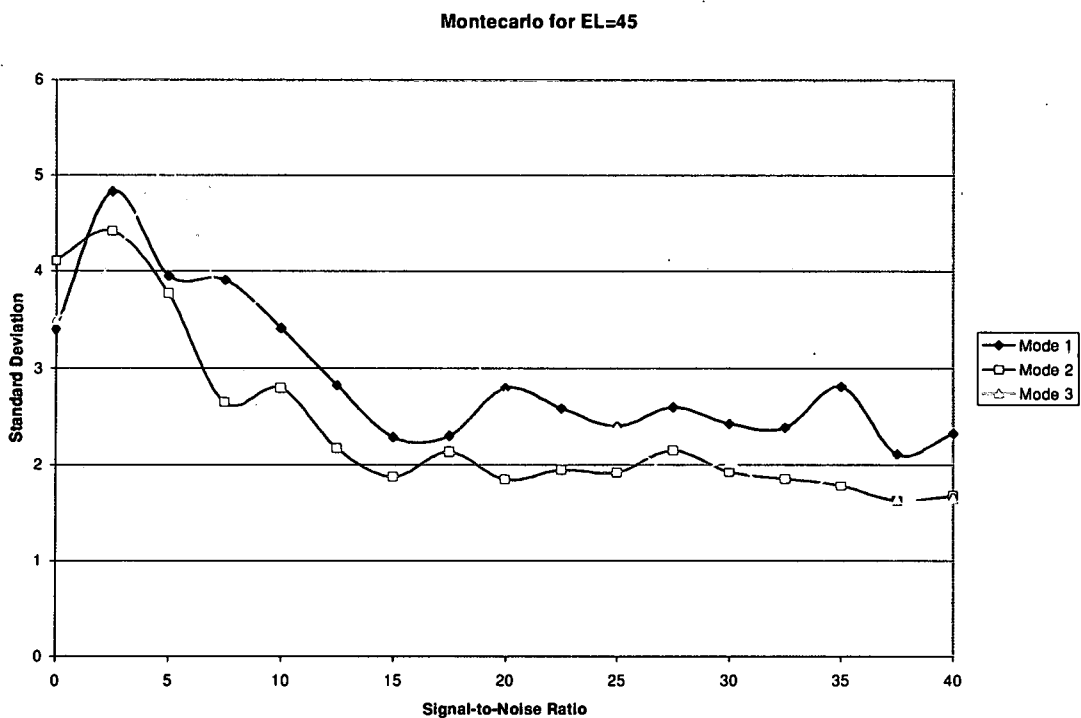


Figure 4.13: SNR vs. # standard deviation for $\theta = 45^\circ$, spiral # 2, at 4GHz.

It is also of worth to compare the experiment one results of both spirals. The azimuth estimates for spiral one and two at an elevation angle of $\theta = 20^\circ$, or figures 4.2 and 4.5, show utmost consistency in the number of catastrophic failures and the increase of accuracy as SNR increases. However, the azimuth estimates for the next two cases, $\theta = 40^\circ$ and $\theta = 45^\circ$, contain some inconsistencies between spiral one and spiral two. It is apparent in figures 4.3 and 4.6, for $\theta = 40^\circ$, that a slight quirk exists between each spiral's results; spiral one in figure 4.3 contains almost flawless results while spiral two in figure 4.6 possesses much higher numbers of catastrophic failures for modes 1 and 3 between SNR = 15 dB and SNR = 40 dB. A similar case is made for figures 4.4 and 4.7, for $\theta = 45^\circ$, where spiral two's results are pristine and spiral one's mode 1 results contain a high number of catastrophic failures also between SNR = 15 dB and SNR = 40 dB. It may be peculiar that spiral two's data is so good for mode 1 when the elevation angle under test in figure 4.7 is so far away from boresight, as mentioned earlier in this section. Similar results may be found in the above standard deviation results, figures 4.8-4.13.

4.2.2 Azimuth Experiment # 2

The second experiment conducted varied frequency from 4-12GHz at three values: 4, 8, and 12GHz. SNR was kept constant at 20 dB. Monte Carlo experiment number two generated 100 random azimuth angles from $\phi = 0^\circ - 360^\circ$ and the statistics were recorded from the obtained data. Cases were run for three elevation angles ($\theta = 20^\circ$, 40° , and 45°) for each of the three usable modes. Results from this experiment were very simple relationships. As frequency increased, the number of catastrophic failures drastically increased for each case; this in turn raised the standard deviation for each respective case. Table 4.1 and 4.2 display the catastrophic failure and standard deviation data from this experiment for antennas one and two, respectively. The number of catastrophic failures always increased as frequency increased; the highlighted cells display the cases that did not follow the trend of increased frequency, increased standard deviation.

Mode 1, SNR=20			$\theta = 20$			$\theta = 40$			$\theta = 45$		
Frequency			Std	# of catfails		Std	# of catfails		Std	# of catfails	
4			1.7089	2		3.6327	5		2.3685	60	
8			4.1333	32		5.1595	46		4.0234	63	
12			4.1989	68		4.4287	72		2.4792	91	

Mode 2, SNR=20			$\theta = 20$			$\theta = 40$			$\theta = 45$		
Frequency			Std	# of catfails		Std	# of catfails		Std	# of catfails	
4			3.514	12		1.562	1		1.3052	8	
8			4.8083	66		3.3168	10		2.5001	16	
12			3.771	63		3.0061	12		3.0769	19	

Mode 3, SNR=20			$\theta = 20$			$\theta = 40$			$\theta = 45$		
Frequency			Std	# of catfails		Std	# of catfails		Std	# of catfails	
4			3.5909	32		1.8251	0		2.5658	10	
8			3.3056	63		2.5644	2		2.5883	12	
12			4.2886	77		3.3878	9		3.5241	45	

Table 4.1: Standard Deviation and catastrophic failures versus frequency for spiral # 1.

Mode 1, SNR=20			$\theta = 20$			$\theta = 40$			$\theta = 45$		
Frequency			Std	# of catfails		Std	# of catfails		Std	# of catfails	
4			1.143	0		4.0364	21		2.741	1	
8			2.4229	0		3.1134	67		3.1853	70	
12			3.9938	66		4.6708	73		4.3517	68	

Mode 2, SNR=20			$\theta = 20$			$\theta = 40$			$\theta = 45$		
Frequency			Std	# of catfails		Std	# of catfails		Std	# of catfails	
4			3.4951	5		2.4088	0		1.7188	7	
8			4.5972	47		3.7655	20		2.4996	29	
12			4.2996	61		4.3165	49		4.3211	28	

Mode 3, SNR=20			$\theta = 20$			$\theta = 40$			$\theta = 45$		
Frequency			Std	# of catfails		Std	# of catfails		Std	# of catfails	
4			3.8797	55		4.8414	52		2.4672	8	
8			3.8201	70		3.9133	43		3.1503	31	
12			3.7227	67		3.4925	33		3.1683	44	

Table 4.2: Standard Deviation and catastrophic failures versus frequency for spiral # 2.

This trend proves an observation made in the last sentence of section three: "it is reasonable to expect this increased "ripple" [present in the phase measurements of the

upper frequency band] to manifest as increased variance in the azimuth angle estimates at the higher end of the band.” However, the maximum standard deviation present in this experiment was only 5.15° (Spiral 1, Mode 1, $\theta = 40^\circ$).

4.2.3 Azimuth Experiment # 3

The third and final Monte Carlo experiment generated 100 iterations of each of eight azimuth angles, two per each quadrant of coverage, which were chosen randomly ahead of time. These angles were $\phi = 30^\circ, 60^\circ, 135^\circ, 150^\circ, 200^\circ, 225^\circ, 300^\circ$, and 330° . 100 realizations of the modal outputs were taken for each of these azimuth values for the three elevation angles ($\theta = 20^\circ, 40^\circ$, and 45°), three frequencies (4, 8, and 12GHz), and SNR=20 dB for each of the three usable modes. The statistics were recorded from the obtained data. The mean of each of the three frequencies for spiral one are shown in figures 4.14-16.

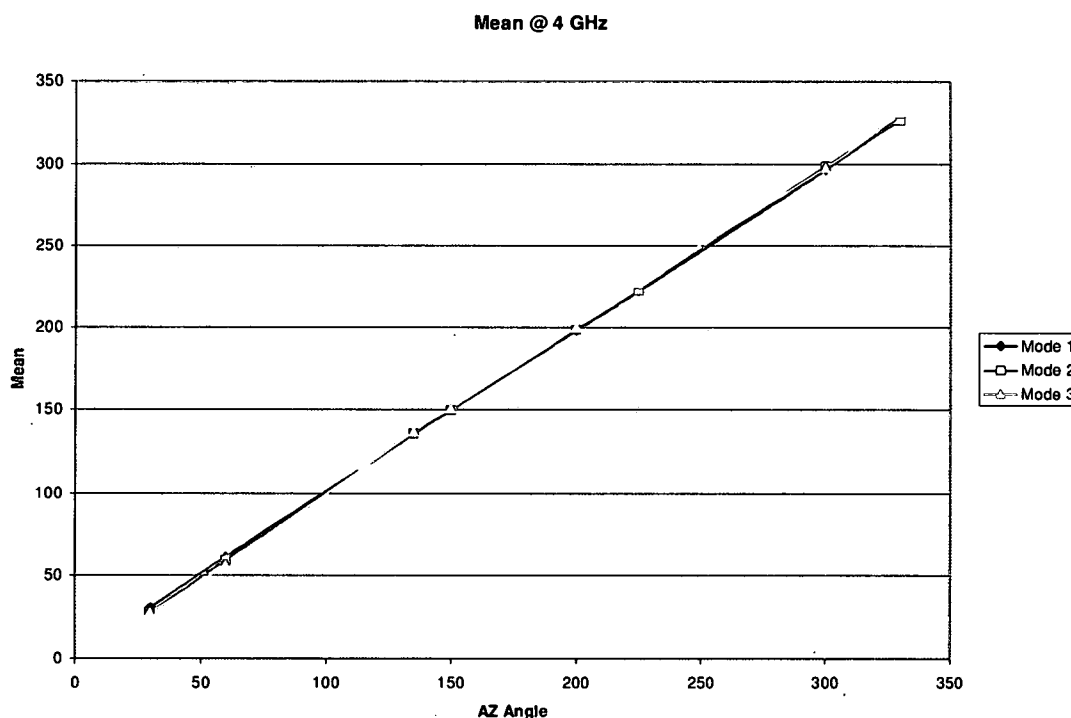


Figure 4.14: Mean of azimuth estimates for spiral # 1 at 4GHz.

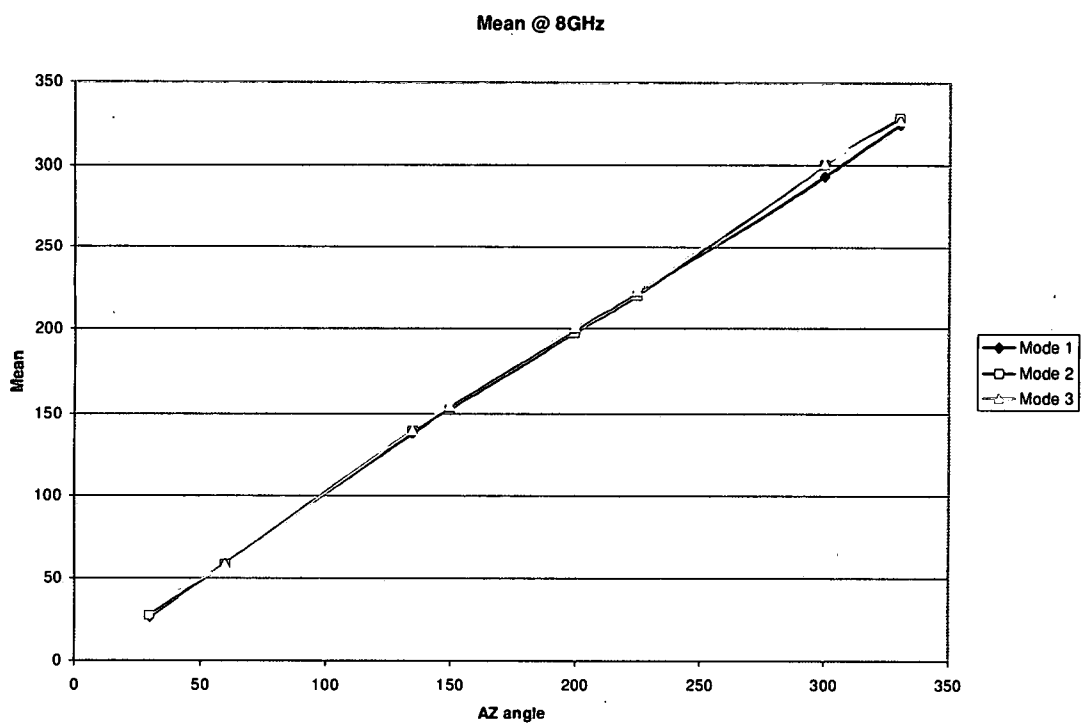


Figure 4.15: Mean of azimuth estimates for spiral # 1 at 8GHz.

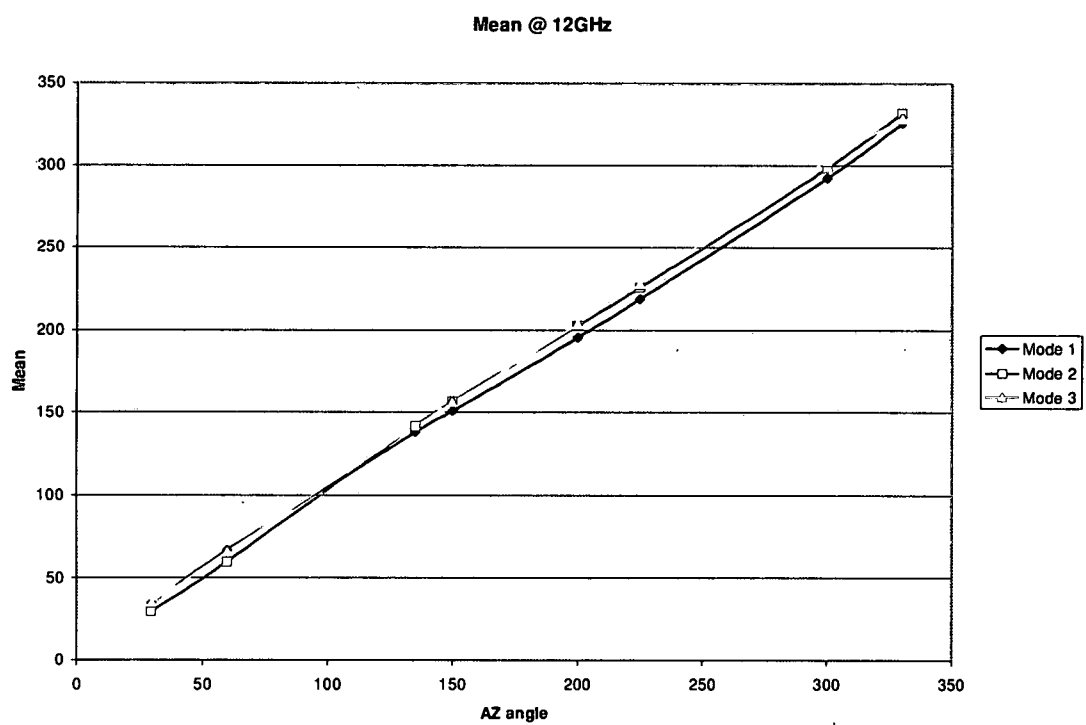


Figure 4.16: Mean of azimuth estimates for spiral # 1 at 12GHz.

The linearity and constant slopes of the above mean versus azimuth graphs indicate that the mean of the actual azimuth estimates is very close in value to the actual azimuth angles. This is in fact, true: the average bias for mode 1, 2, and 3 in the above graphs are shown in table 4.3, below.

Mode	Figure		
	4.14	4.15	4.16
1	1.520888°	3.68665°	4.750437°
2	1.516915°	2.610575°	2.728913°
3	2.061863°	2.902688°	4.4703°

Table 4.3: Average bias of experiment # 3 estimates for spiral # 1.

Noticing the trends in table 4.3, one can observe that as frequency increases, the average bias of estimates increases. We can again relate this trend back to the final paragraph of section 3, as in the 2nd experiment. It may be beneficial to note that the average bias of estimates for this entire experiment is 2.916°. It should also be mentioned that the number of catastrophic failures present in this experiment is drastically reduced from the previous experiments. The entire set of 4GHz estimates for this experiment contains zero catastrophic failures out of 2400 trials (24 angles of 100 iterations each)! The 8GHz set of estimates contains 187 failures out of 2400 trials (7.79%). As expected, the 12GHz set of estimates contains the most catastrophic failures, 1005 out of 2400, or 41.8%.

The same experiment was conducted on spiral two and the statistics were recorded from the obtained data. The mean of each of the three frequencies for spiral one are shown in figures 4.17-19.

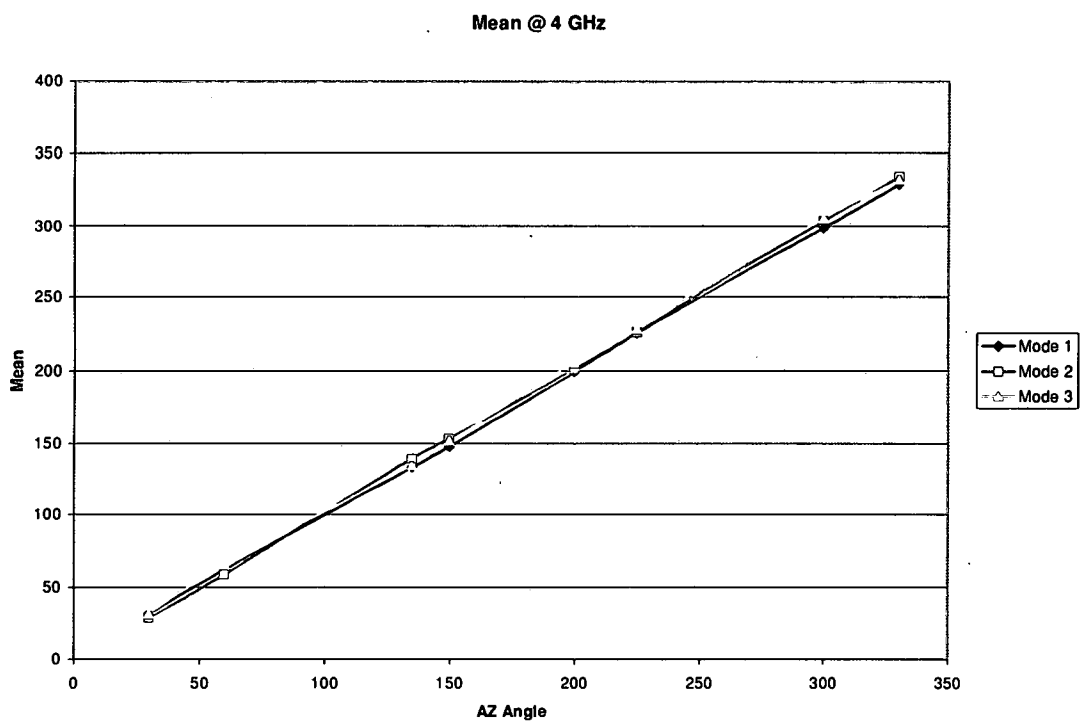


Figure 4.17: Mean of azimuth estimates for spiral # 2 at 4GHz.

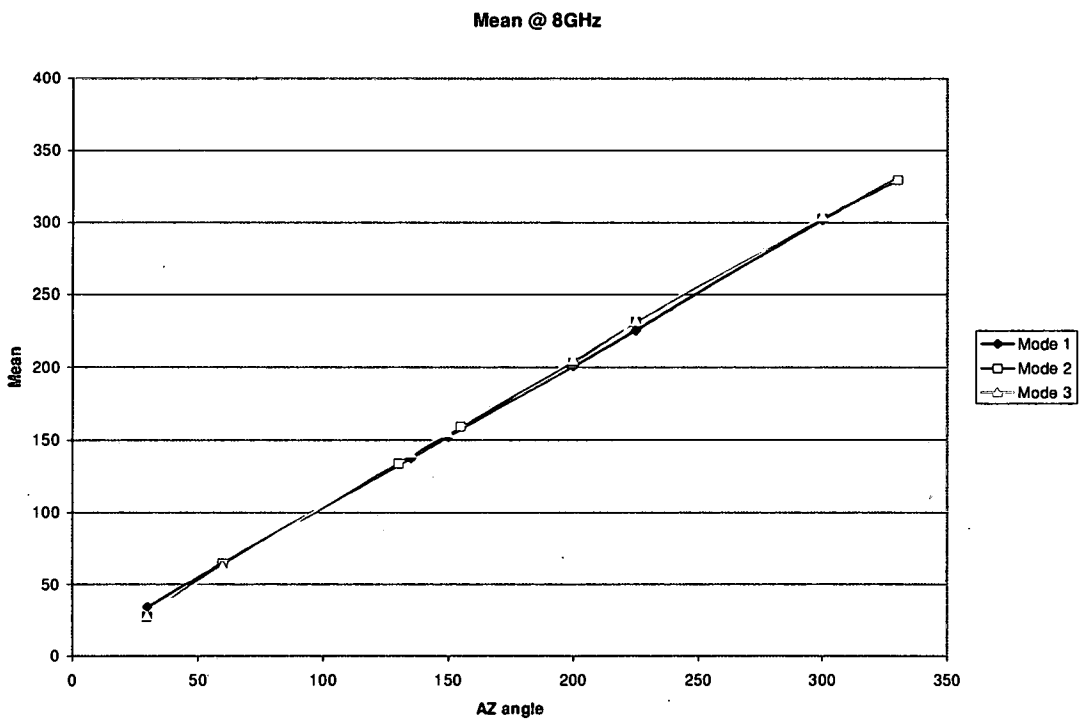


Figure 4.18: Mean of azimuth estimates for spiral # 2 at 8GHz.

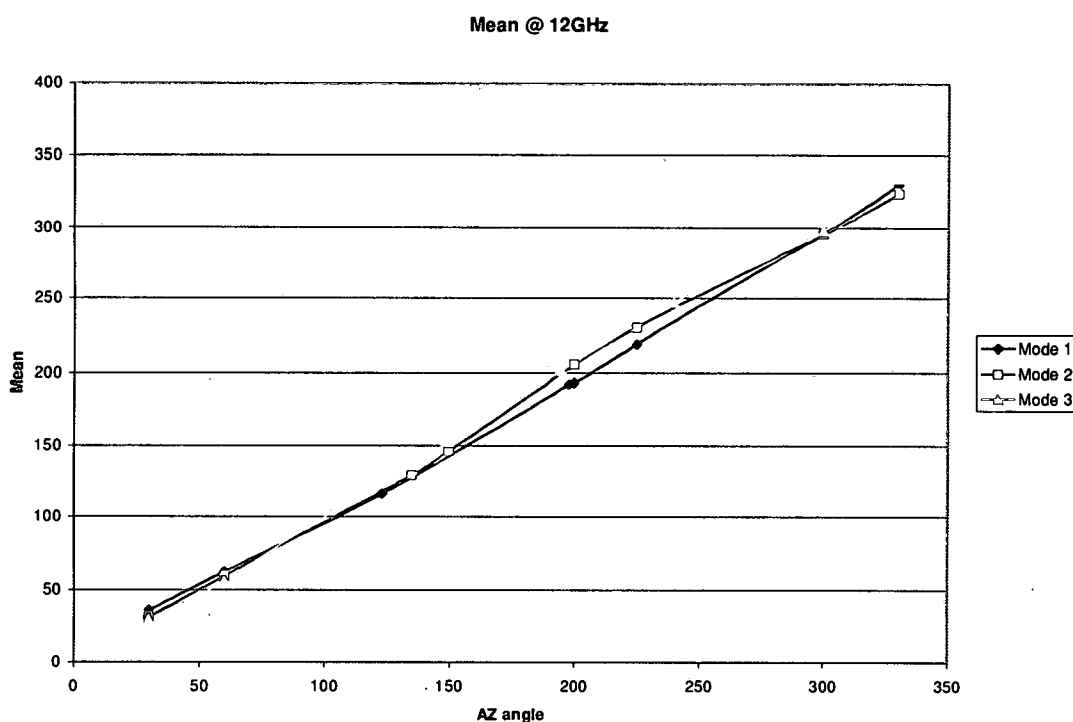


Figure 4.19: Mean of azimuth estimates for spiral # 2 at 12GHz.

The linearity and constant slopes of the spiral two mean versus azimuth graphs indicate that the mean of the actual azimuth estimates are again very close in value to the actual azimuth angles. This is in fact, true: the average bias for mode 1, 2, and 3 in the spiral two graphs are shown in table 4.4.

Figure			
Mode	4.17	4.18	4.19
1	1.229013°	2.26085°	4.820588°
2	2.868025°	3.52545°	3.933175°
3	3.52215°	4.878238°	3.746638°

Table 4.4: Average bias of experiment # 3 estimates for spiral # 2.

Noticing the trends in table 4.4, one can observe that as frequency increases, the average bias of estimates increases—except for figure 4.18 (mode 3 at 8GHz). This single inconsistency in this trend may be attributed to the “ripple” in the phase data. We can again relate this trend back to the final paragraph of section 3, as in the 2nd

experiment. It may be beneficial to note that the average bias of estimates for this entire experiment is 3.420° , only slightly higher ($.496^\circ$) than spiral one. The entire set of 4GHz estimates for spiral two contains only 72 catastrophic failures out of 2400 trials (3.0%). The 8GHz set of estimates contains 267 failures out of 2400 trials (11.1%). As expected, the 12GHz set of estimates contains the most catastrophic failures, 1078 out of 2400, or 44.9%. These statistics are comparable to the results for spiral one; the differences for the frequency sets between the two antennas (spiral two minus spiral one) is 3.0%, 3.31%, and 3.1%, respectively.

4.3 Monte Carlo Elevation Experimentation

In order to test the accuracy and validity of the comparison technique of AoA determination, multiple Monte Carlo experiments were conducted using the actual elevation measurement data collected in the RASCAL compact range. Signal-to-noise ratio (SNR), frequency, and elevation angle are the three independent variables considered for these experiments. The azimuth angle under investigation is constant over the three experiments at $\phi = 180^\circ$. One variable is varied while all others are kept constant in order to analyze the effects of each on the model. Noise is synthetically added to the experimental data, which is considered to be "pristine." For each experiment, statistics are recorded including mean, standard deviation, bias, and the number of catastrophic failures. Catastrophic failures are defined as AoA estimates that are greater than 7.5° (elevation) away from the true elevation AoA. When these catastrophic failures are identified, they are not included in the final statistical analysis for each measurement set.

Elevation angle estimates are gathered from the elevation pattern modal ratios (m_2/m_1 and m_3/m_1) presented at the end of chapter 3 in figures 3.37-3.42. These ratios are formed directly from the elevation modal patterns also presented in chapter 3 in figures 3.27-3.36. From this table of values, it is possible to "fit" a low order polynomial very accurately when it is of the form,

$$r = f(\theta). \quad (4.3)$$

Here ' r ' is the modal ratio value and ' θ ' is the elevation angle. However, it is more convenient to express the elevation angle estimate as a function of the observed modal ratio, even though the order of the polynomial required to yield adequate accuracy is quite high. That is,

$$\hat{\theta} = g(r) \quad (4.4)$$

Where r is again the modal ratio value and ' $\hat{\theta}$ ' is the elevation angle estimate. We will set up $g(r)$ as a 3rd order polynomial (4 coefficients) in order to estimate the elevation angle of an incoming signal. From the table of measured values, we assign a polynomial which approximates the table. Instead of storing the entire table, we merely store the polynomial coefficients. A polynomial fit is required for each azimuth angle, defining a semi-infinite plane. Though theory predicts, based on symmetry requirements, that modal ratios must remain the same for the semi-infinite planes defined by ϕ and $\phi + 180^\circ$, in practice, perfect symmetry does not exist and a different polynomial fit must be determined for modal ratio corresponding to each semi-infinite plane defined by a given azimuth angle. Figure 4.20 shows the original modal ratios for the $\phi=0^\circ$ and $\phi=180^\circ$ planes and the absence of symmetry may be noted. Figure 4.21 shows the initial modal ratios and the overlaid 3rd order polynomials from which the elevation estimates are generated.

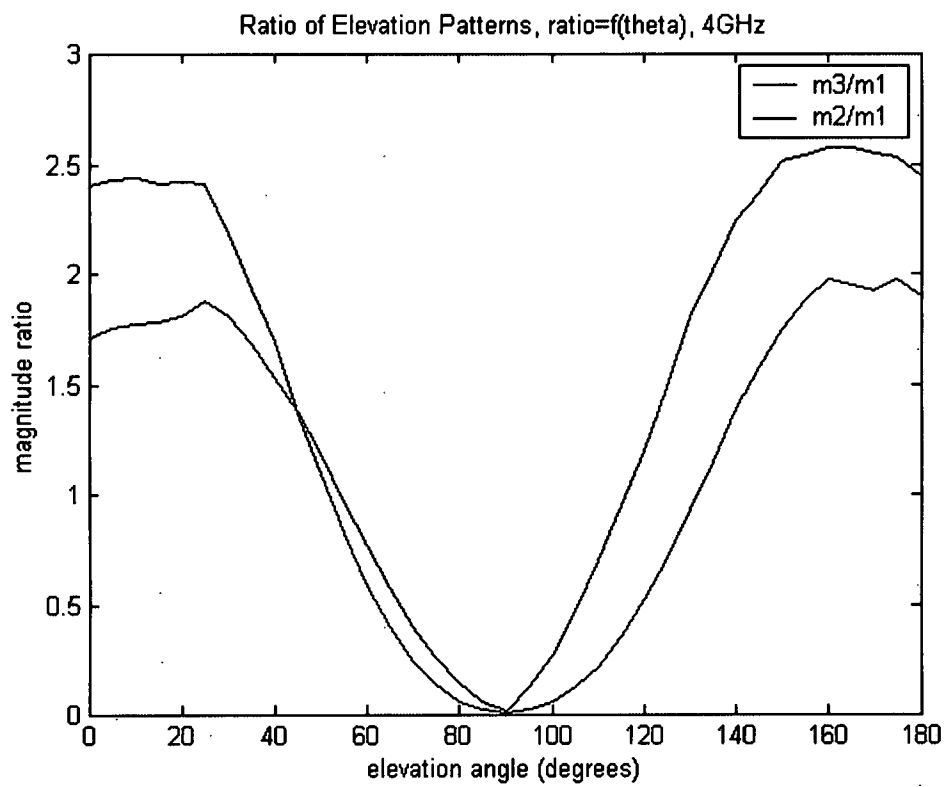


Figure 4.20: Ratio of modal elevation patterns of the form $r = f(\theta)$.

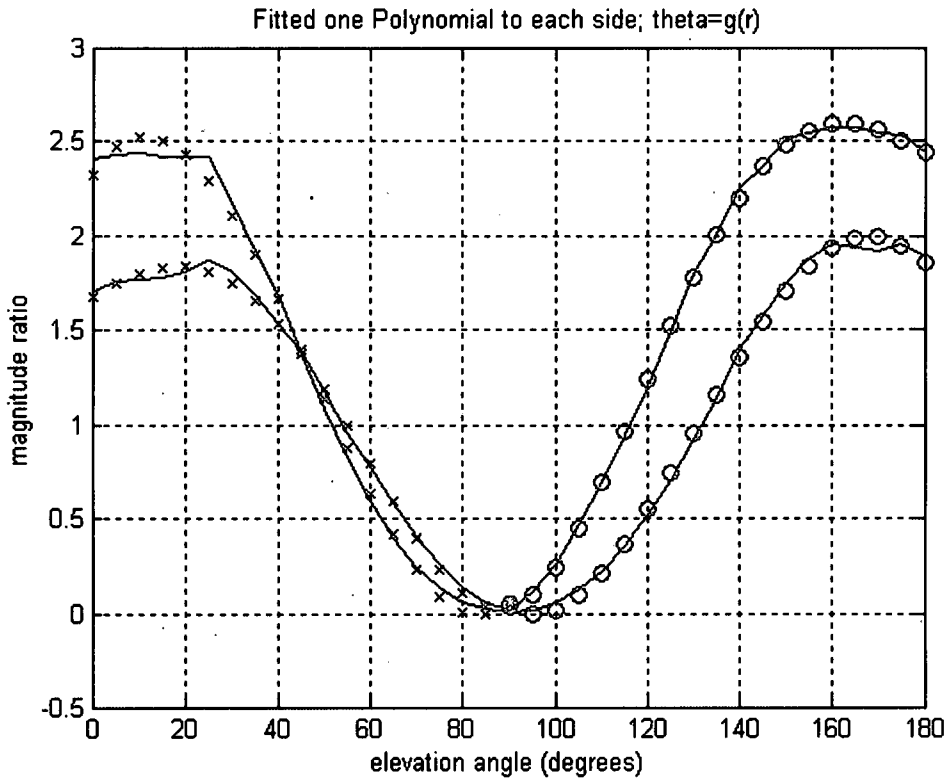


Figure 4.21: Fitted polynomials to each side of the modal ratios of the form $\hat{\theta} = g(r)$.

The continuous lines above are the actual modal ratio data; the symbols 'x' and 'o' represent the polynomial data fit. Also note that these estimates generated will be unreliable near the horizons, as predicted in the observations at the end of chapter 3.

Using $\hat{\theta}$ as an initial guess, we can refine $\hat{\theta}$ by solving for the roots of a familiar equation, slightly altered from its form in equation 4.3, that will give us $\hat{\theta}_{refined}$:

$$f(\theta) - r = 0 \quad (4.5)$$

This method will refine the coarse estimate obtained by equation 4.4. It was hopeful that the $\hat{\theta}_{refined}$ estimate would improve the initial elevation angle estimate, especially near the horizon; however, these refined estimates did not improve upon the coarse estimates near the horizon and therefore are not included in the data presented in the following section.

4.2.4 Elevation Experiment # 1

This Monte Carlo experiment varied the SNR from 0 to 40 dB in 2.5 dB increments. Statistics were recorded for angle estimates based on both modal ratios at elevation angles of 5°, 10°, 20°, 30°, 40°, 50°, 60°, 70°, 75°, and 80° for three frequencies ($f = 4, 8, \text{ and } 12\text{GHz}$). This Monte Carlo experiment generated 100 ($N=100$, the number of iterations) elevation angles, each at an azimuth angle of $\phi = 180^\circ$ (with unique noise each iteration) and the statistics were recorded from the obtained data. The calibration process is different for each spiral antenna; therefore, the results from each antenna in this experiment are similar and only the results from spiral #1 are presented below. Shown in the figures below are plots of the number of catastrophic failures versus SNR for spiral #1 using the comparison method. The estimates based on mode 2-1 ratio are always shown in blue, and the estimates based on mode 3-1 ratio are always shown in yellow. The main coverage section of the elevation modal patterns, $\theta = 20^\circ\text{--}60^\circ$, is used in this analysis in figures 4.22-4.36 in 10° intervals each at the three different frequencies.

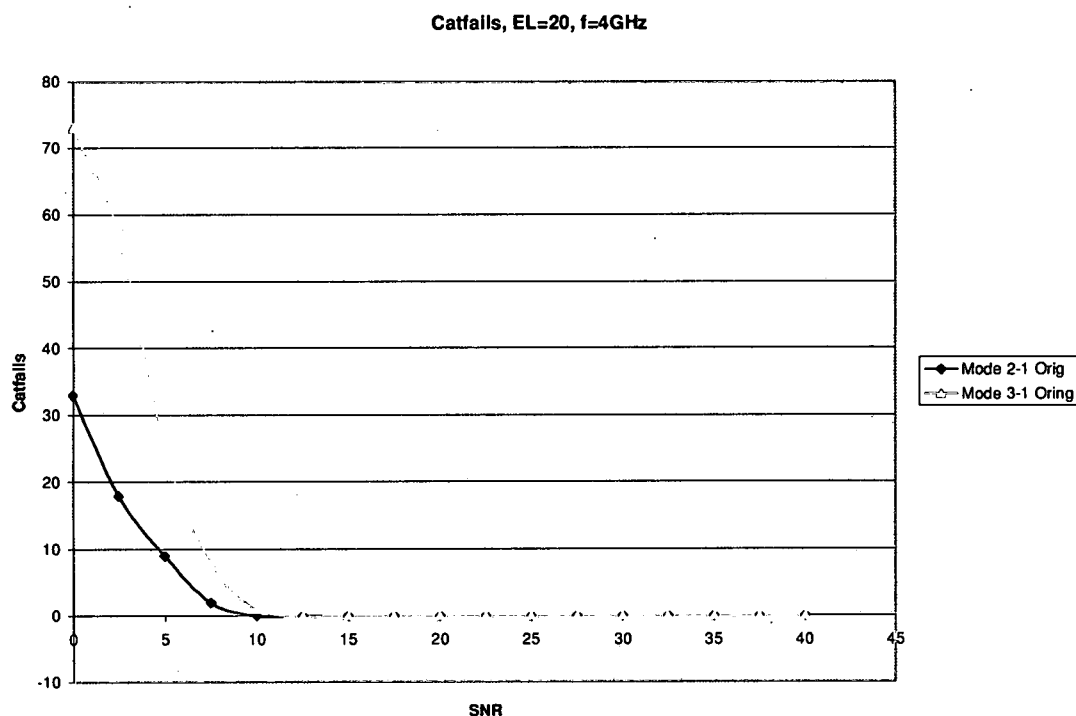


Figure 4.22: SNR vs. # of catastrophic failures for $\theta = 20^\circ$, spiral # 1, at 4GHz.

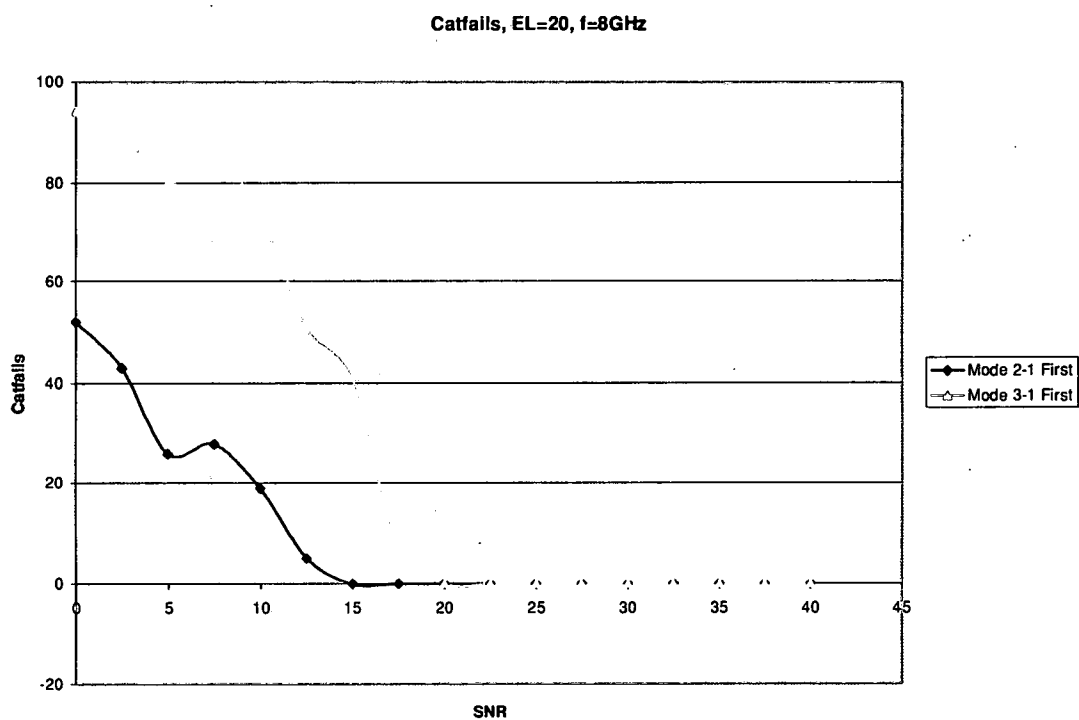
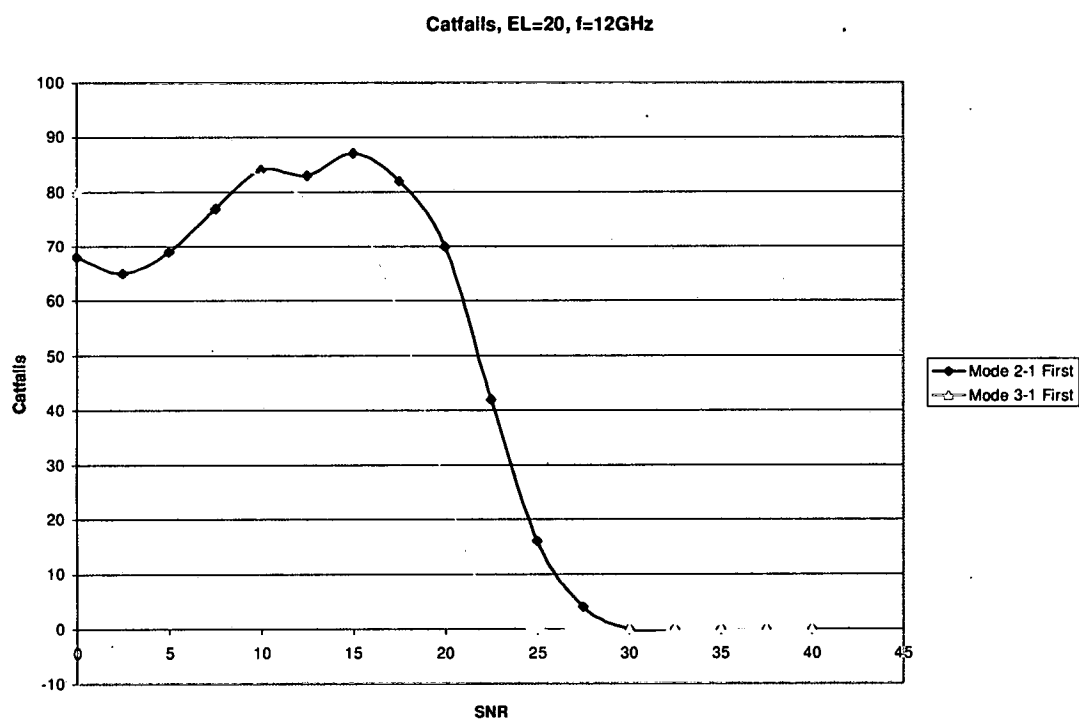


Figure 4.23: SNR vs. # of catastrophic failures for $\theta = 20^\circ$, spiral # 1, at 8GHz.



4.24: SNR vs. # of catastrophic failures for $\theta = 20^\circ$, spiral # 1, at 12GHz.

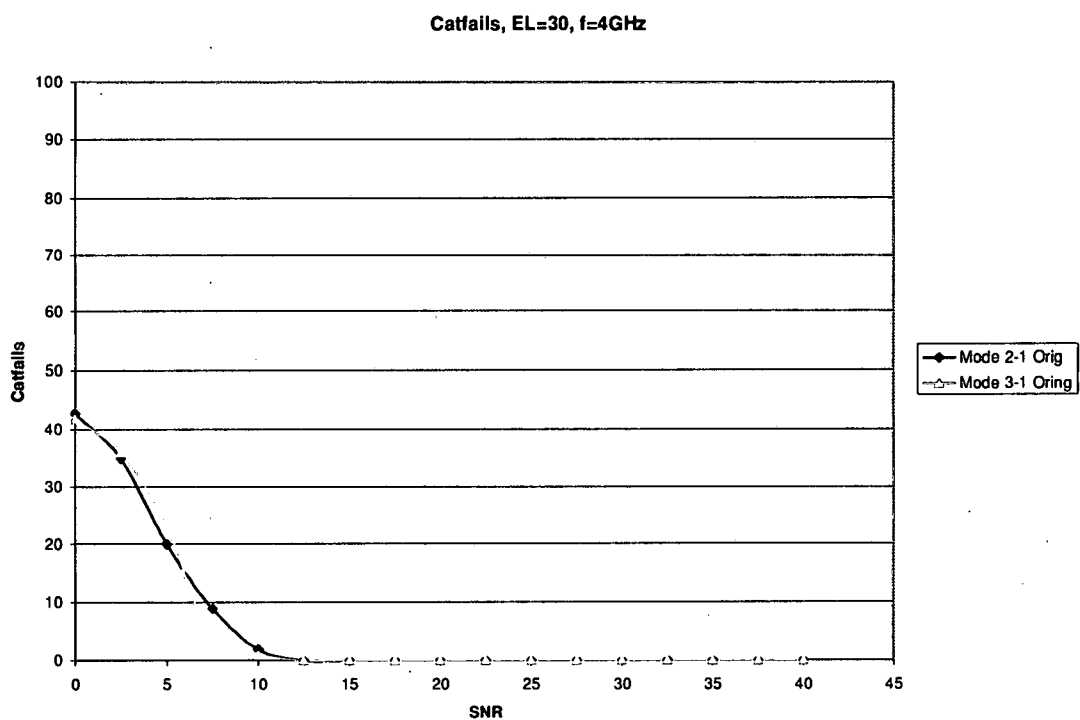


Figure 4.25: SNR vs. # of catastrophic failures for $\theta = 30^\circ$, spiral # 1, at 4GHz.

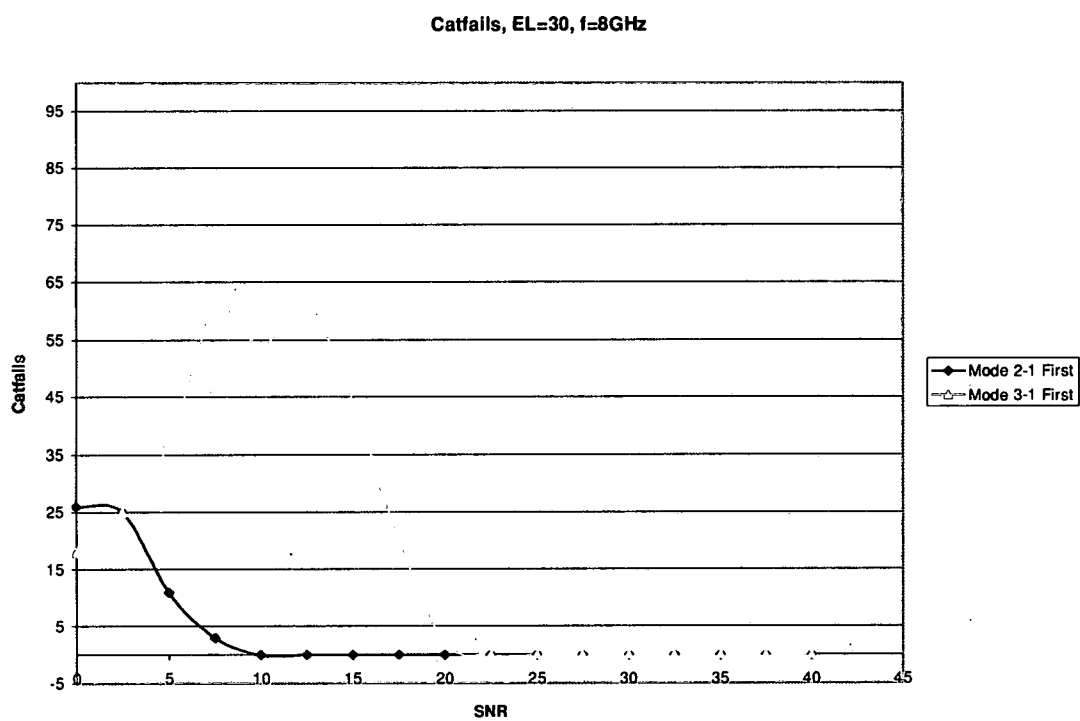


Figure 4.26: SNR vs. # of catastrophic failures for $\theta = 30^\circ$, spiral # 1, at 8GHz.

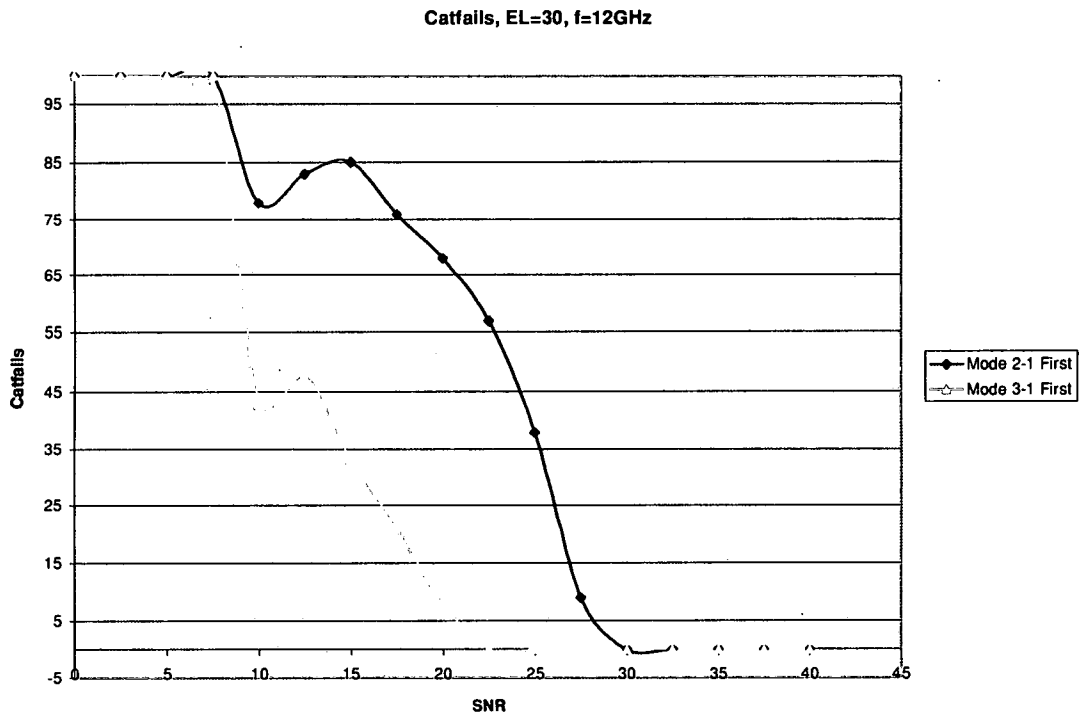


Figure 4.27: SNR vs. # of catastrophic failures for $\theta = 30^\circ$, spiral # 1, at 12GHz.

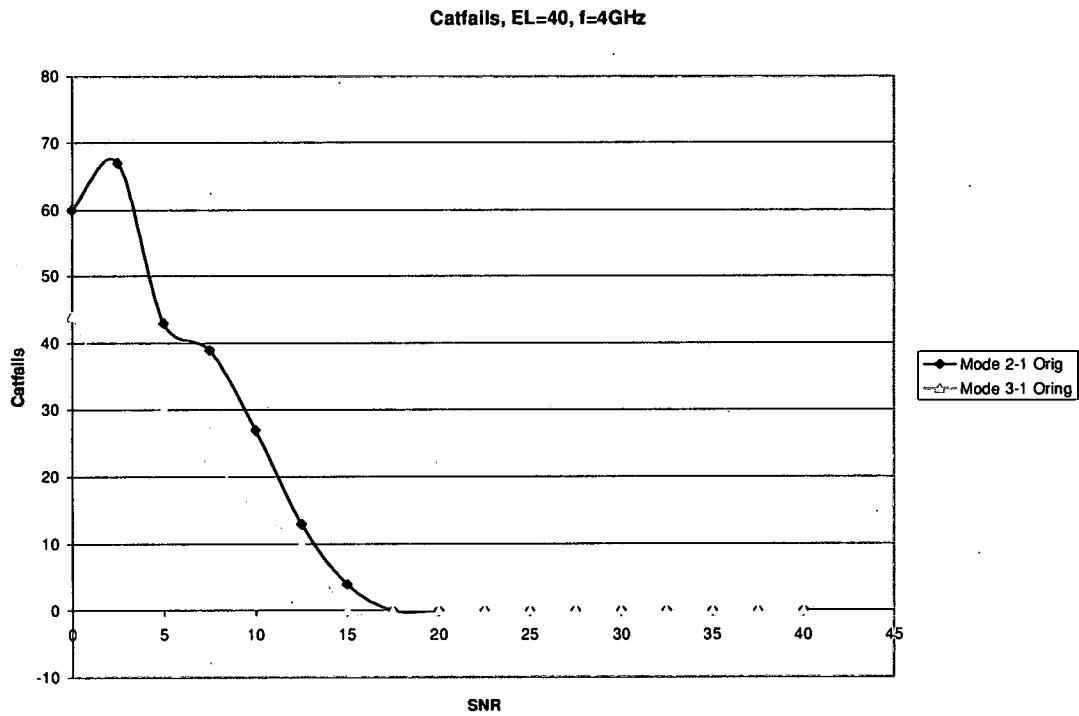


Figure 4.28: SNR vs. # of catastrophic failures for $\theta = 40^\circ$, spiral # 1, at 4GHz.

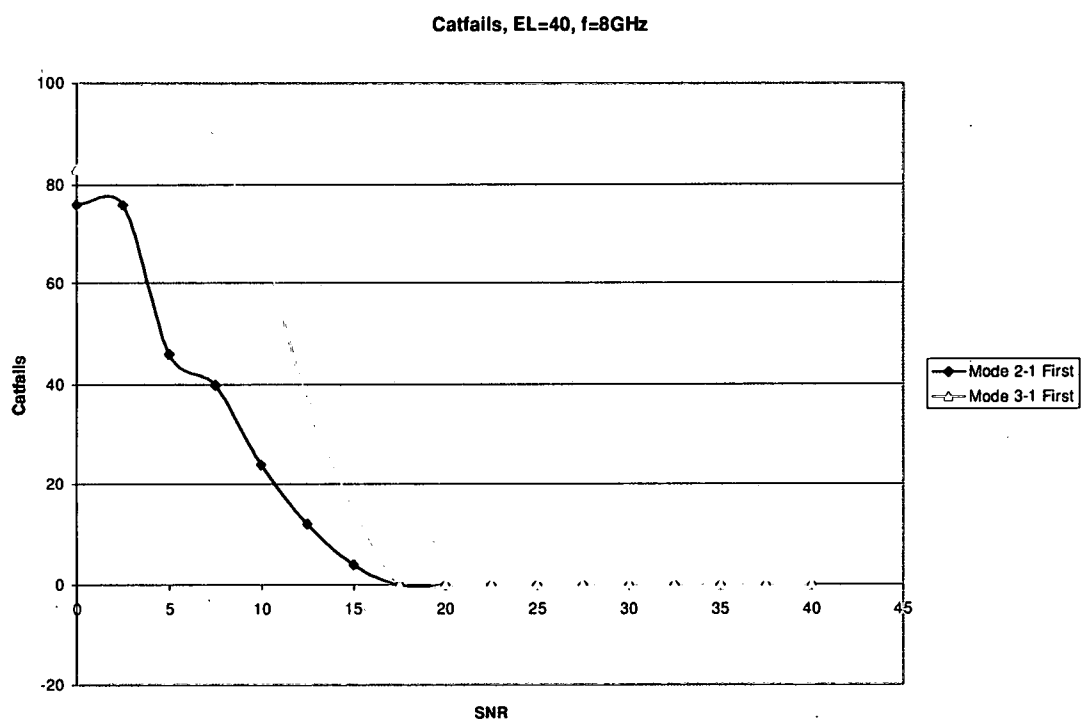


Figure 4.29: SNR vs. # of catastrophic failures for $\theta = 40^\circ$, spiral # 1, at 8GHz.

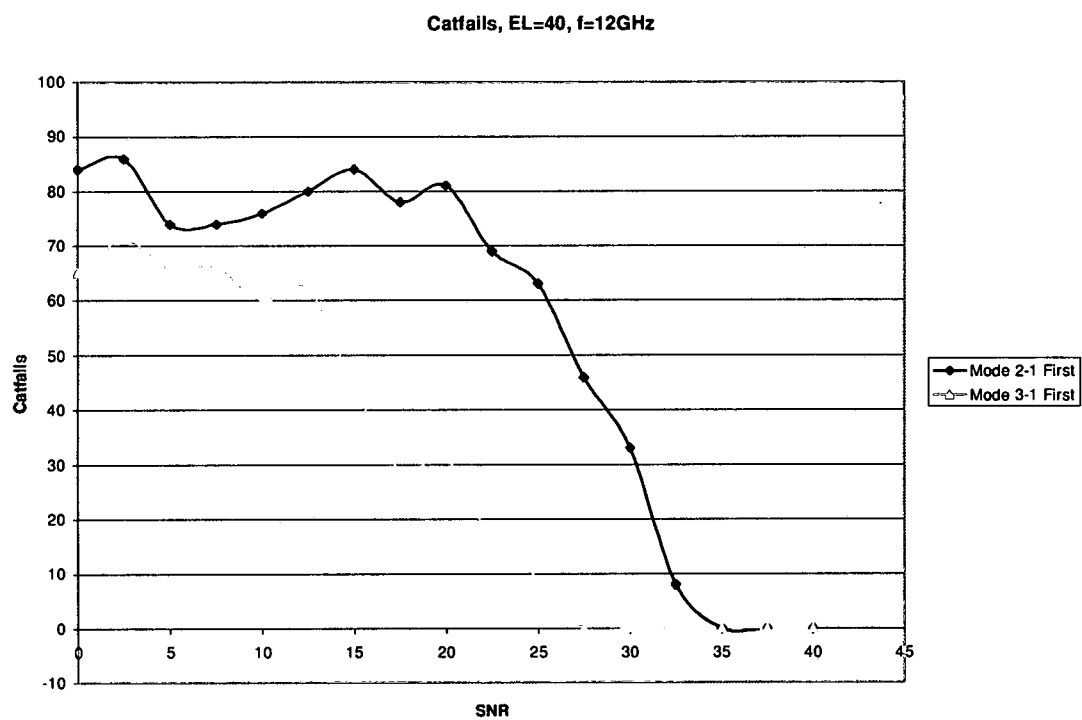


Figure 4.30: SNR vs. # of catastrophic failures for $\theta = 40^\circ$, spiral # 1, at 12GHz.

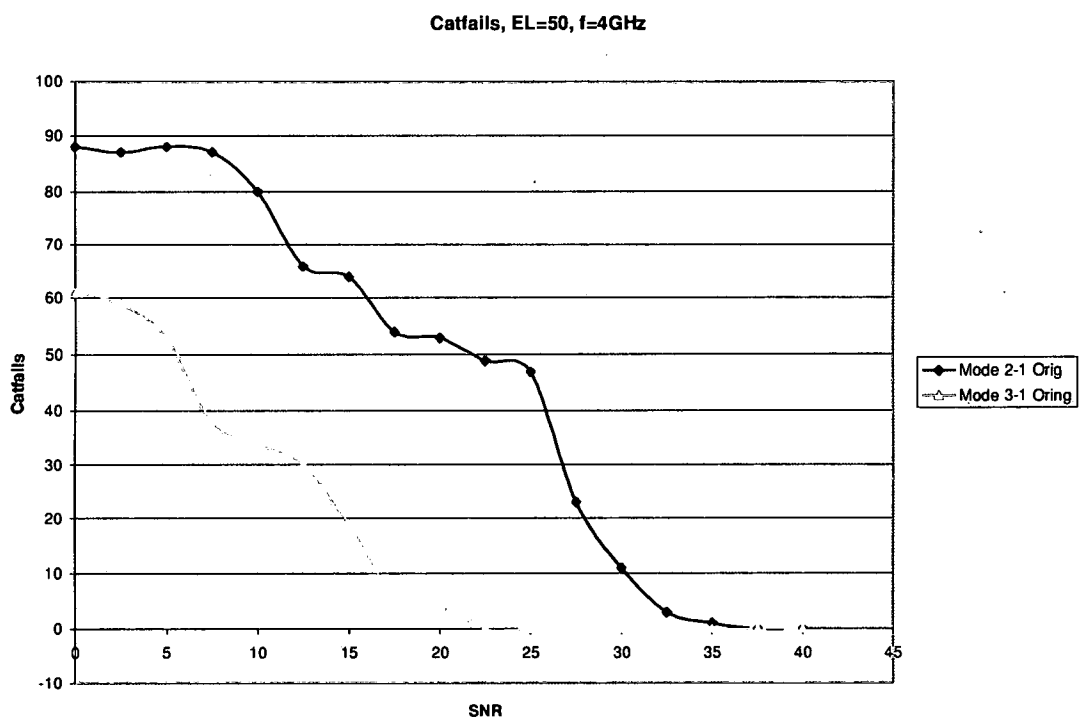


Figure 4.31: SNR vs. # of catastrophic failures for $\theta = 50^\circ$, spiral # 1, at 4GHz.

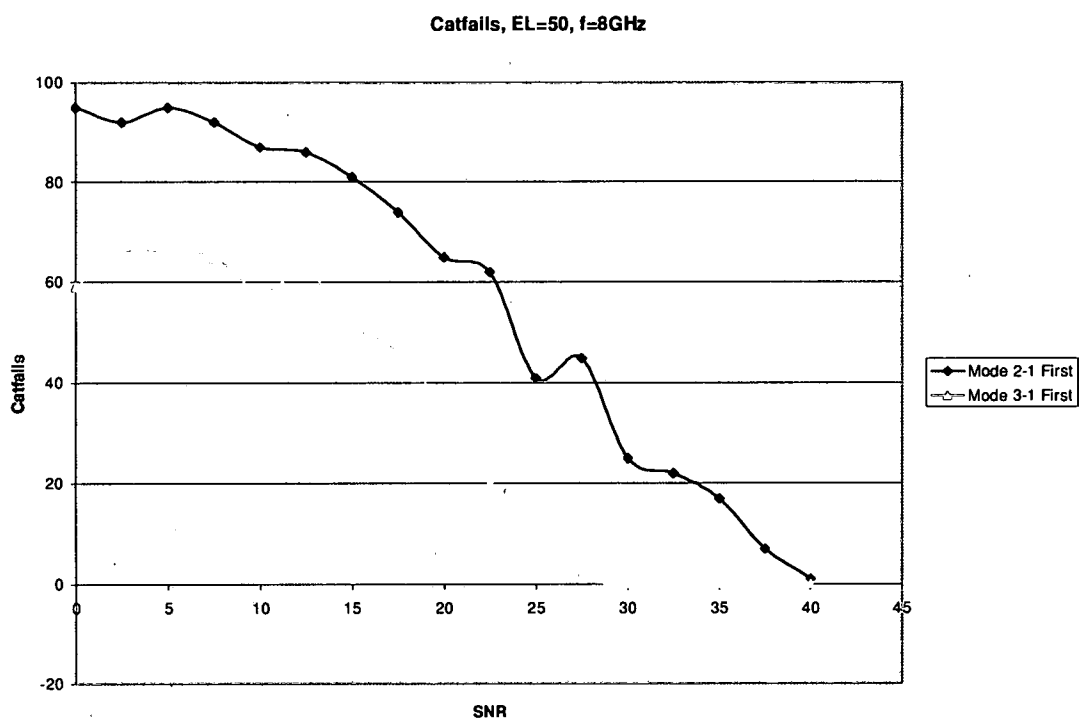


Figure 4.32: SNR vs. # of catastrophic failures for $\theta = 50^\circ$, spiral # 1, at 8GHz.

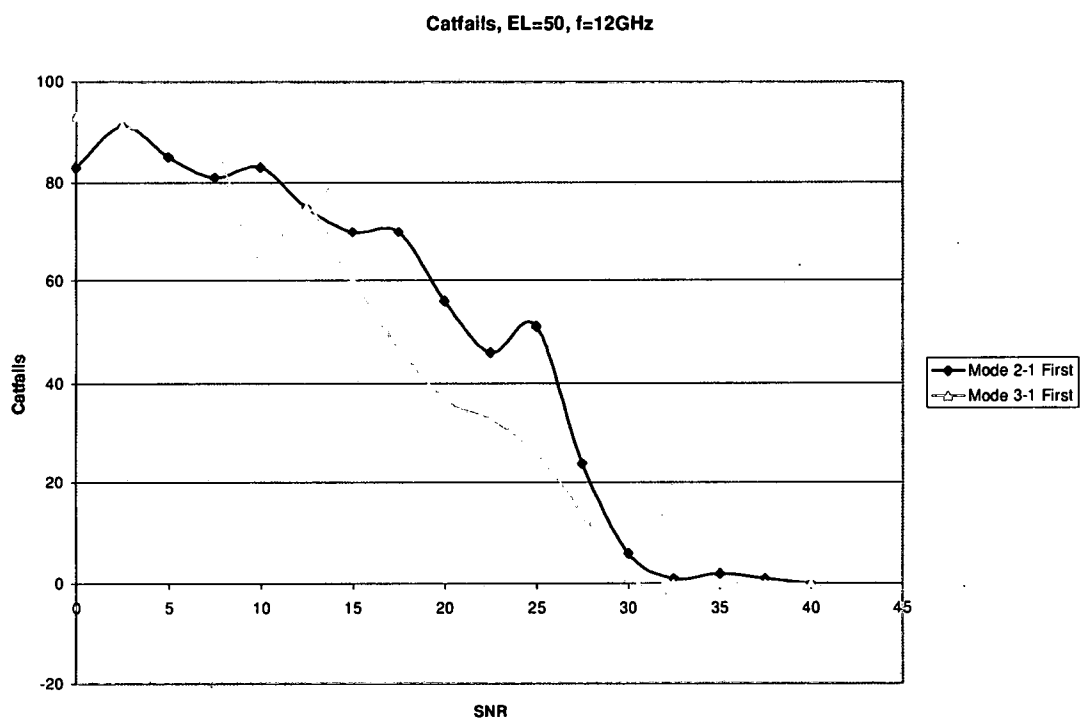


Figure 4.33: SNR vs. # of catastrophic failures for $\theta = 50^\circ$, spiral # 1, at 12GHz.

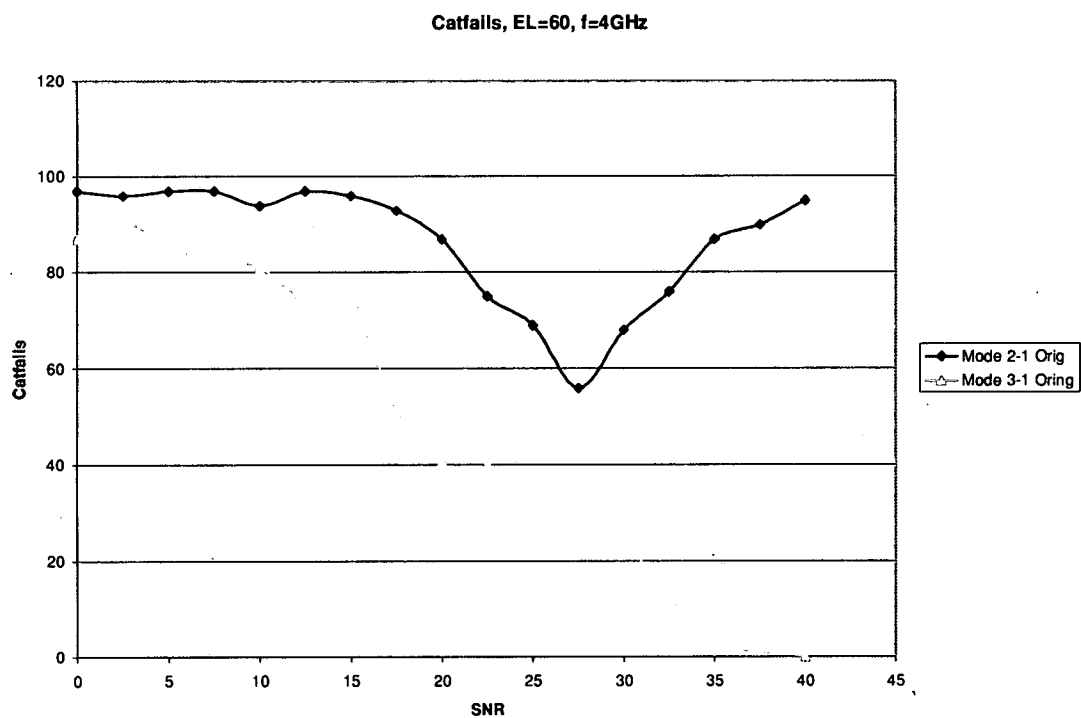


Figure 4.34: SNR vs. # of catastrophic failures for $\theta = 60^\circ$, spiral # 1, at 4GHz.

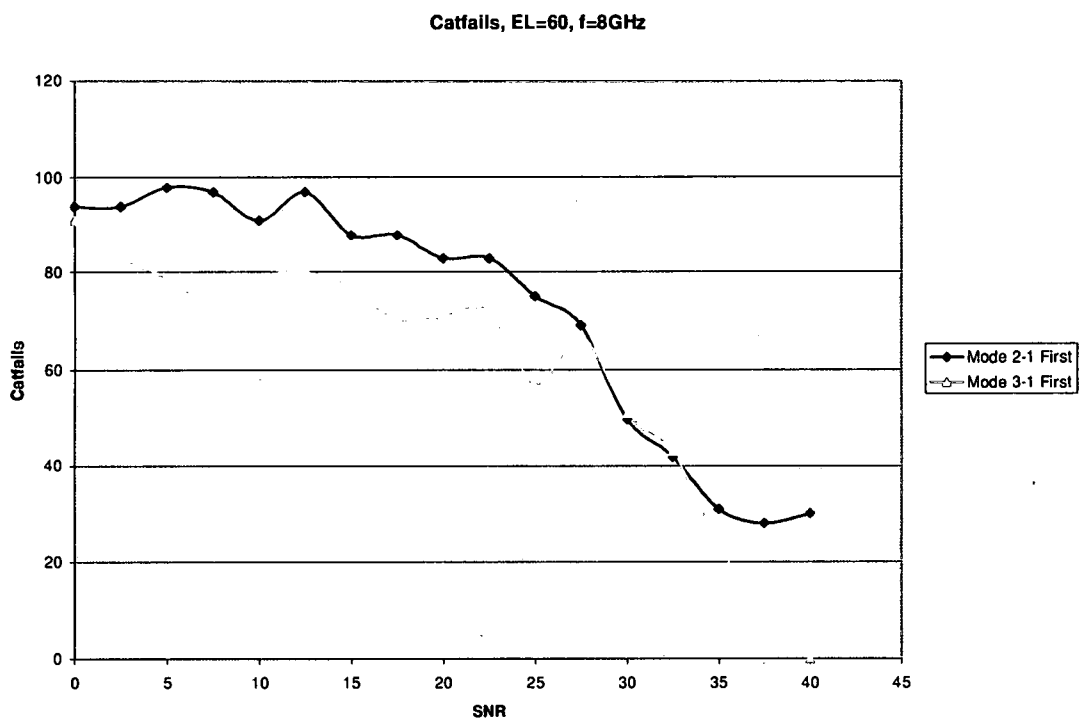


Figure 4.35: SNR vs. # of catastrophic failures for $\theta = 60^\circ$, spiral # 1, at 8GHz.

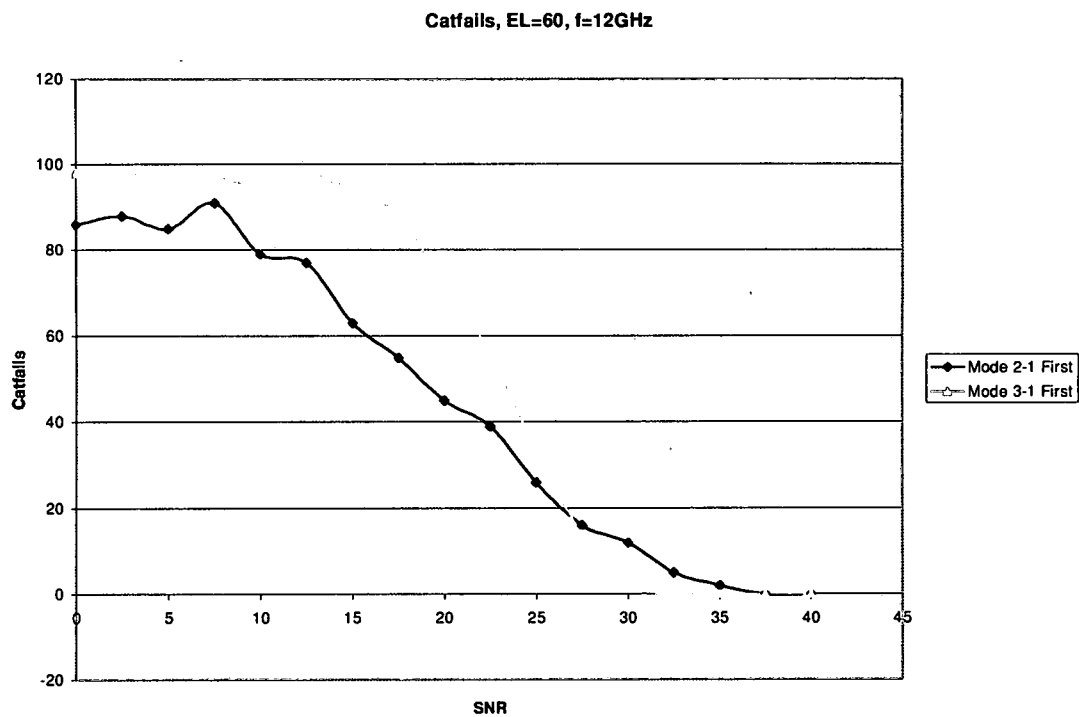


Figure 4.36: SNR vs. # of catastrophic failures for $\theta = 60^\circ$, spiral # 1, at 12GHz.

From an examination of the experimental catastrophic failure results presented in figures 4.122-4.36 for the main elevation pattern coverage area, the following observations can be made:

- As frequency increases within each specific elevation angle investigated, the number of catastrophic failures increases.
- In general, the mode 2-1 ratio is more accurate (has less catastrophic failures) in the mode 2 elevation coverage range ($\theta = 20^\circ$ - 40°) while the mode 3-1 ratio is more accurate (has less catastrophic failures) in the mode 3 elevation coverage range ($\theta = 40^\circ$ - 60°).
- As the elevation angle under investigation increases from $\theta = 20^\circ$ (figures 4.22-4.24) to $\theta = 60^\circ$ (figures 4.34-4.36), the SNR threshold value increases (the SNR value where the number of catastrophic failures from that SNR value and up are less than 50).

In the following figures, the standard deviation experimental results are presented versus SNR for spiral #1. Just as the previous figures showed how the catastrophic failures were affected as SNR was changed, figures 4.37-4.51 show how standard deviation is affected as SNR is changed. The main coverage section of the elevation modal patterns, $\theta = 20^\circ$ - 60° , is used in this analysis in 10° intervals each at the three different frequencies.

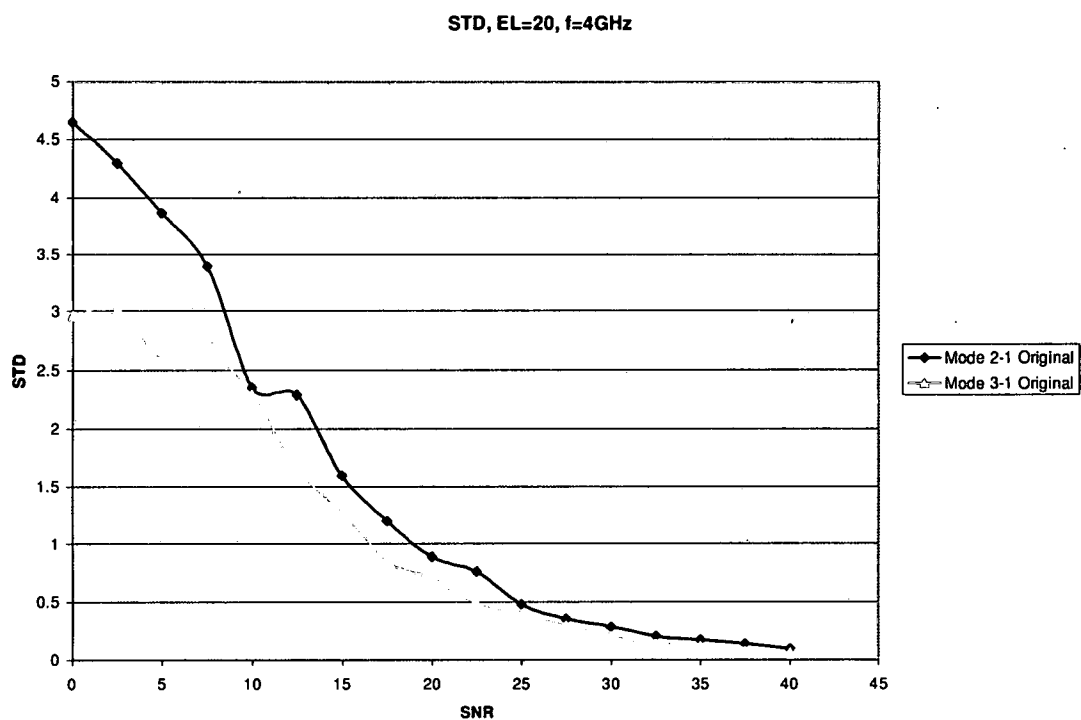


Figure 4.37: SNR vs. standard deviation for $\theta = 20^\circ$, spiral # 1, at 4GHz.

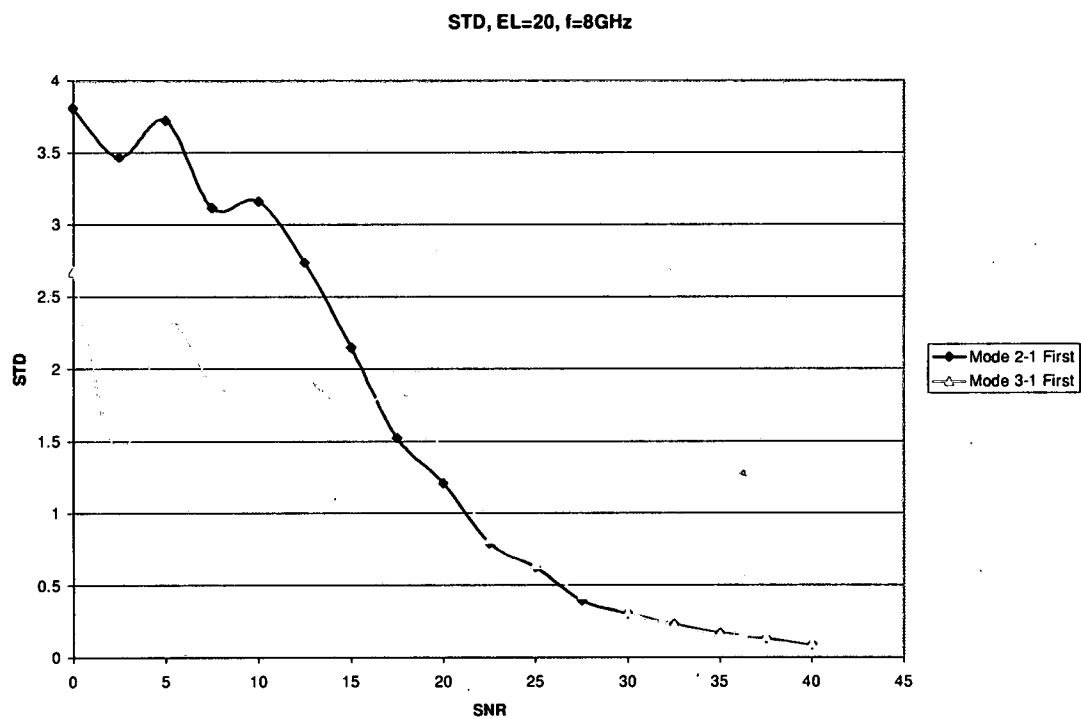


Figure 4.38: SNR vs. standard deviation for $\theta = 20^\circ$, spiral # 1, at 8GHz.

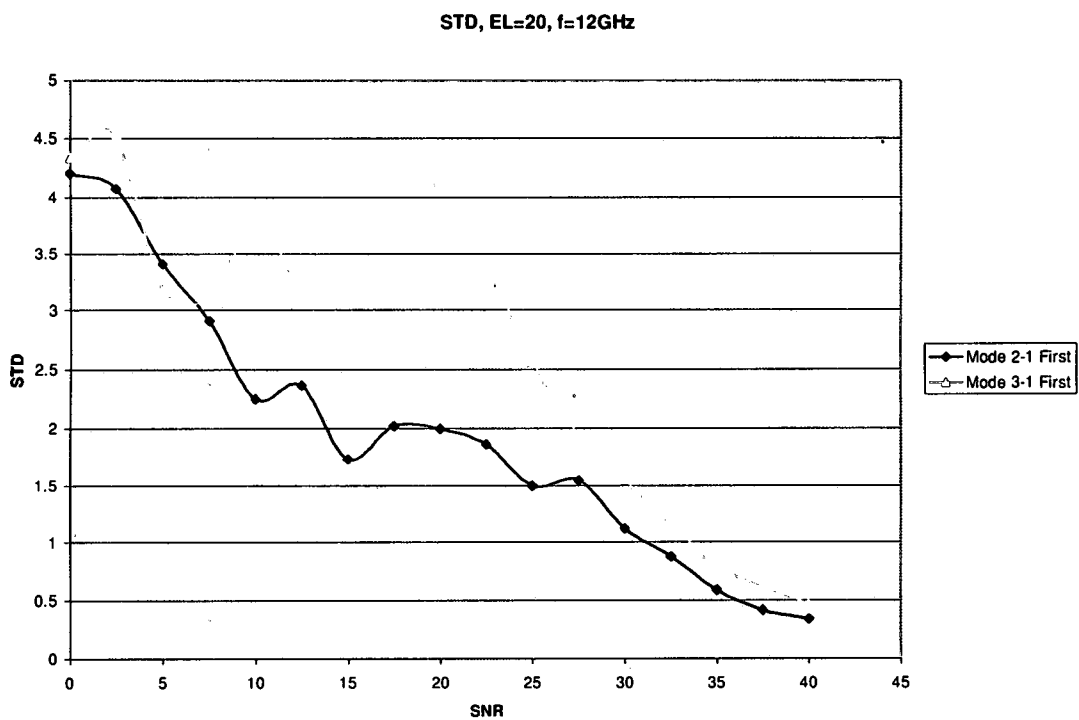


Figure 4.39: SNR vs. standard deviation for $\theta = 20^\circ$, spiral # 1, at 12GHz.

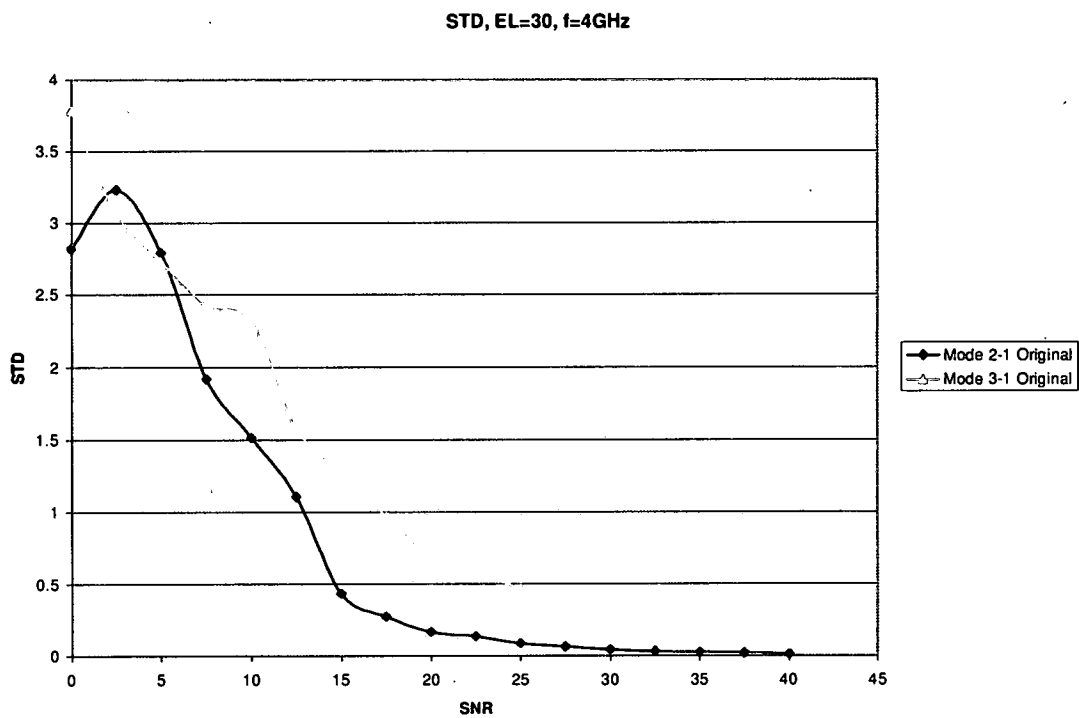


Figure 4.40: SNR vs. standard deviation for $\theta = 30^\circ$, spiral # 1, at 4GHz.

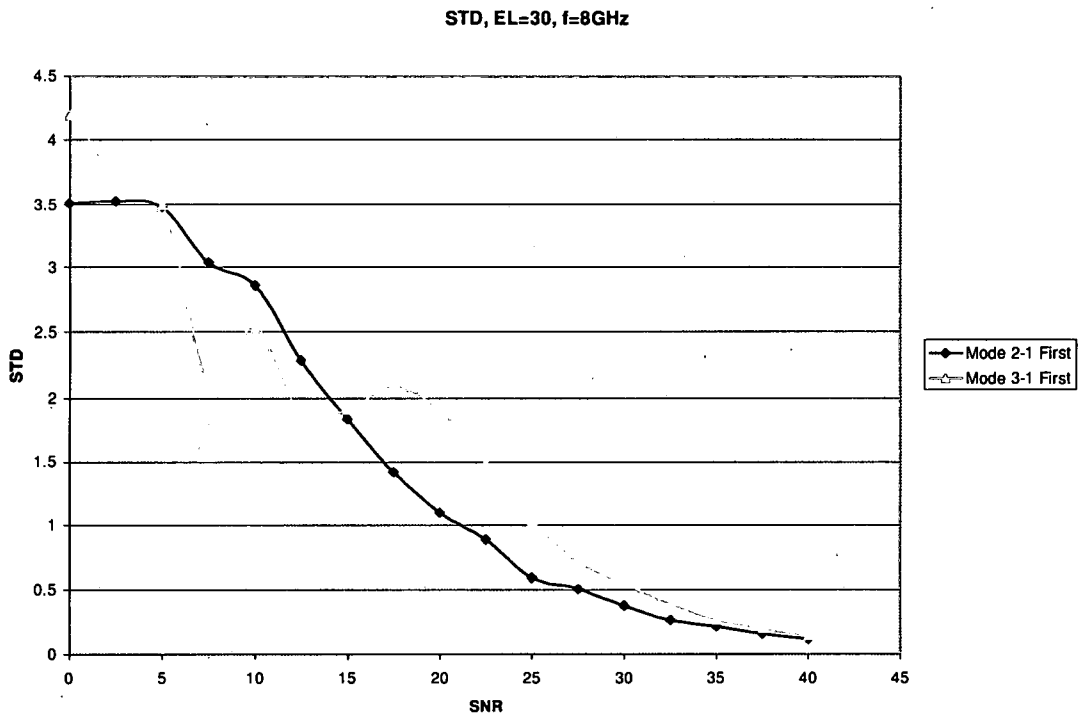


Figure 4.41: SNR vs. standard deviation for $\theta = 30^\circ$, spiral # 1, at 8GHz.

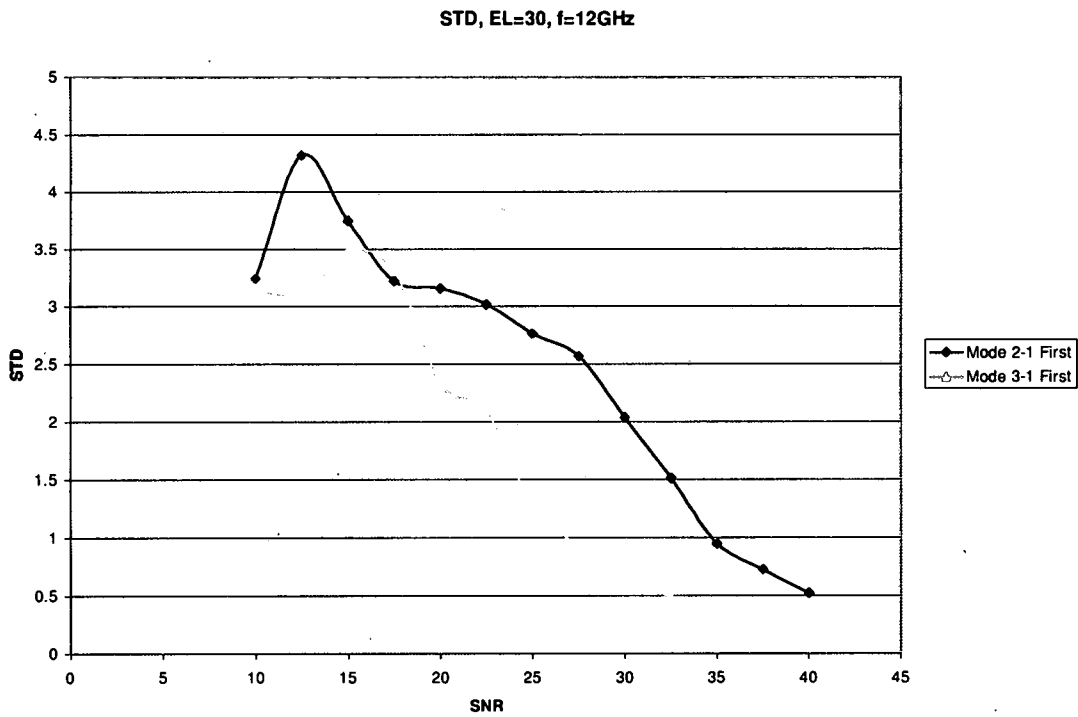


Figure 4.42: SNR vs. standard deviation for $\theta = 30^\circ$, spiral # 1, at 12GHz.

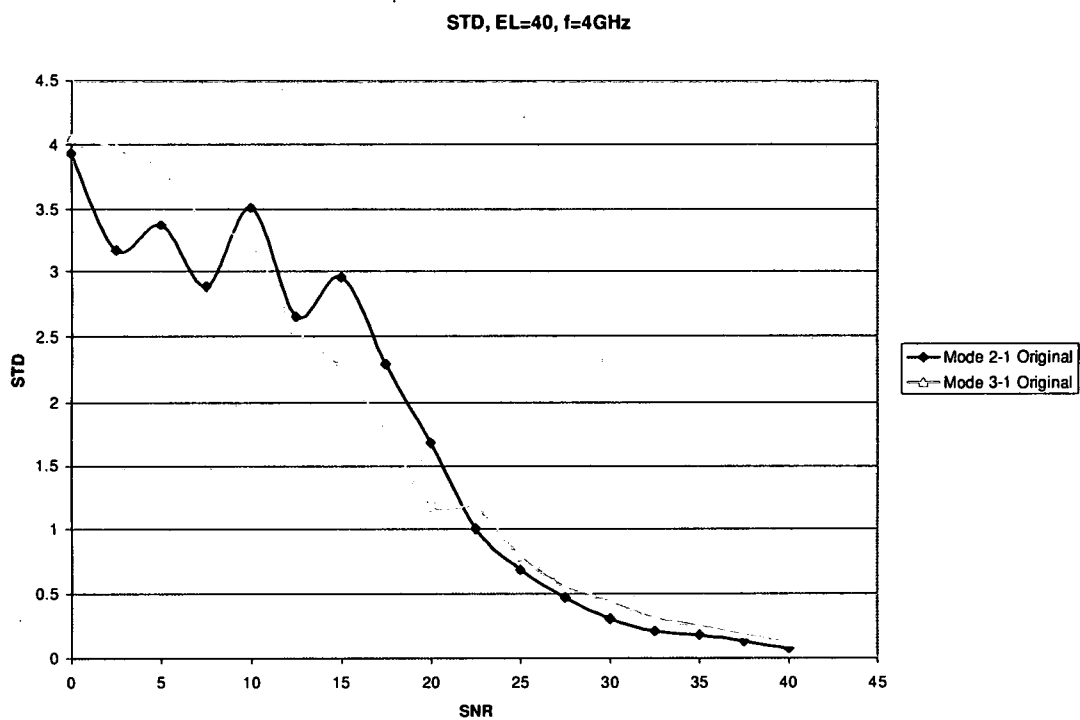


Figure 4.43: SNR vs. standard deviation for $\theta = 40^\circ$, spiral # 1, at 4GHz.

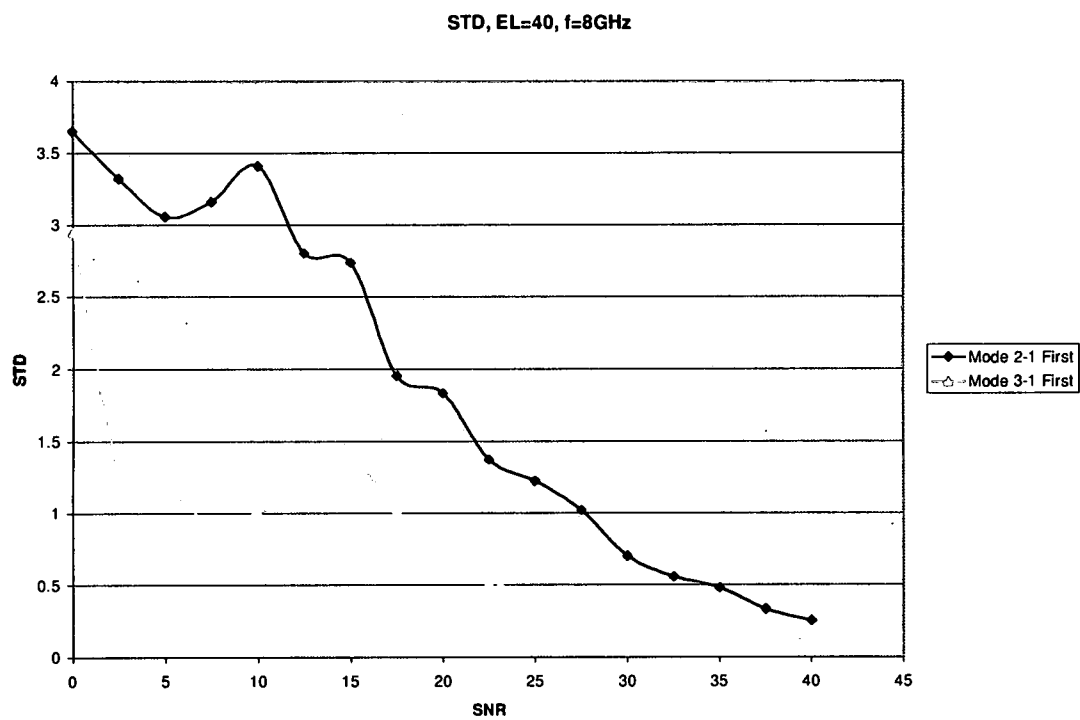


Figure 4.44: SNR vs. standard deviation for $\theta = 40^\circ$, spiral # 1, at 8GHz.

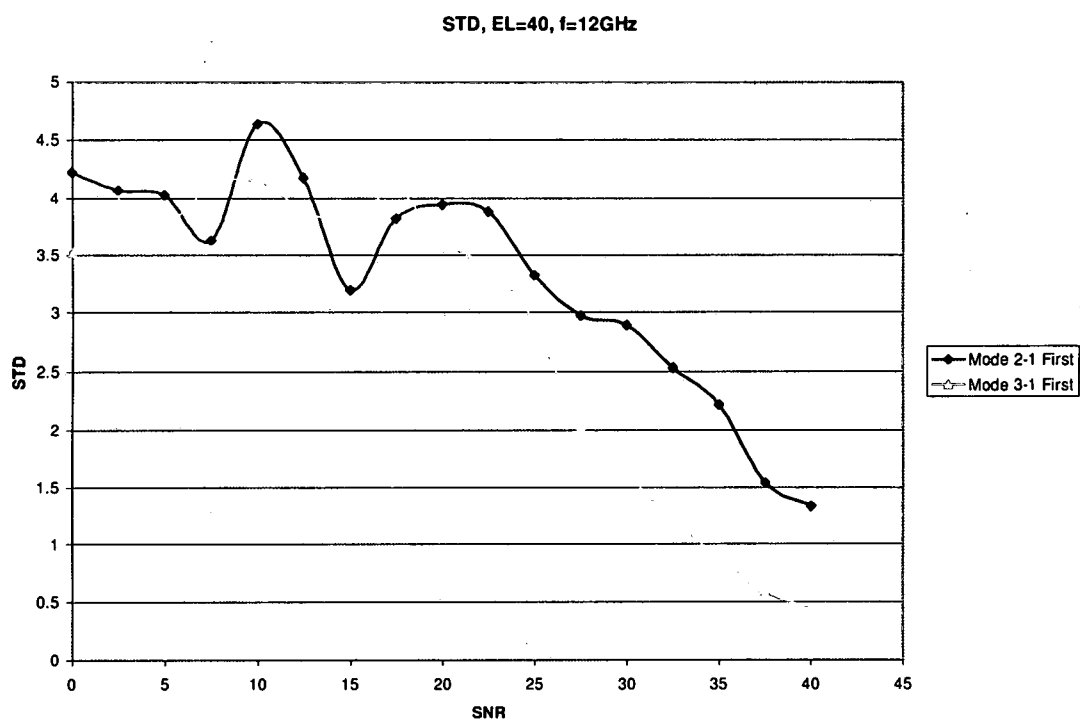


Figure 4.45: SNR vs. standard deviation for $\theta = 40^\circ$, spiral # 1, at 12GHz.

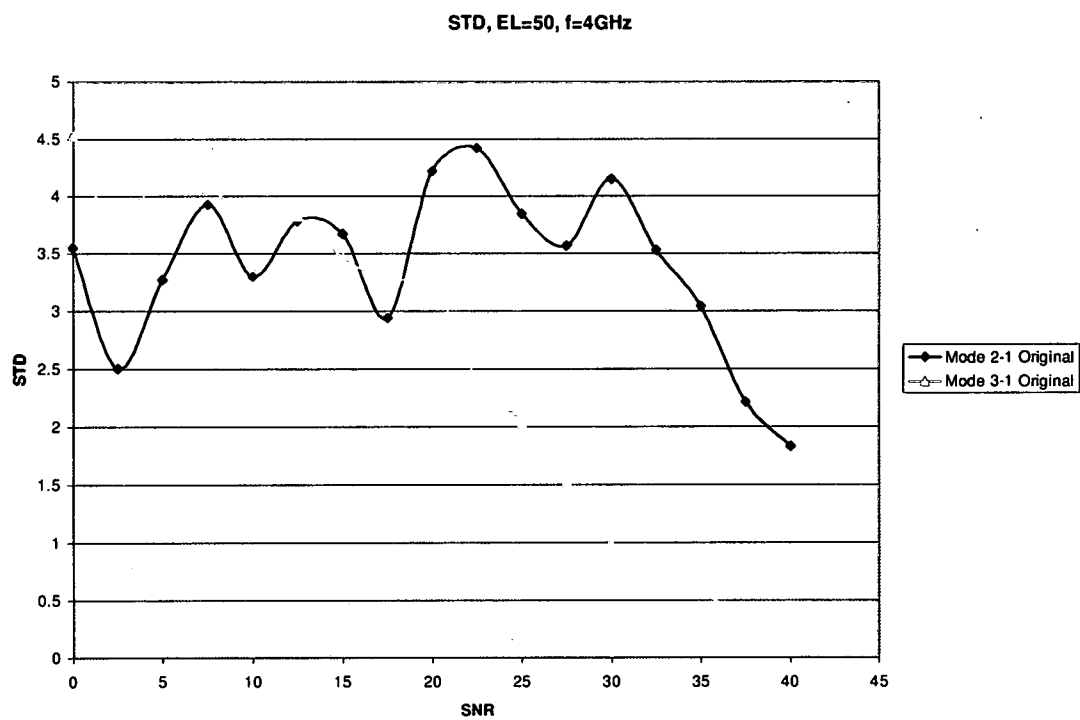


Figure 4.46: SNR vs. standard deviation for $\theta = 50^\circ$, spiral # 1, at 4GHz.

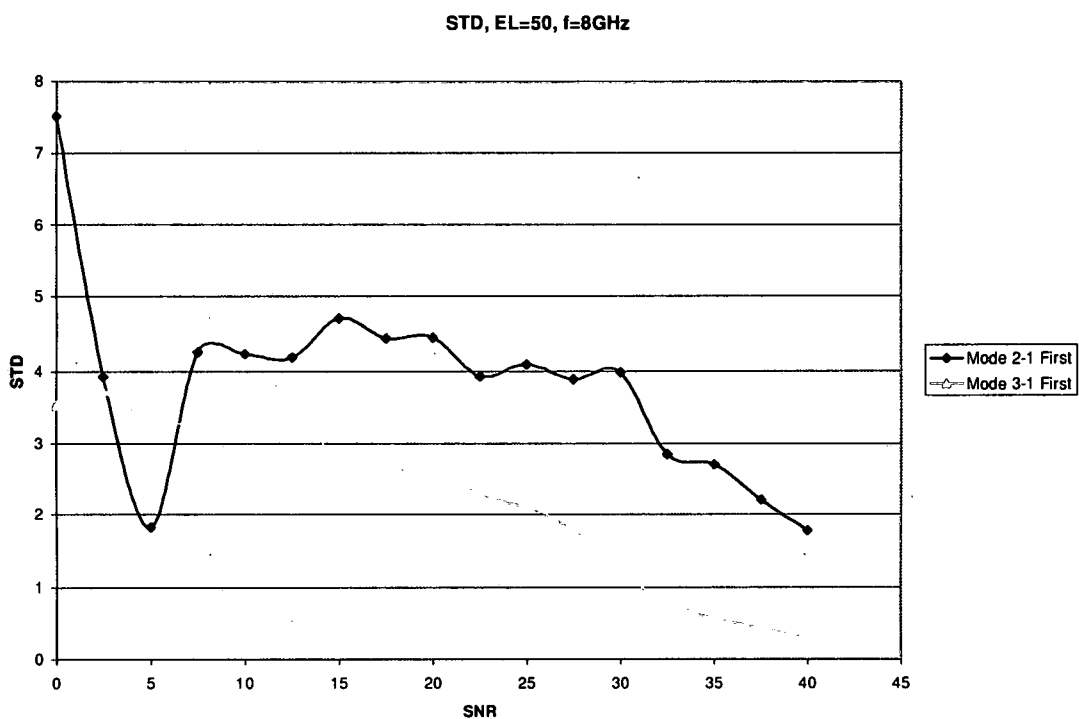


Figure 4.47: SNR vs. standard deviation for $\theta = 50^\circ$, spiral # 1, at 8GHz.

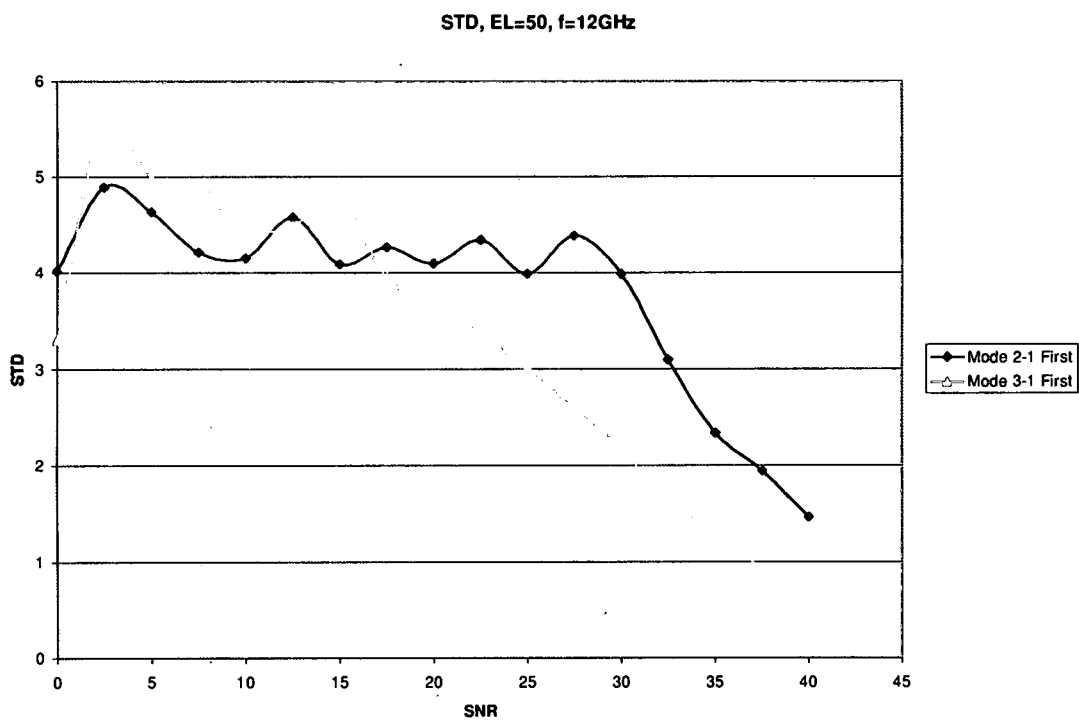


Figure 4.48: SNR vs. standard deviation for $\theta = 50^\circ$, spiral # 1, at 12GHz.

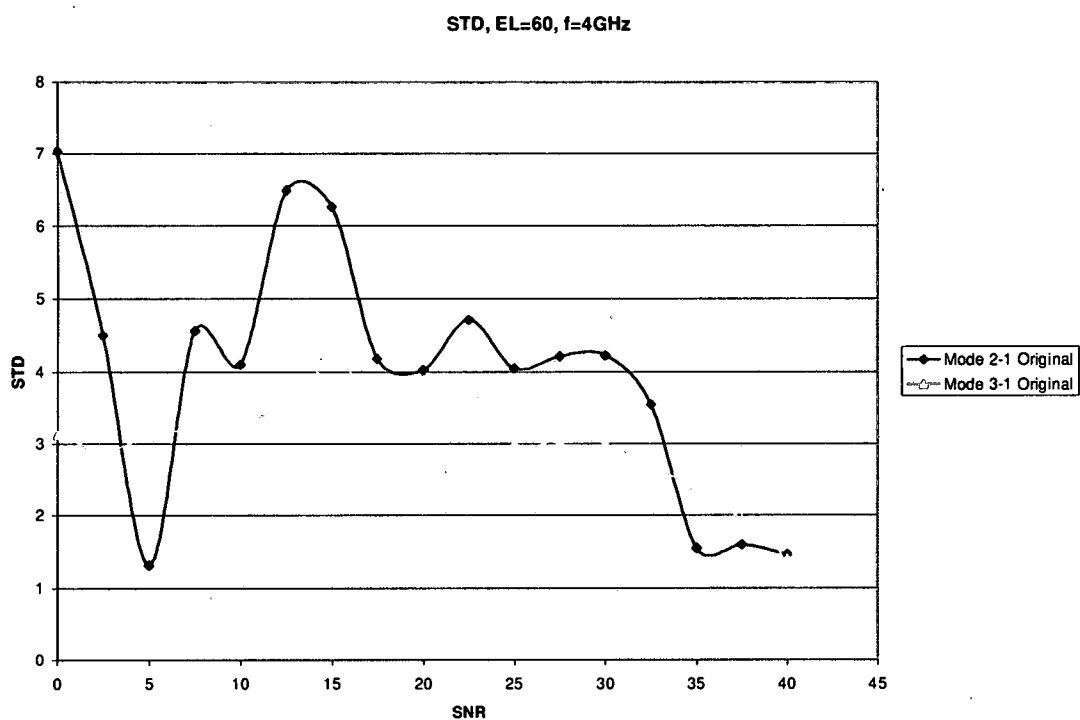


Figure 4.49: SNR vs. standard deviation for $\theta = 60^\circ$, spiral # 1, at 4GHz.

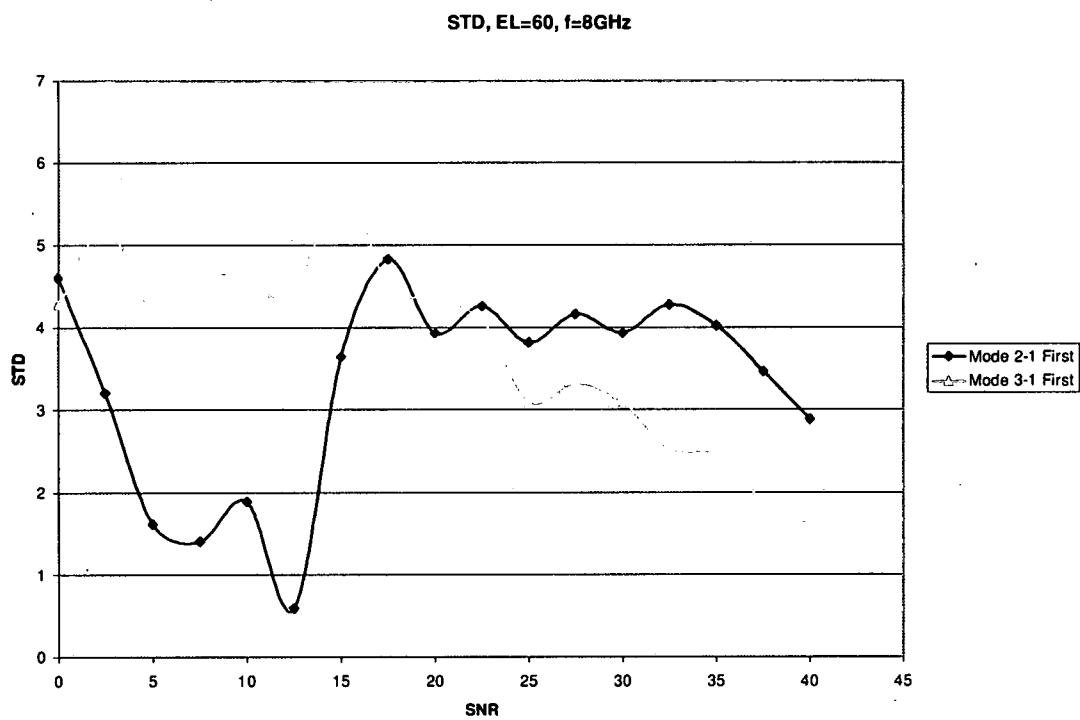


Figure 4.50: SNR vs. standard deviation for $\theta = 60^\circ$, spiral # 1, at 8GHz.

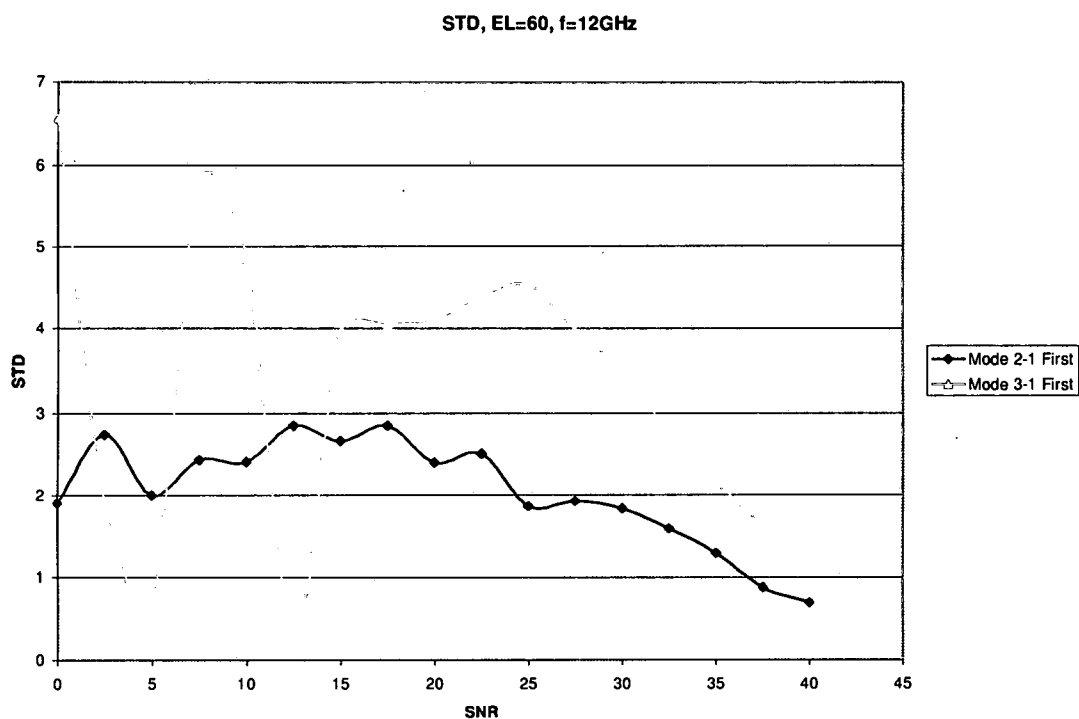


Figure 4.51: SNR vs. standard deviation for $\theta = 60^\circ$, spiral # 1, at 12GHz.

From an examination of the experimental standard deviation results presented in figures 4.37-4.51 for the main elevation pattern coverage area, the following observations can be made:

- As frequency increases within each specific elevation angle investigated, the standard deviation increases.
- As the elevation angle under investigation increases from $\theta = 20^\circ$ (figures 4.37-4.39) to $\theta = 60^\circ$ (figures 4.49-4.51), the SNR threshold value increases (the SNR value where the standard deviation from that SNR value and up are less than 2).
- As the elevation angle under investigation increases from $\theta = 20^\circ$ (figures 4.37-4.39) to $\theta = 60^\circ$ (figures 4.49-4.51), the mode 3-1 ratio contains lower standard deviation estimates than the mode 2-1 ratio and thus becomes the more accurate ratio for angle estimates as θ increases.

We have looked at the results of this Monte Carlo experiment for elevation estimates in the main elevation coverage region, $\theta = 20^\circ$ - 60° . Now we need to look into the more troublesome areas for accurate elevation angle estimation: near boresight and approaching the horizon.

Near boresight has good coverage from mode 1 as presented in chapter 2; however, looking at the elevation modal ratios of figures 3.37-3.42 it is noticeable that a null is present in the center of each ratio at boresight, or $\theta = 0^\circ$ ($\theta = 90^\circ$ in the figures), and this null becomes less distinguished as frequency increases. This may lead to estimate inconsistencies at higher frequencies near boresight. The number of catastrophic failures for $\theta = 10^\circ$, 5° , and 0° are presented below versus SNR in figures 4.52-4.60; the standard deviation of the estimates versus SNR are presented in figures 4.61-4.69.

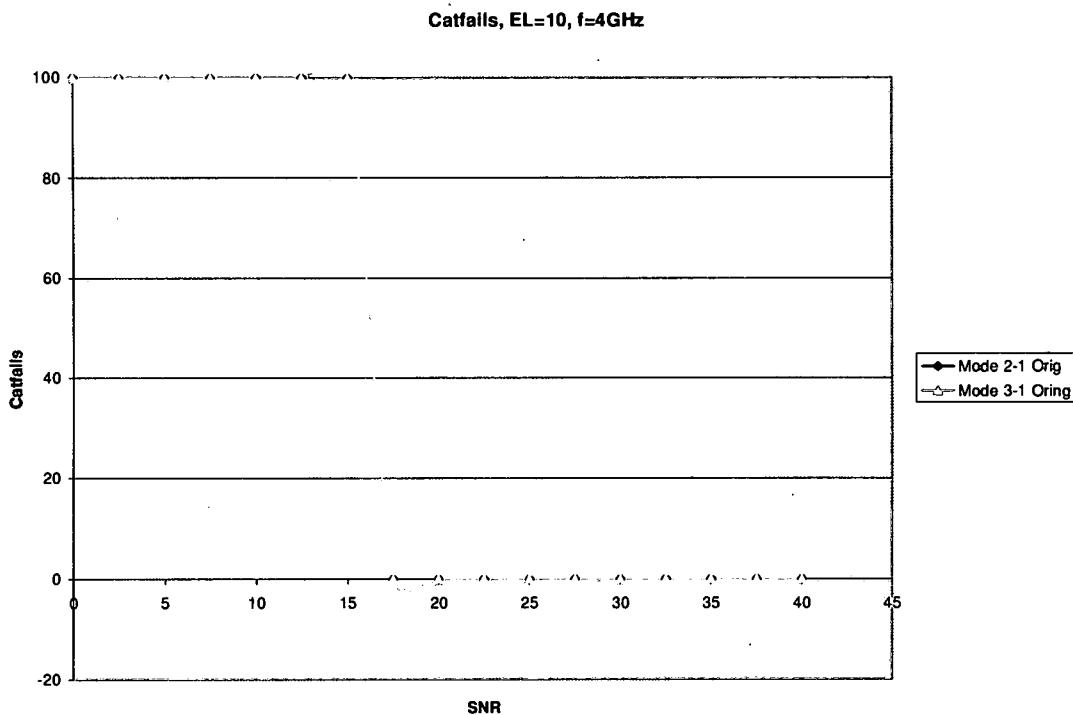


Figure 4.52: SNR vs. # of catastrophic failures for $\theta = 10^\circ$, spiral # 1, at 4GHz.

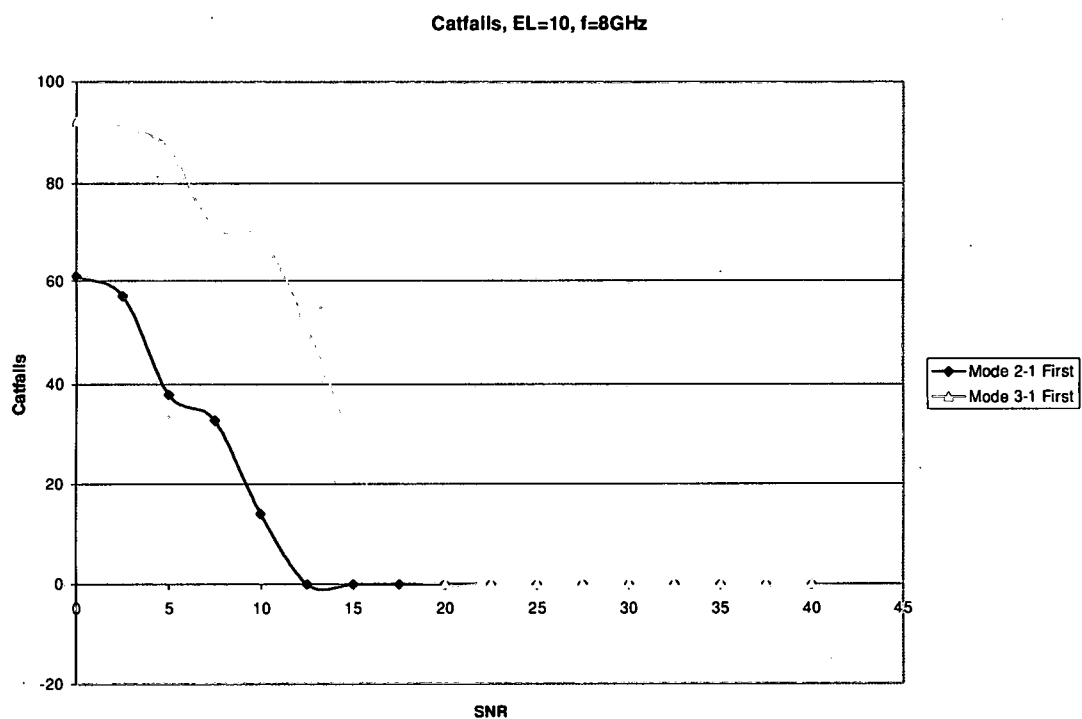


Figure 4.53: SNR vs. # of catastrophic failures for $\theta = 10^\circ$, spiral # 1, at 8GHz.

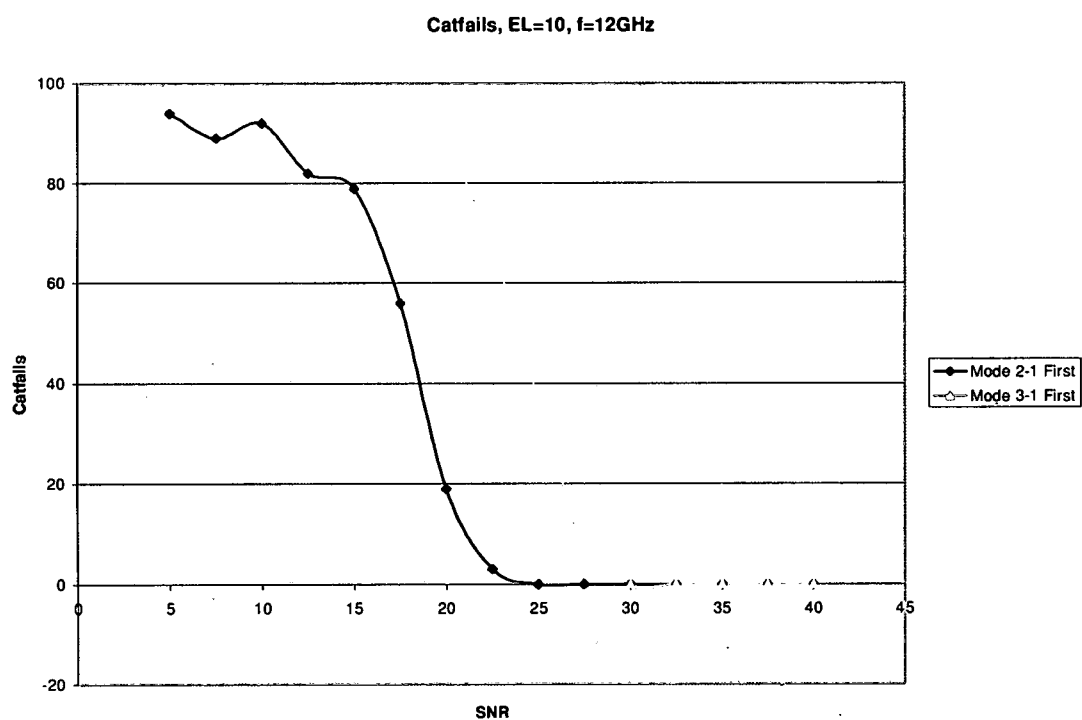


Figure 4.54: SNR vs. # of catastrophic failures for $\theta = 10^\circ$, spiral # 1, at 12GHz.

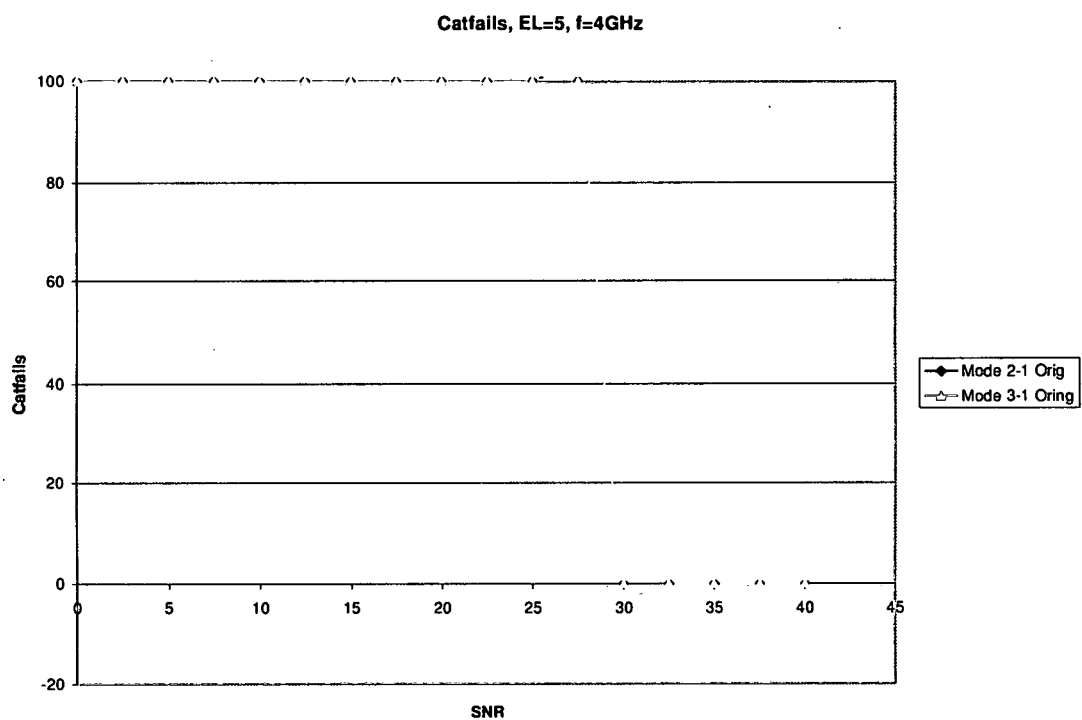


Figure 4.55: SNR vs. # of catastrophic failures for $\theta = 5^\circ$, spiral # 1, at 4GHz.

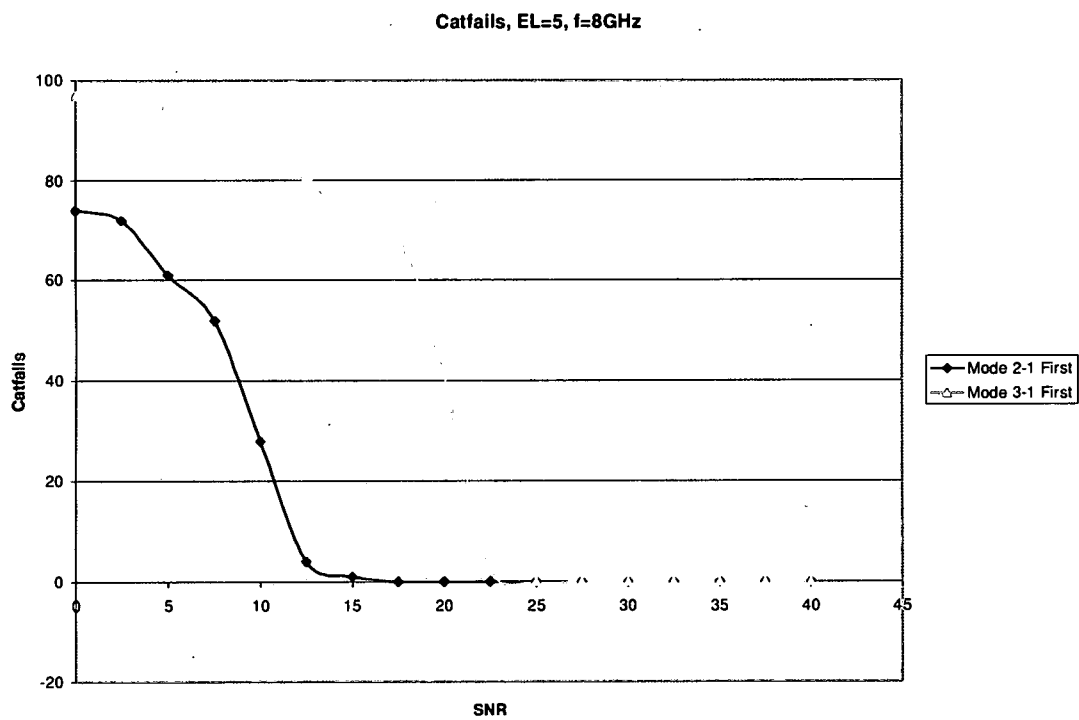


Figure 4.56: SNR vs. # of catastrophic failures for $\theta = 5^\circ$, spiral # 1, at 8GHz.

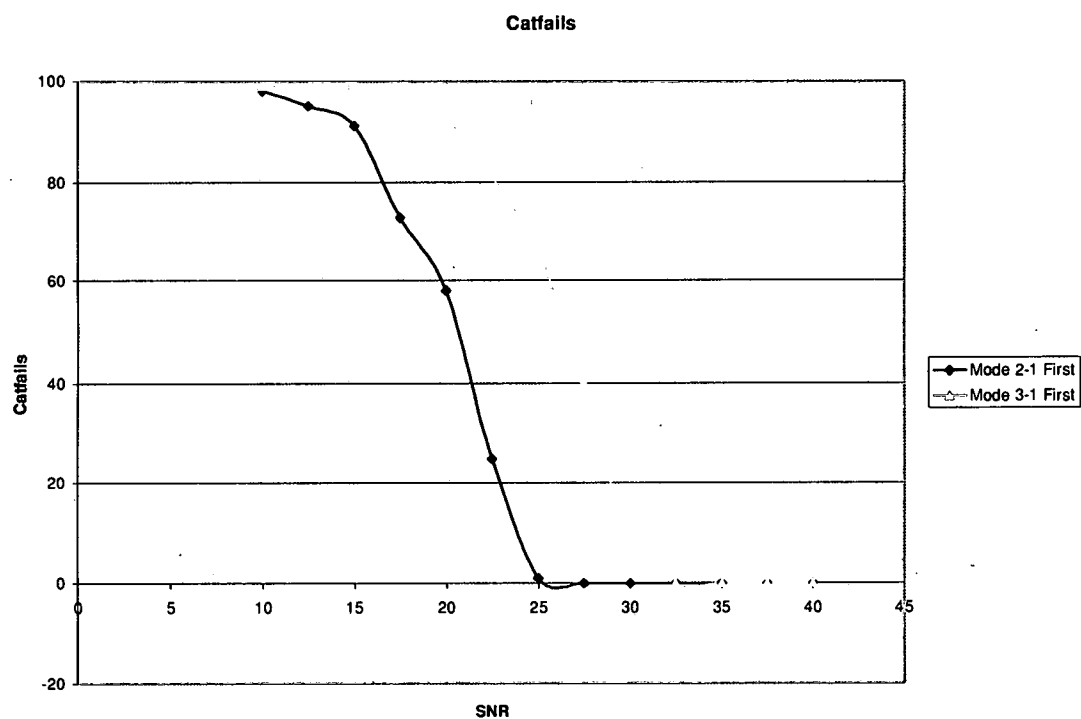


Figure 4.57: SNR vs. # of catastrophic failures for $\theta = 5^\circ$, spiral # 1, at 12GHz.

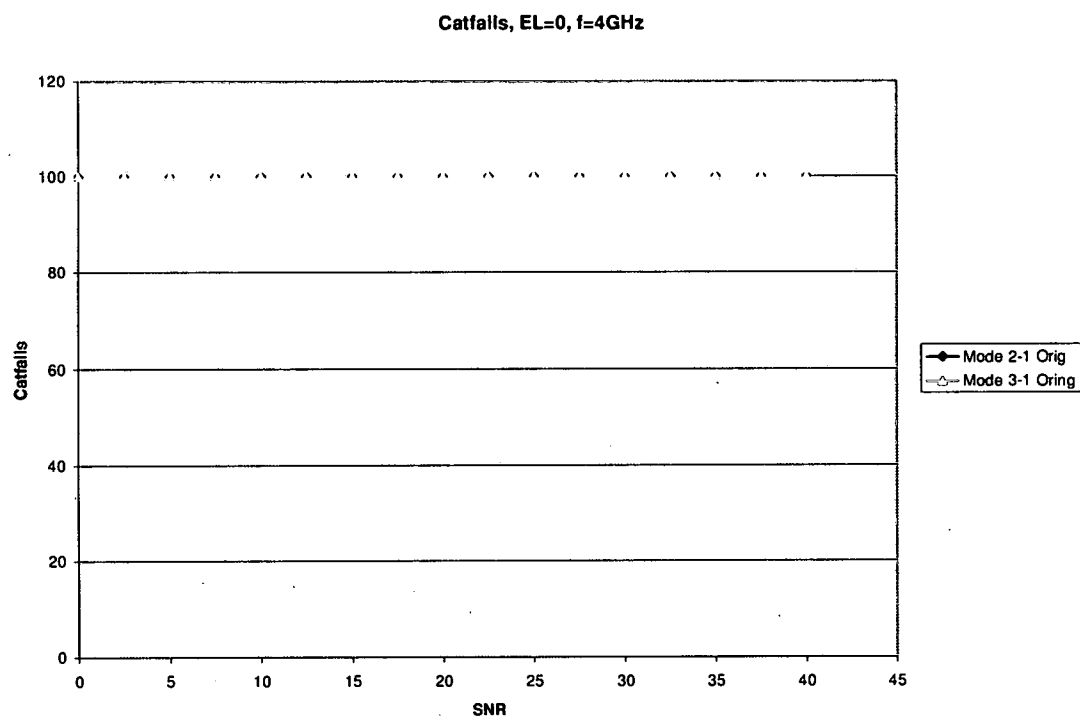


Figure 4.58: SNR vs. # of catastrophic failures for $\theta = 0^\circ$, spiral # 1, at 4GHz.

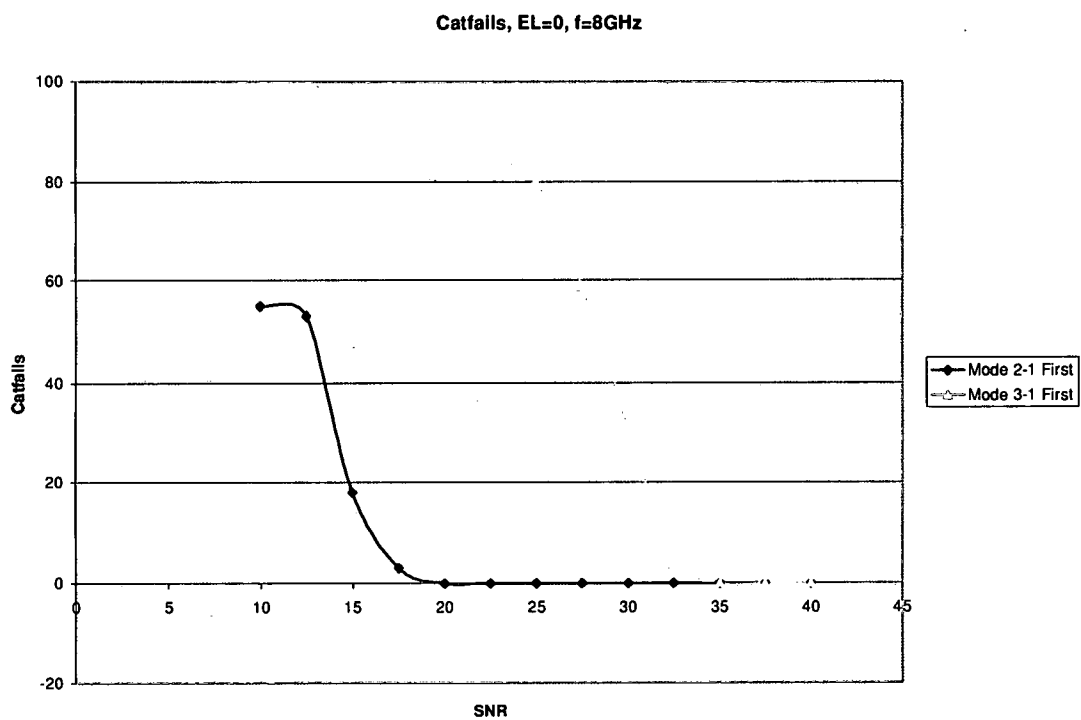


Figure 4.59: SNR vs. # of catastrophic failures for $\theta = 0^\circ$, spiral # 1, at 8GHz.

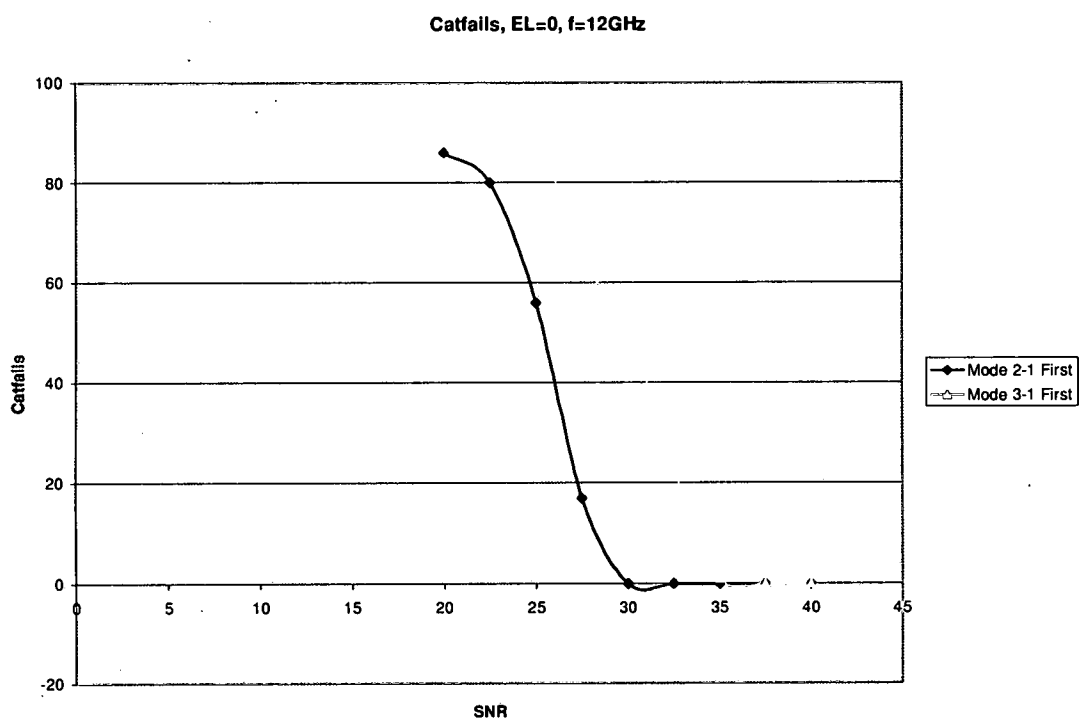


Figure 4.60: SNR vs. # of catastrophic failures for $\theta = 0^\circ$, spiral # 1, at 12GHz.

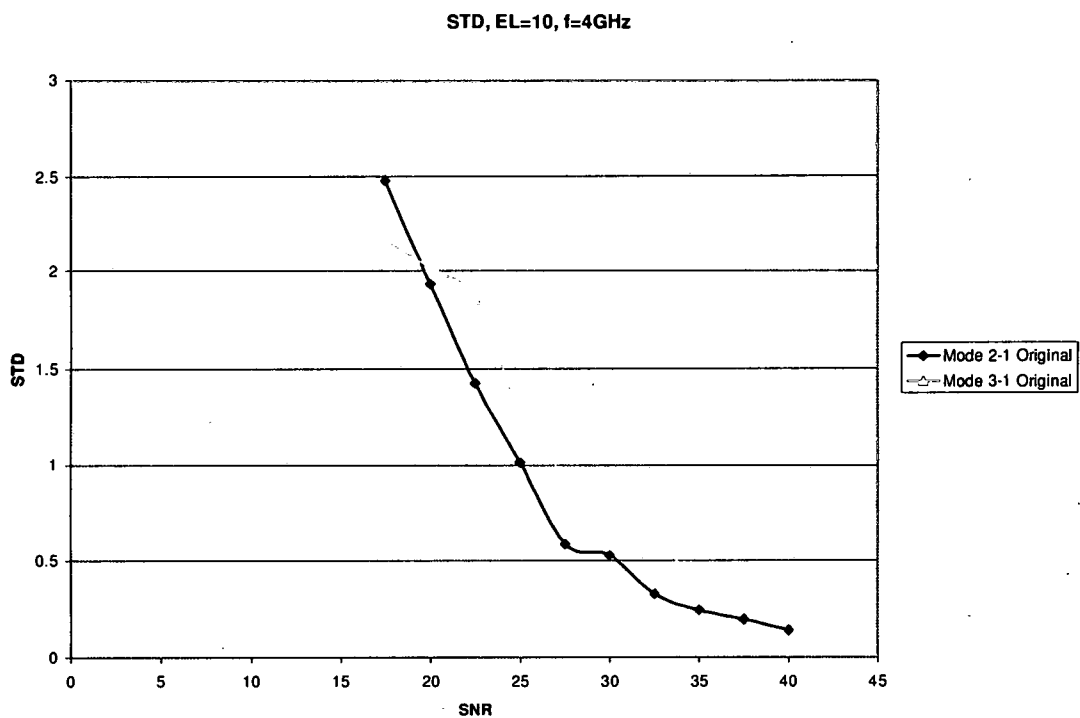


Figure 4.61: SNR vs. standard deviation for $\theta = 10^\circ$, spiral # 1, at 4GHz.

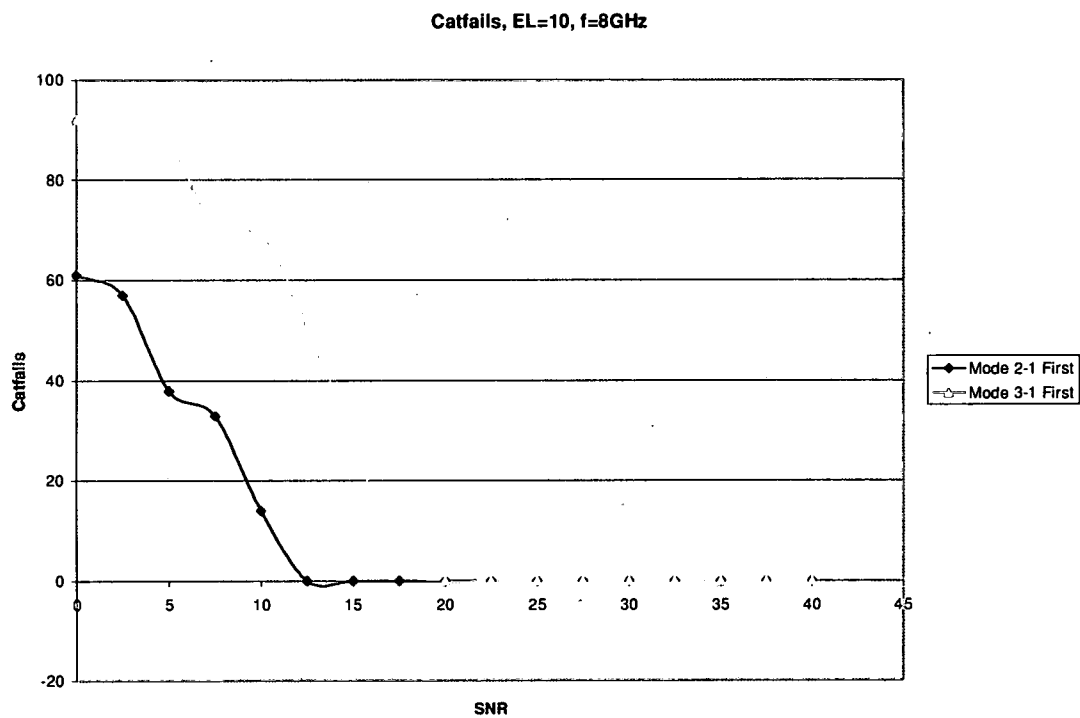


Figure 4.62: SNR vs. standard deviation for $\theta = 10^\circ$, spiral # 1, at 8GHz.

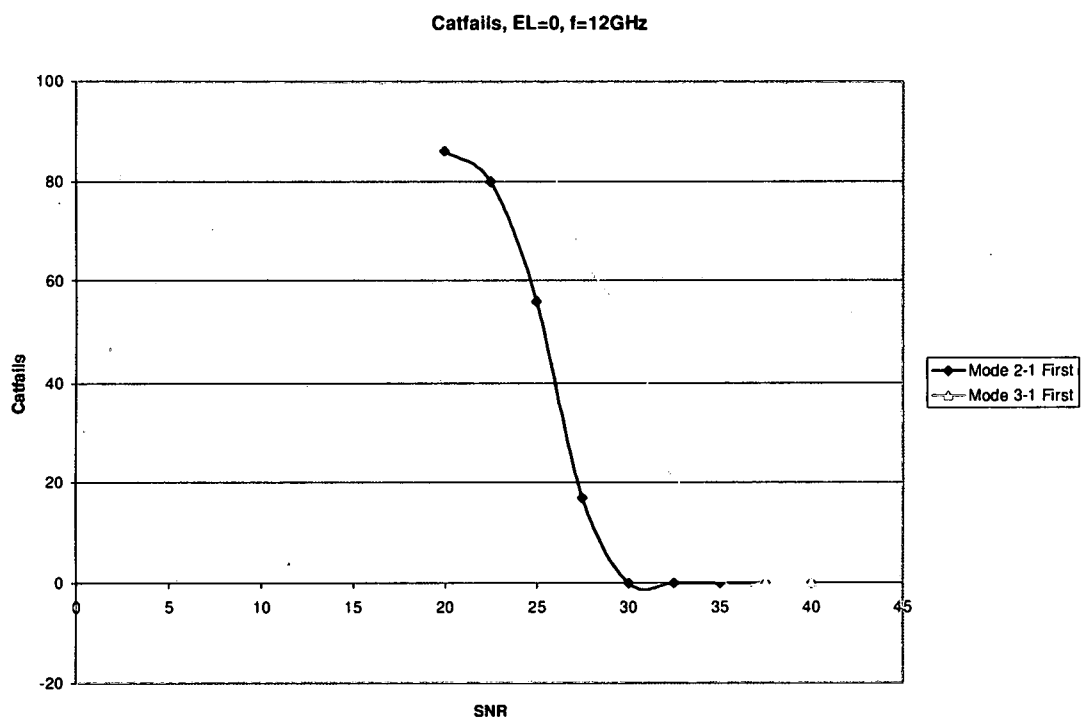


Figure 4.63: SNR vs. standard deviation for $\theta = 10^\circ$, spiral # 1, at 12GHz.

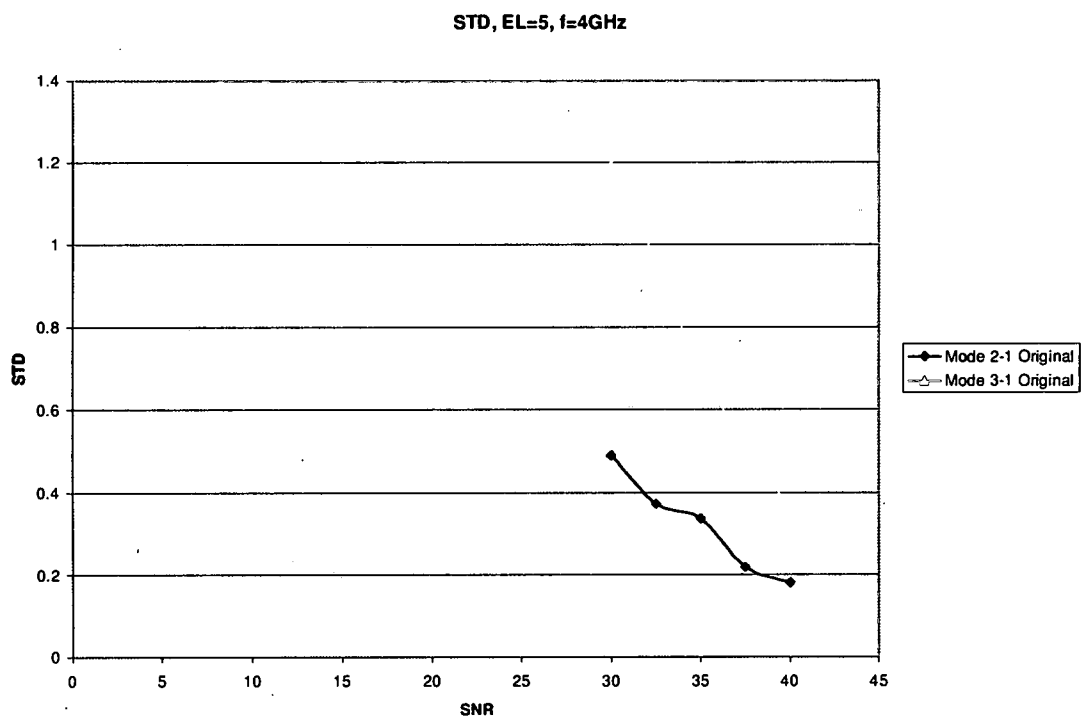


Figure 4.64: SNR vs. standard deviation for $\theta = 5^\circ$, spiral # 1, at 4GHz.

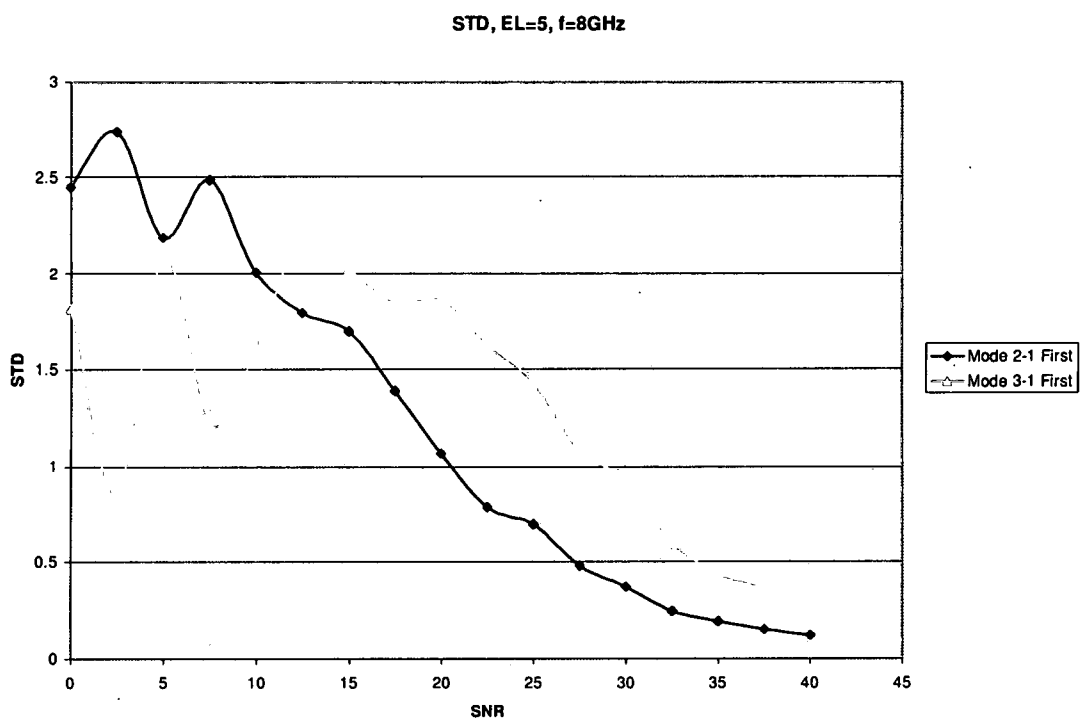


Figure 4.65: SNR vs. standard deviation for $\theta = 5^\circ$, spiral # 1, at 8GHz.

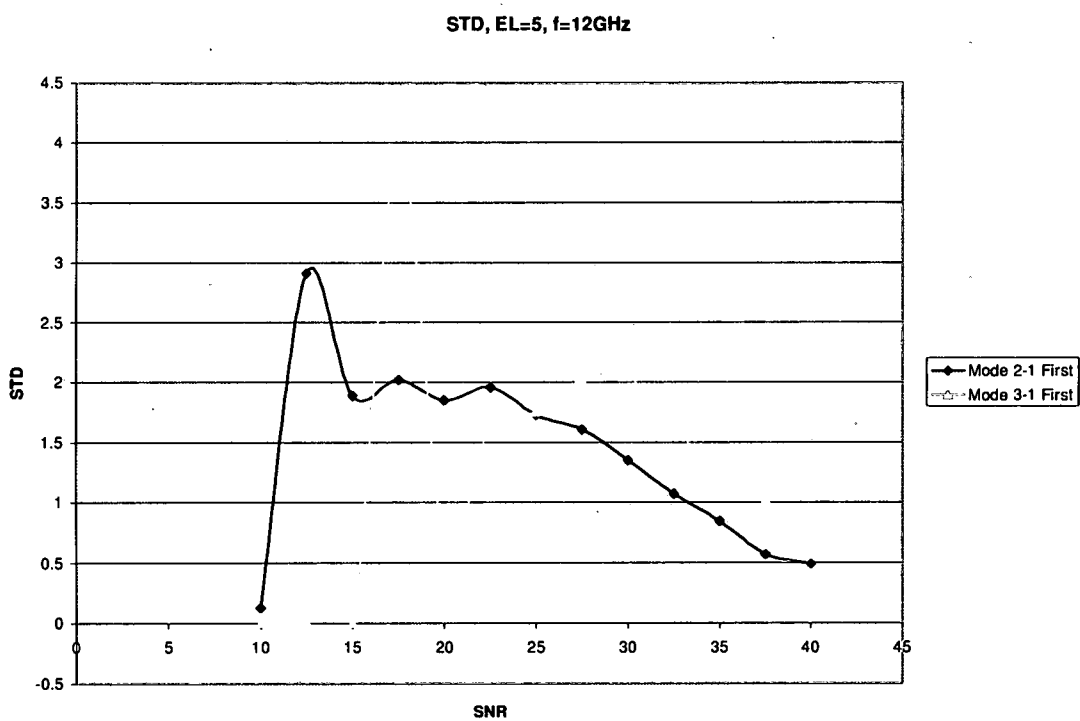


Figure 4.66: SNR vs. standard deviation for $\theta = 5^\circ$, spiral # 1, at 12GHz.

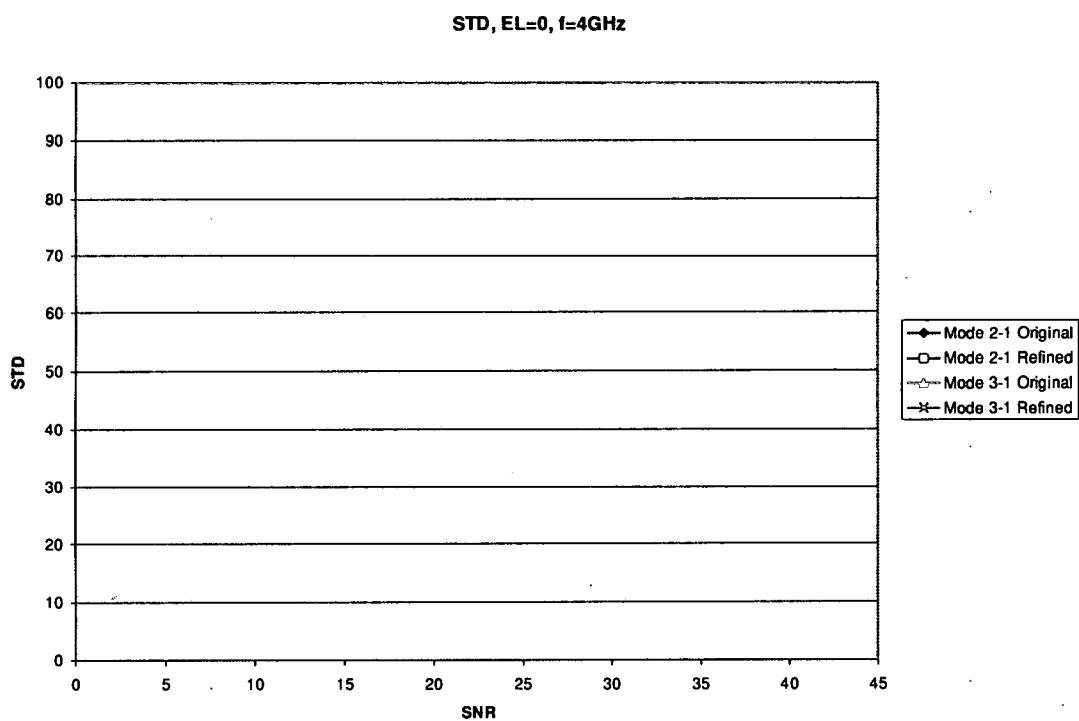


Figure 4.67: SNR vs. standard deviation for $\theta = 0^\circ$, spiral # 1, at 4GHz.

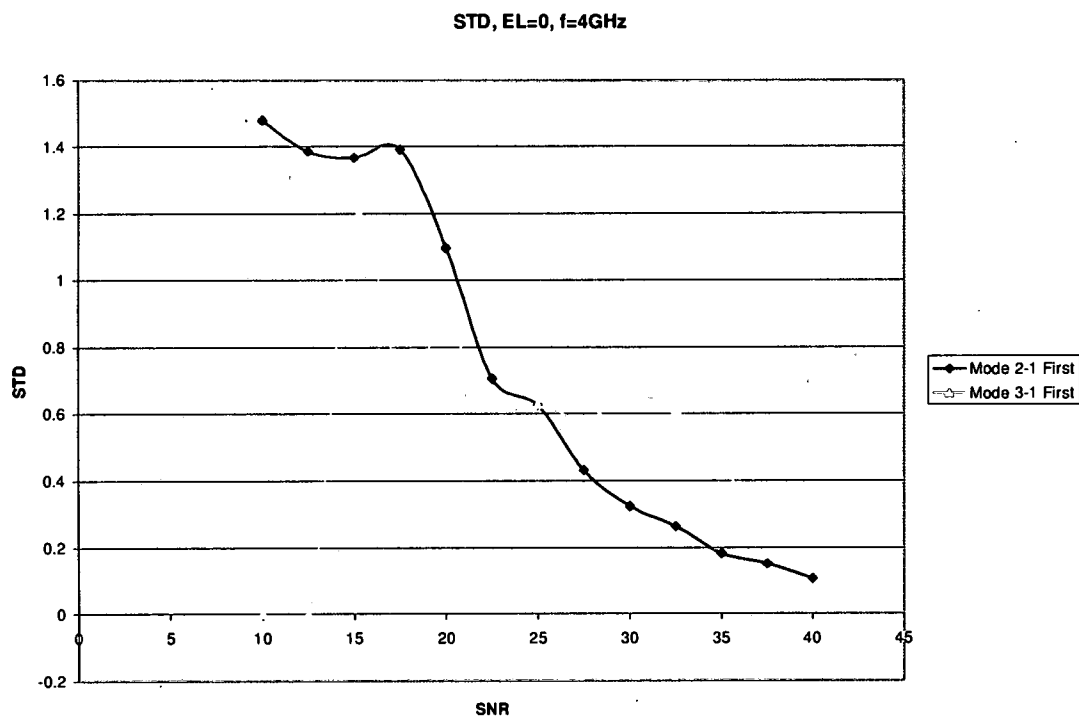


Figure 4.68: SNR vs. standard deviation for $\theta = 0^\circ$, spiral # 1, at 8GHz.

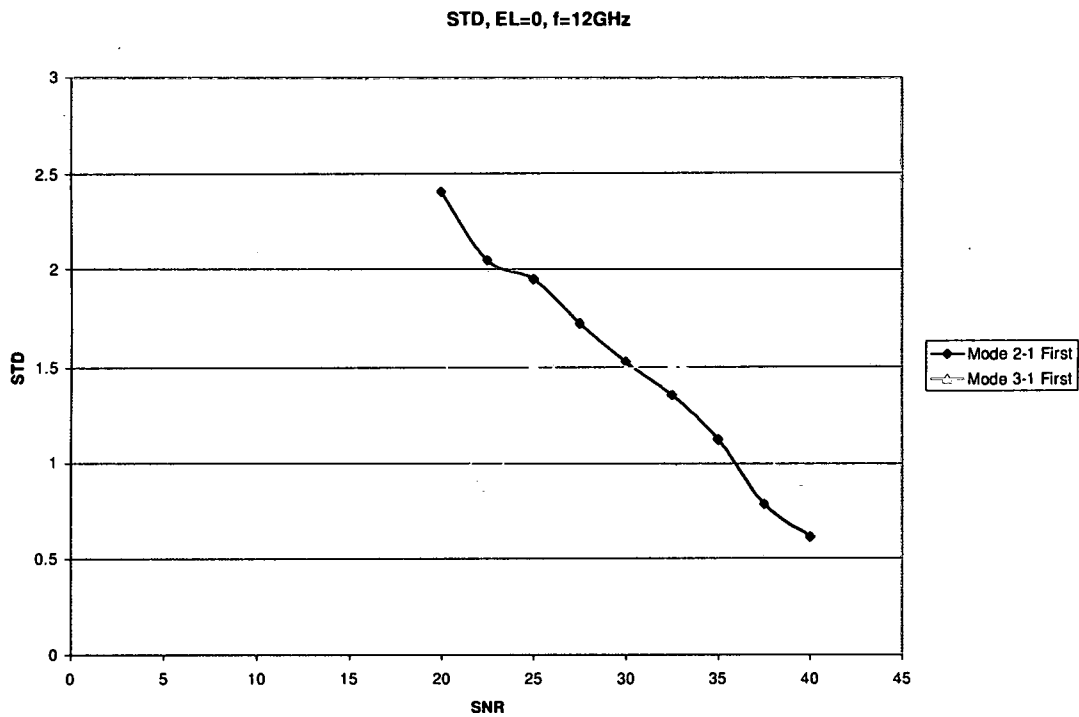


Figure 4.69: SNR vs. standard deviation for $\theta = 0^\circ$, spiral # 1, at 12GHz.

The near horizon region of space is the most difficult region for coverage as shown in chapter 2. Unlike the boresight region, there is no coverage from any mode for close to horizon elevation angle estimates, as noted theoretically in figure 2.5 and in actual pattern data in figures 3.27-3.36. Angle estimates are expected to be poor in this region. As the elevation angle approaches the horizon, the number of catastrophic failures and the standard deviation of the estimates are expected to increase. Results of catastrophic failures (figures 4.70-4.78) and standard deviation (figures 4.79-4.87) for elevation angles of $\theta = 70^\circ$, 75° , and 80° are shown for spiral # 1, each at the familiar three frequencies of 4, 8, and 12GHz, in the following figures.

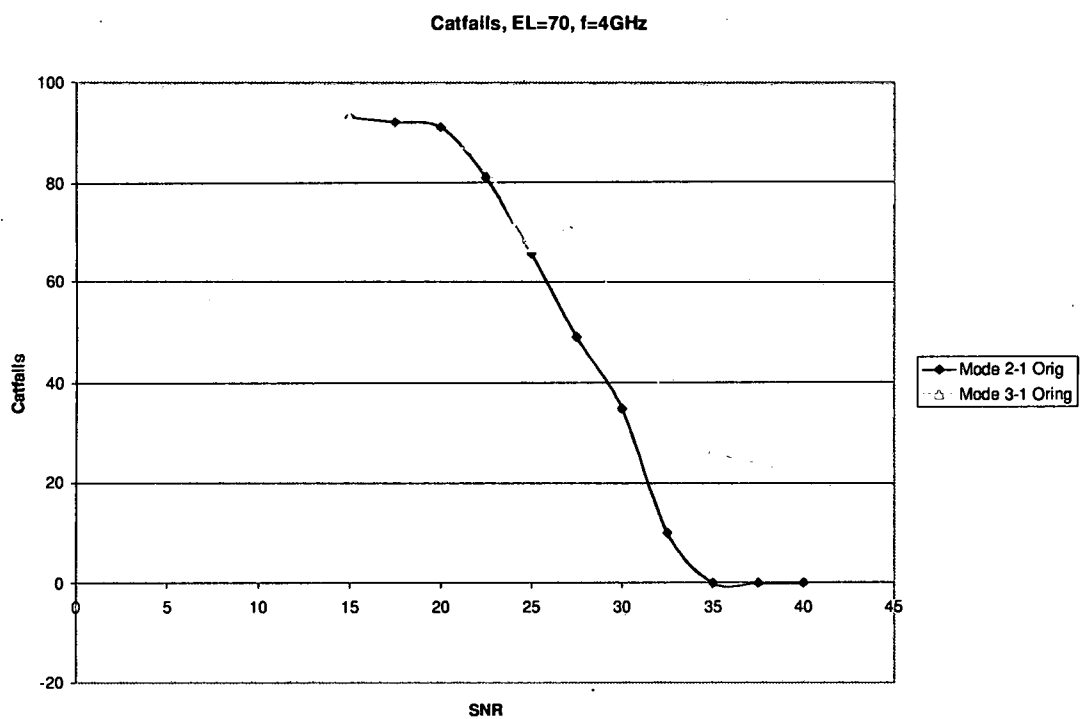


Figure 4.70: SNR vs. # of catastrophic failures for $\theta = 70^\circ$, spiral # 1, at 4GHz.

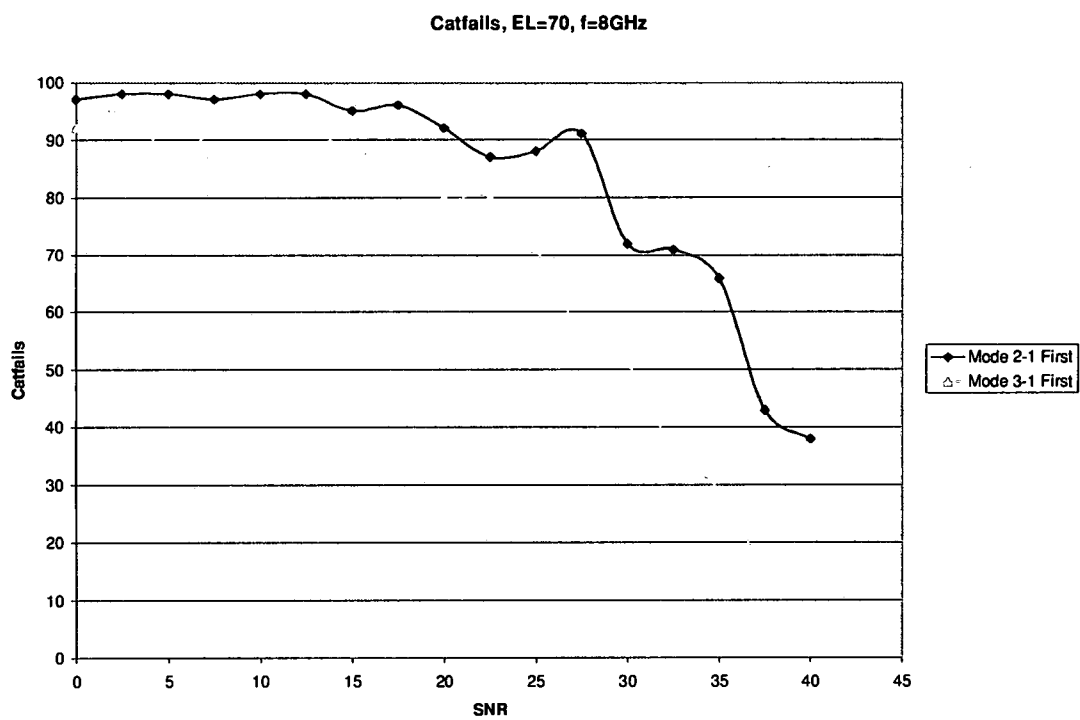


Figure 4.71: SNR vs. # of catastrophic failures for $\theta = 70^\circ$, spiral # 1, at 8GHz.

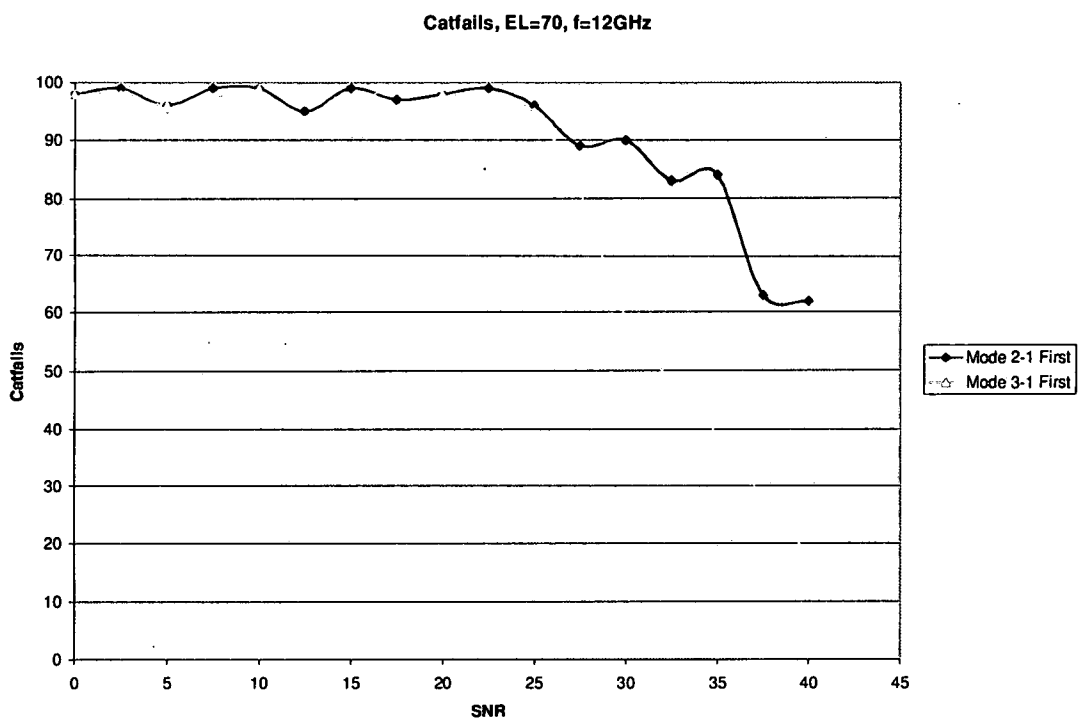


Figure 4.72: SNR vs. # of catastrophic failures for $\theta = 70^\circ$, spiral # 1, at 12GHz.

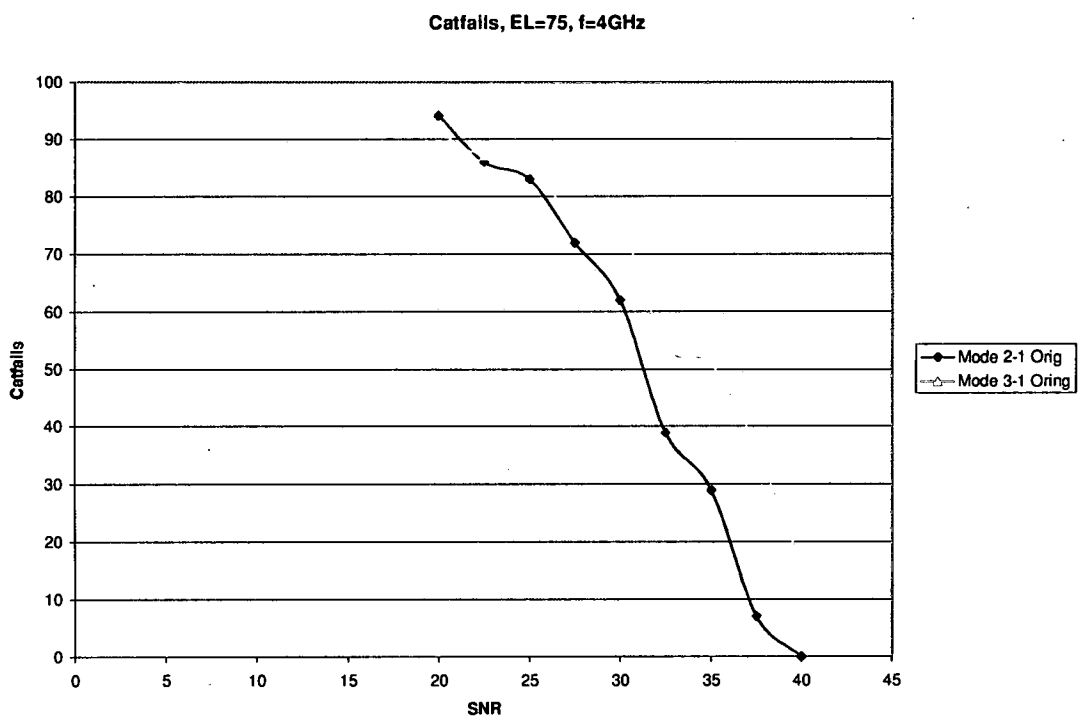


Figure 4.73: SNR vs. # of catastrophic failures for $\theta = 75^\circ$, spiral # 1, at 4GHz.

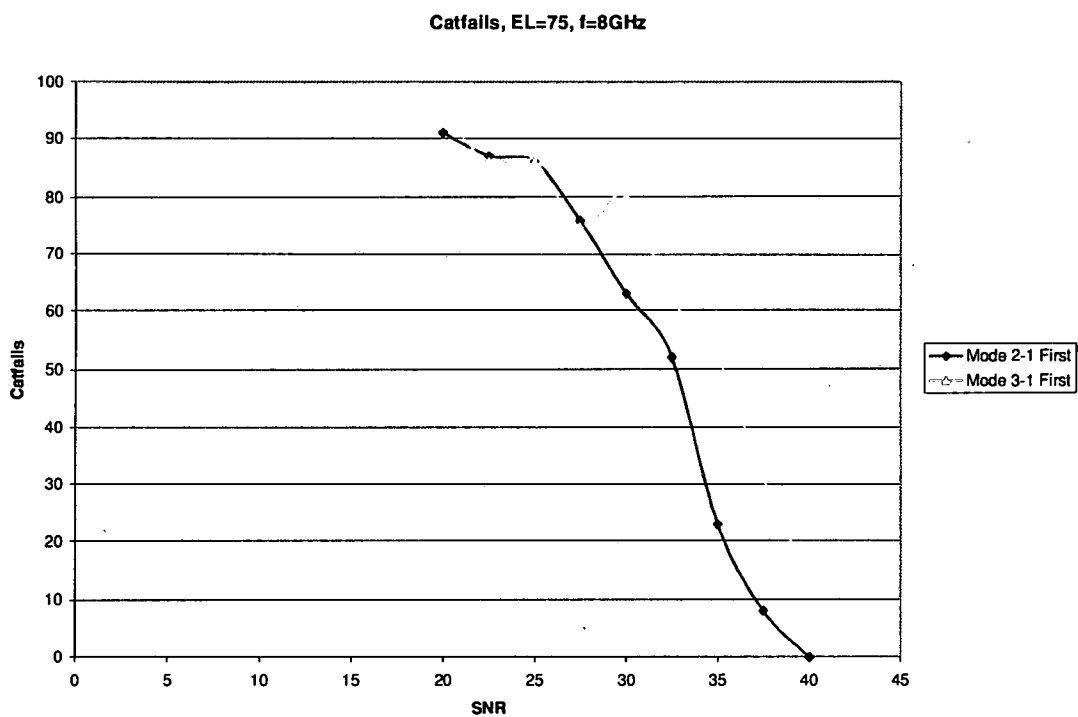


Figure 4.74: SNR vs. # of catastrophic failures for $\theta = 75^\circ$, spiral # 1, at 8GHz.

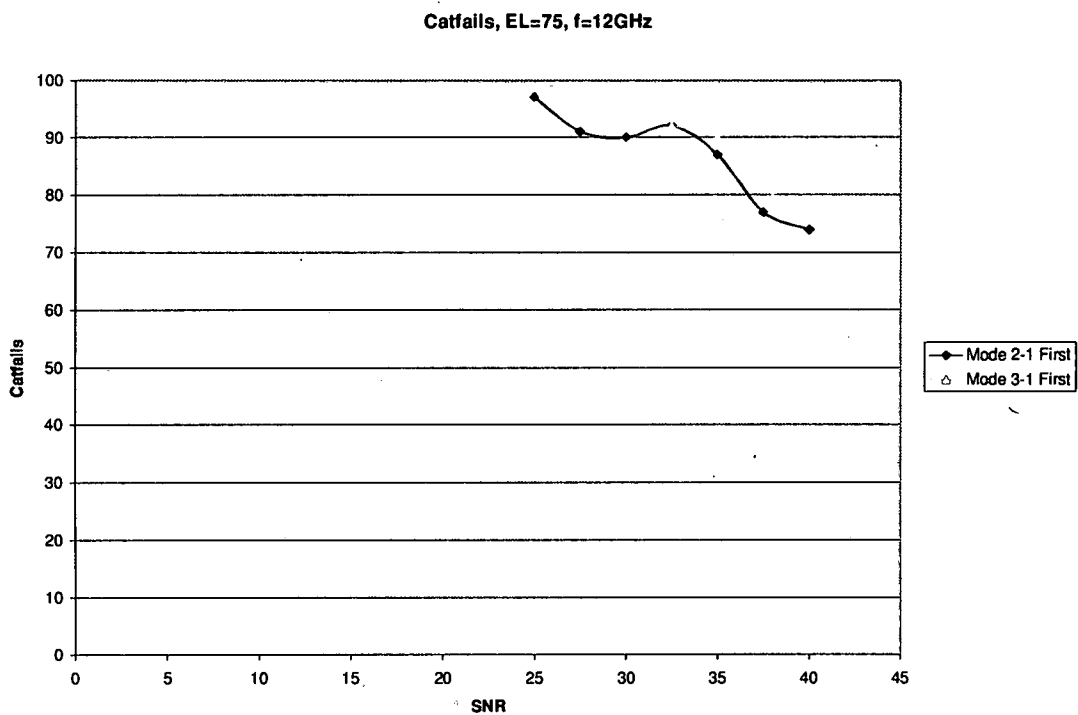


Figure 4.75: SNR vs. # of catastrophic failures for $\theta = 75^\circ$, spiral # 1, at 12GHz.

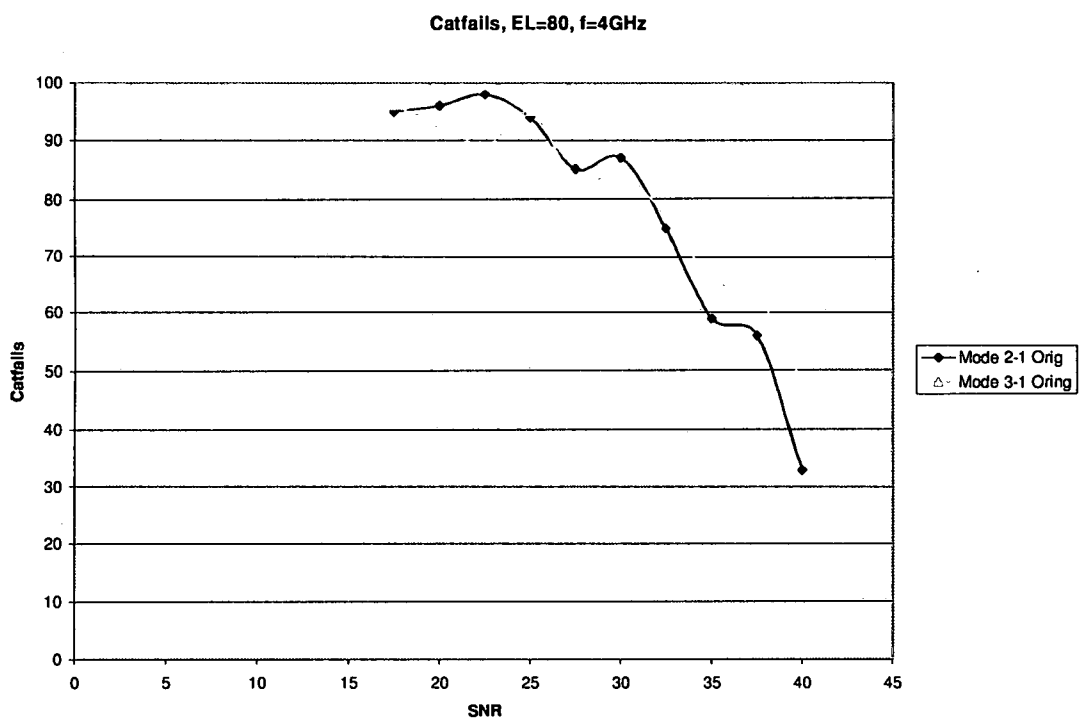


Figure 4.76: SNR vs. # of catastrophic failures for $\theta = 80^\circ$, spiral # 1, at 4GHz.

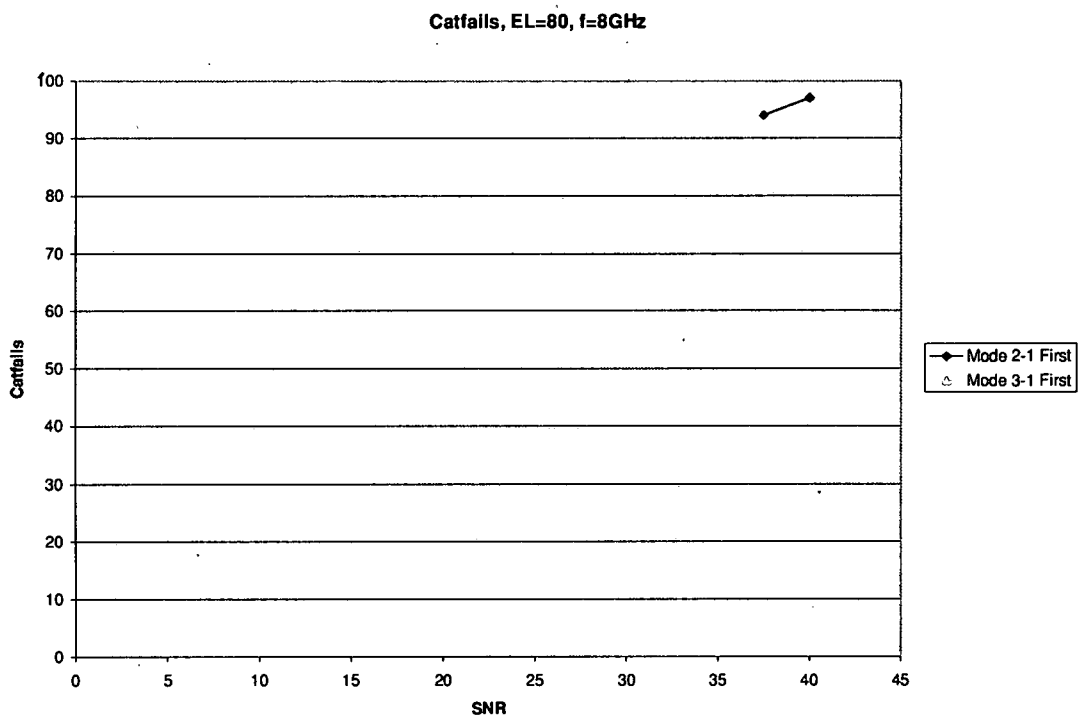


Figure 4.77: SNR vs. # of catastrophic failures for $\theta = 80^\circ$, spiral # 1, at 8GHz.

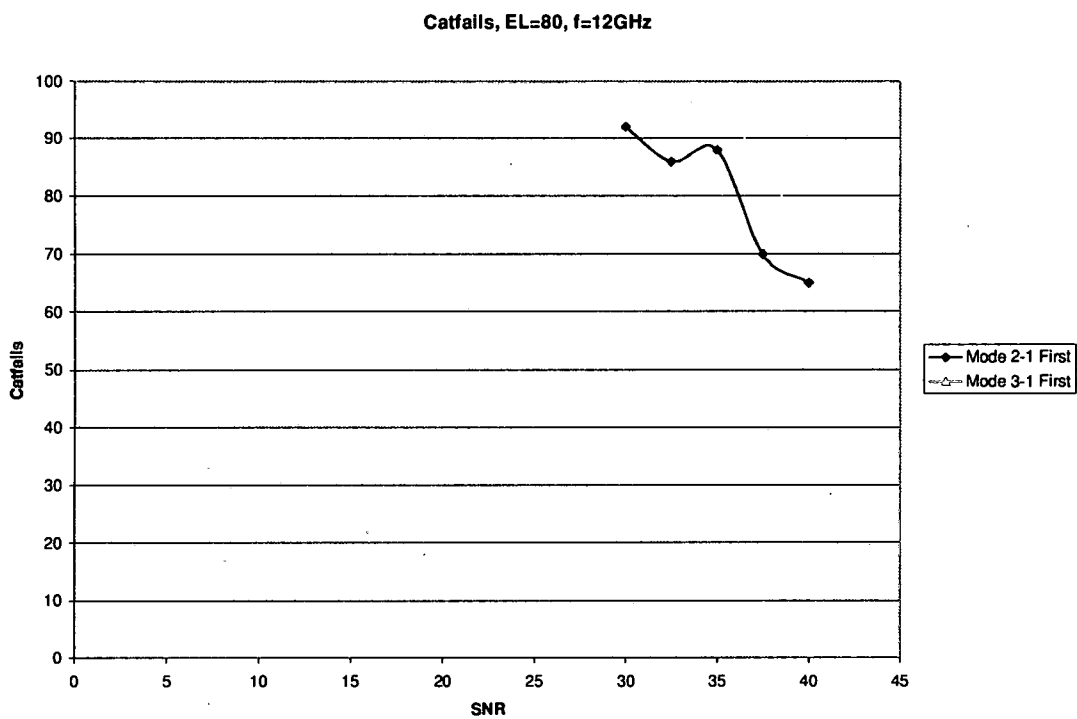


Figure 4.78: SNR vs. # of catastrophic failures for $\theta = 80^\circ$, spiral # 1, at 12GHz.

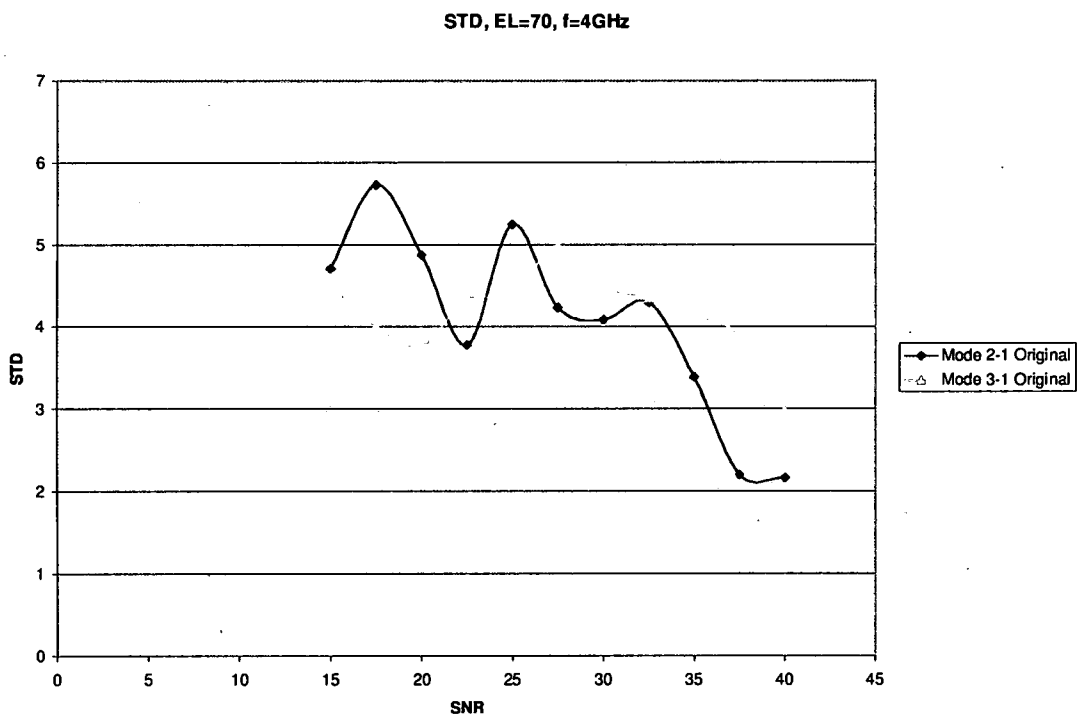


Figure 4.79: SNR vs. standard deviation for $\theta = 70^\circ$, spiral # 1, at 4GHz.

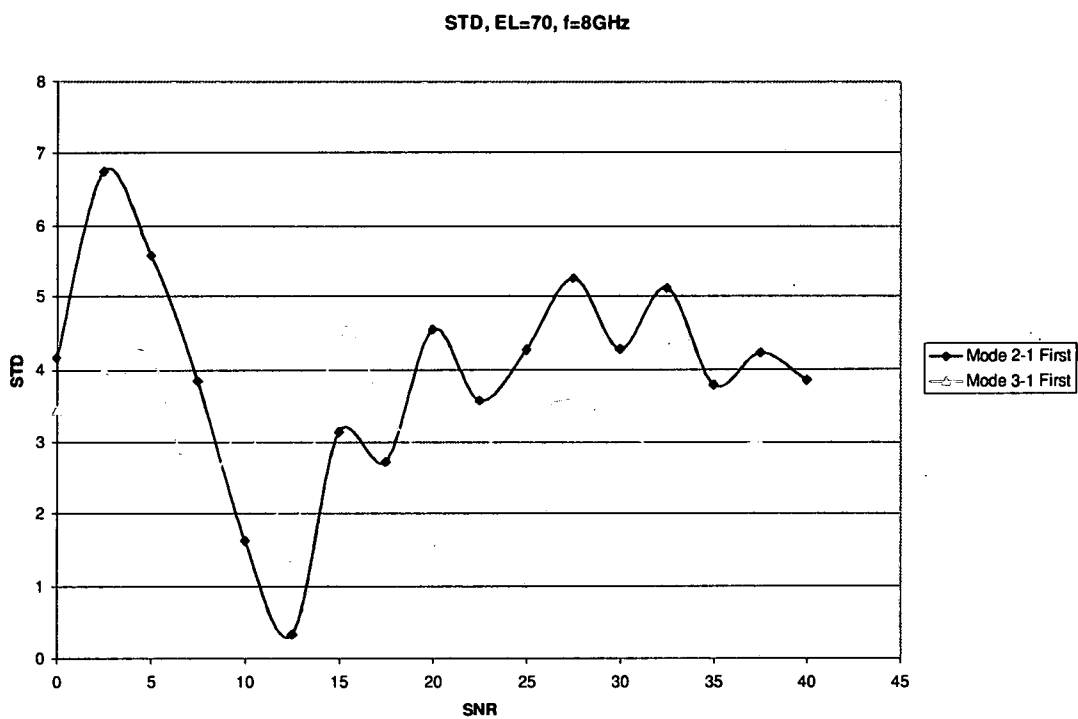


Figure 4.80: SNR vs. standard deviation for $\theta = 70^\circ$, spiral # 1, at 8GHz.

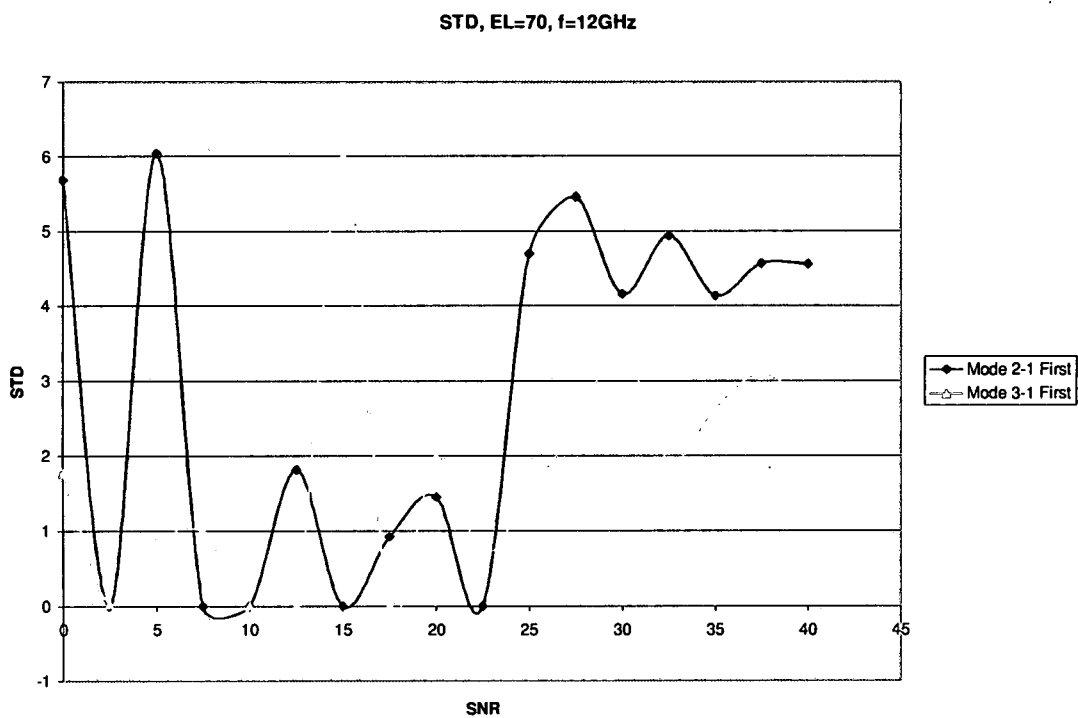


Figure 4.81: SNR vs. standard deviation for $\theta = 70^\circ$, spiral # 1, at 12GHz.

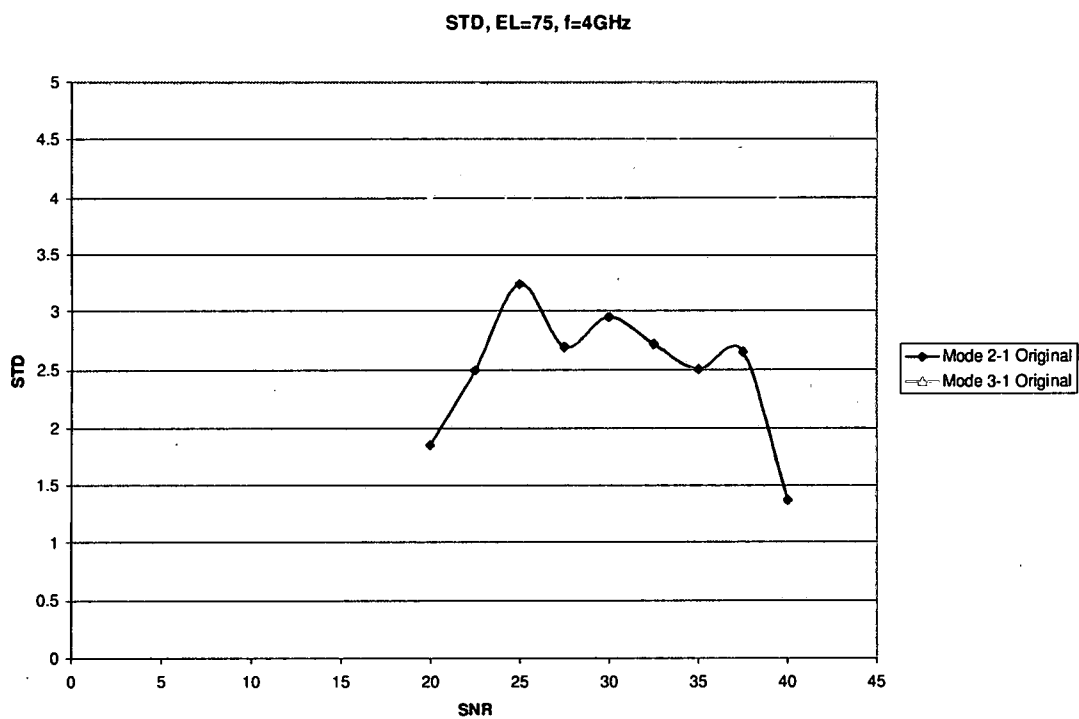


Figure 4.82: SNR vs. standard deviation for $\theta = 75^\circ$, spiral # 1, at 4GHz.

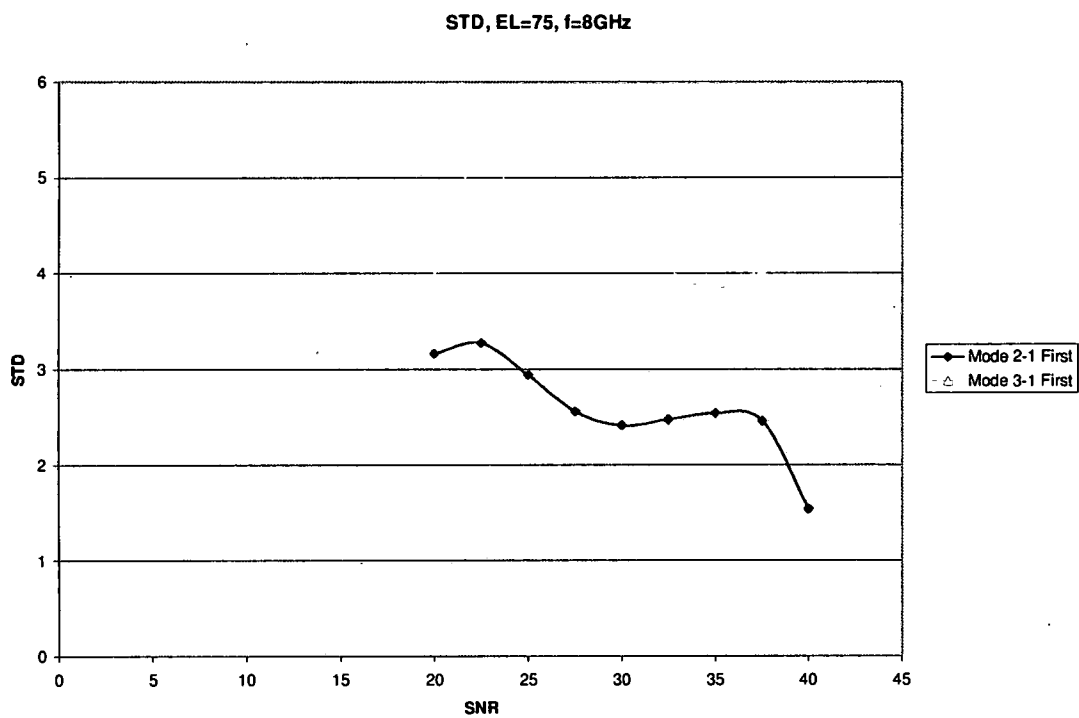


Figure 4.83: SNR vs. standard deviation for $\theta = 75^\circ$, spiral # 1, at 8GHz.

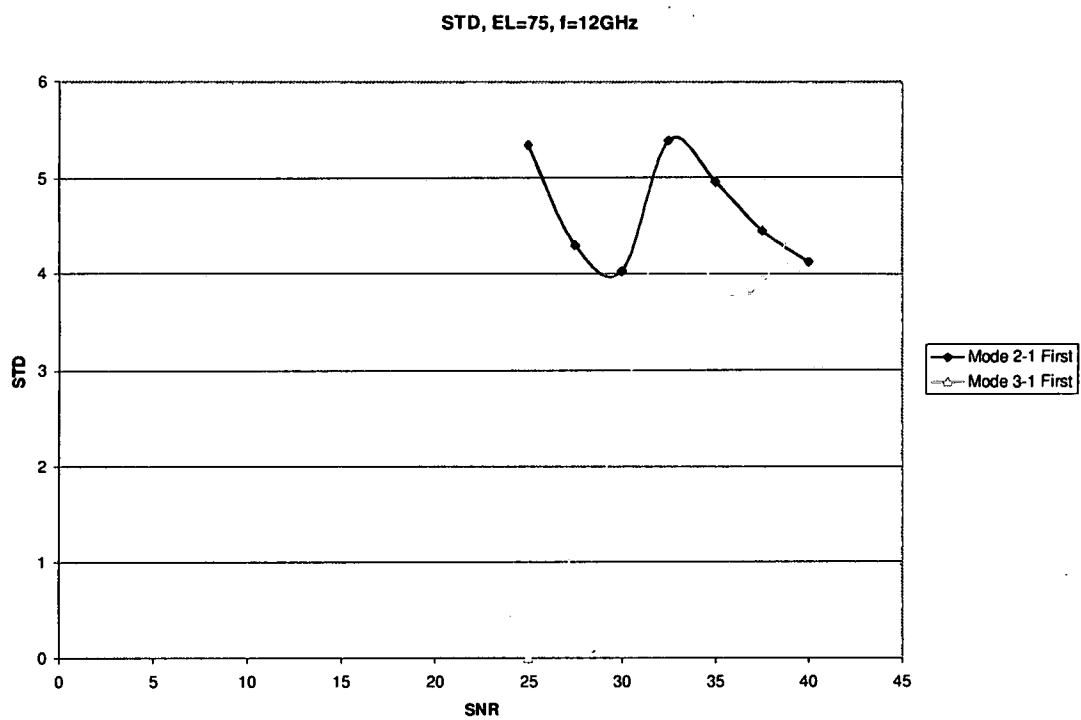


Figure 4.84: SNR vs. standard deviation for $\theta = 75^\circ$, spiral # 1, at 12GHz.

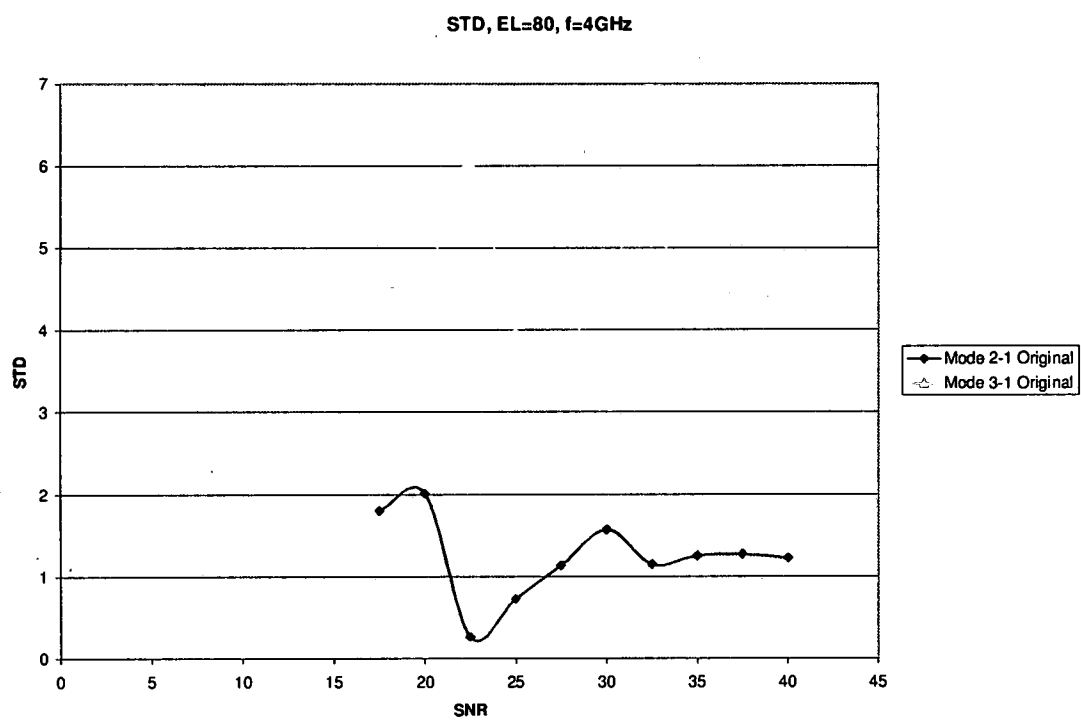


Figure 4.85: SNR vs. standard deviation for $\theta = 80^\circ$, spiral # 1, at 4GHz.

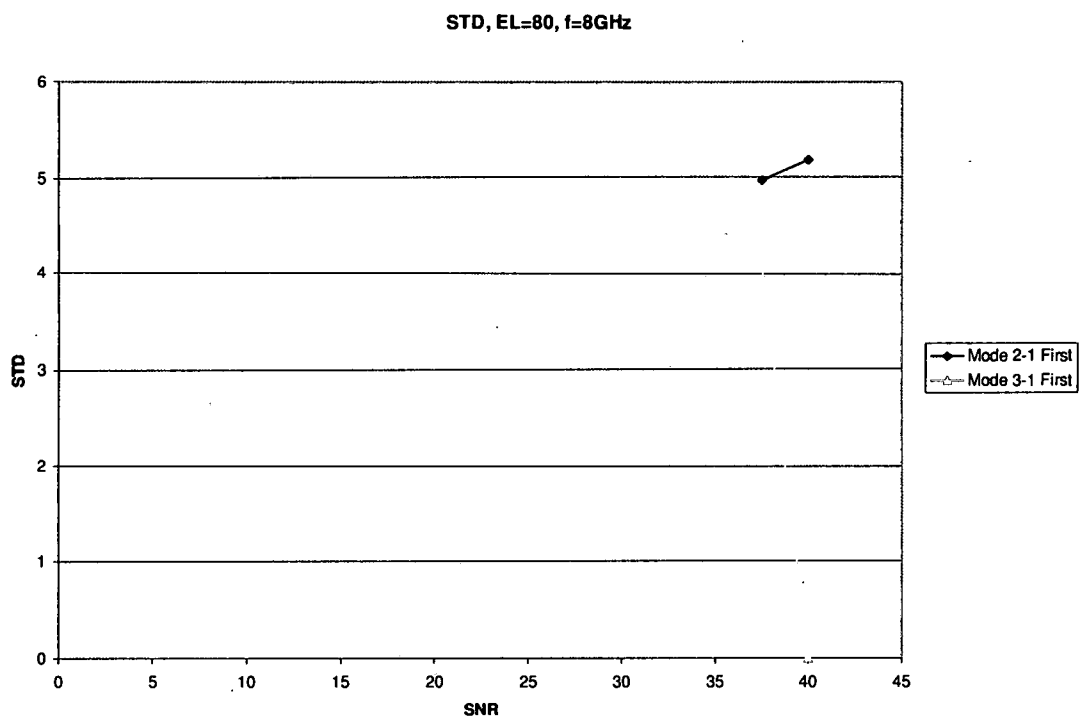


Figure 4.86: SNR vs. standard deviation for $\theta = 80^\circ$, spiral # 1, at 8GHz.

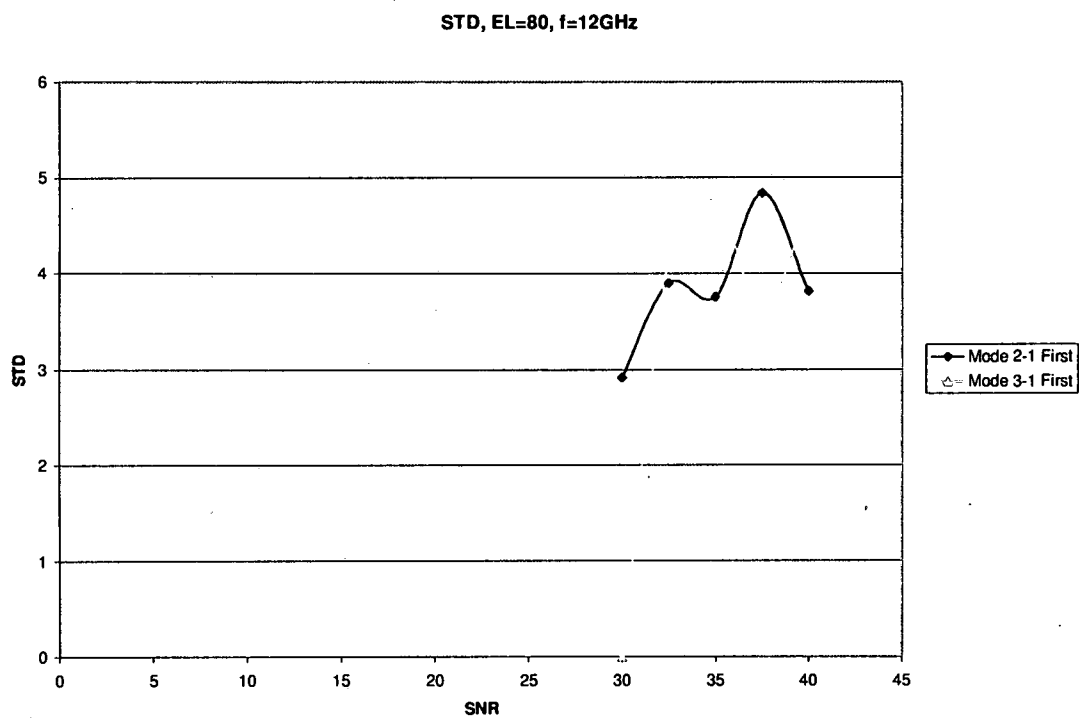


Figure 4.87: SNR vs. standard deviation for $\theta = 80^\circ$, spiral # 1, at 12GHz.

From an examination of the experimental catastrophic failure and standard deviation results presented in figures 4.70-4.87 for the main elevation pattern coverage area, the following observations can be made:

- As frequency increases within each specific elevation angle investigated, the number of catastrophic failures increase and the standard deviation increases.
- As the elevation angle under investigation increases from $\theta = 70^\circ$ to $\theta = 80^\circ$, the number of catastrophic failures present skyrocket—an SNR of 40dB is required just to prohibit the catastrophic failures ratio from exceeding 50% at $\theta = 80^\circ$.
- As the elevation angle under investigation increases from $\theta = 70^\circ$ to $\theta = 80^\circ$, the standard deviation increases dramatically and is greater than 6° for SNR values less than the norm of 20dB for $\theta = 75^\circ$ and 80° .

CHAPTER V

CONCLUSIONS

The goal of this work is to validate, by actual measurements, the angle estimation performance of a four-arm spiral antenna using the “comparison” method. Chapter 3 presented the measurement range setup and the extensive wideband measurement data for two four-arm spiral antennas and the associated modeformer. These measurements were carried out in a compact range, which illuminates the antenna under test with a plane wave via a parabolic reflector as shown in figure 3.1(b). The spiral antennas were measured using a patented phase-stationary test body. A test body enhances the integrity of antenna measurements by evaluating performance in an appropriate conformal environment. The “almond” shaped test body incorporates a positioning system which provides a phase-stationary antenna aperture center under rotation of both azimuth and elevation. This fixed phase center of antennas under test allows for salient phase data acquisition in azimuth—a trait essential for accurate azimuth angle estimation. It is worthy to note that the phase reference is ever changing from measurement to measurement and mode to mode as evident in the azimuth phase data of figures 3.5-3.25. The difference in phase reference between measurements depicts the need for calibration (or phase compensation) as mentioned in section 2.1.3 and section 4.1.

With the goal of demonstrating the capability of the multi-arm spiral antenna to provide estimates of both azimuth and elevation angles of incident radiation, the following measurements are carried out:

- The outputs of mode 1, 2, and 3 are measured as functions of azimuth for elevations angles of $\theta = 20^\circ$, 40° , and 45° , and at three different frequencies of 4, 8, and 12GHz. The best elevation angle estimates are expected to be in the range of $\theta = 20^\circ$ - 50° , the modal main beam coverage area, and hence the measurements

were carried out for $\theta = 20^\circ$, 40° , and 45° . The spiral antenna was designed to operate over a frequency range of 2-18 GHz. It is hoped that measurements carried out at 4, 8, and 12GHz help characterize the performance of AoA estimation over the core of this band.

- Measurements for evaluating elevation angle estimates are also carried out for mode 1, 2, and 3 at the same three frequencies of 4, 8, and 12GHz. The elevation measurements are carried out over the x-z plane defined by $\phi = 0$ (for $x \geq 0$) and $\phi = \pi$ (for $x \leq 0$).

A careful study of the measurements carried out to assess the azimuth angle estimation capabilities reveals the following:

- The gain of the three modes is relatively invariant with azimuth, as expected, for all elevation angles and over the whole band. However, a significant amount of ripple is observable in the mode 3 output at the lower end of the band (4 GHz) and in the mode 1 output at the higher end of the band (12 GHz). This could be explained as follows: the active region corresponding to mode 3 has a circumference of 3λ and as this active region approaches the outermost edge of the antenna at the lower end of the band causing imperfections in the active region resulting in the observed ripple. At the higher end of the band, the active region corresponding to mode 1 has a circumference of 1λ approaches the feed region resulting in the observed ripple. This observed ripple, especially in the phase variation, does result in azimuth angle estimation errors.

An examination of the measurements carried out to assess the elevation angle estimation capabilities reveals the following:

- By virtue of symmetry, theory requires that elevation patterns be symmetric. However, the actual measured data in the $\phi = 0$ and $\phi = \pi$ semi-infinite planes are noticeably asymmetrical. This lack of symmetry requires that, two separate polynomials must be determined to fit the measured data in the two semi-infinite

planes. Indeed, symmetry requires that elevation patterns be independent of the azimuth; practical limitations limit the symmetry realized and the elevation patterns are not necessarily independent of azimuth.

- The higher the frequency, the greater the asymmetry and the ripple in elevation patterns.
- The unit to unit variations in elevation patterns and modal ratios are evident and point to the need for calibration.
- It is readily discernible that for elevation angles near horizon (i.e., $\theta \approx 90^\circ$), angle estimates will be highly unreliable.
- For elevation angles near boresight (i.e., $\theta \approx 0^\circ$), the modal ratio is close to zero. Receiver noise, therefore, significantly affects elevation angle estimates near the zenith (boresight).

The measured data is processed, calibrated, and used to determine the AoA estimates and compared to the true values. From the results of this process, we may draw the following conclusions:

- The coverage provided by the various modes plays an important role in the accuracy of the AoA estimates. Mode 1 gives good coverage near boresight in the elevation range of 0° - 30° , approximately, resulting in good angles estimates. However, in the $>30^\circ$ range, mode 1 does not give very good estimates, but nevertheless must be used to resolve the ambiguous estimates provided by higher-order modes. Mode 2 and 3 and beyond have very poor coverage near the zenith; in this region, approximately 0° - 30° , it is best to use merely the mode 1 estimate and ignore the rest of the modal outputs.
- Near the horizon, say in the elevation range of 60° - 90° , none of the modes provide meaningful coverage and AoA estimates are unreliable.
- In the 30° - 60° range, higher order modes do provide good coverage, but must rely on the relatively poor azimuth estimates provided by mode 1 to resolve the ambiguities of the AoA estimates provided by the higher order modes.

- The elevation angle estimates are unreliable near the horizon, just as in the case of azimuth estimates—near the zenith, the higher order modal outputs are relatively small, making the modal output ratios near zero. As a result, a relatively small amount of thermal noise can result in a large error in the angle estimates provided. Reasonable estimates near boresight can be obtained if the Signal-to-noise ratio is high enough. Reasonable elevation angle estimates can be obtained for elevation angles in the range of 20°-60°.
- The measured data clearly indicates that as frequency increases, the quality of angle estimates deteriorates. As the frequency increases, the active region on the spiral antenna moves towards the feed region. Thus, any small asymmetries in the feed region can significantly impact the radiation patterns. Interestingly, it is mode 1 that is more significantly affected at higher frequencies than the higher order modes. At the low end of the frequency band, it is the higher modes, mode 3 in this case, that are more affected as the active region moves outward and the active region of the higher order modes that reach the outer edge of the antenna first. Indeed, the measurements clearly show this effect. These inconsistencies may be minimized or even eliminated by imposing a stricter regime of manufacturing tolerances on the antenna. Yet another reason for the deterioration of the estimates at higher frequencies could be due to the change in the behavior of the modeformer with frequency. Strictly speaking, the modeformer should be properly characterized across the band and this information must be then used to 'correct' or 'compensate' the actual measurements so that the imperfections in the modeformer performance are removed.

Research in this area can and should be pursued in a number of different directions:

- Characterization of the modeformer mentioned above and improving the AoA estimation performance across the frequency band.
- Currently, the phase reference for the measurement of each modal output is different. It would be very desirable to devise a measurement technique that makes it possible to measure all the modal outputs with the same phase reference.

- Only the comparison method was used to obtain the AoA estimates here; however, it has been demonstrated that a number of modern parameter estimation techniques may also be used to obtain AoA estimates. It would be useful to demonstrate the efficiency of these methods by validating with experimental data.
- A 'hybrid' multi-arm spiral and interferometer configuration may be used to improve upon the AoA estimates. Exploration and validation of such techniques would be a very desirable addition to the existing body of knowledge.

Bibliography

1. Jacobs, E., and Ralston, E.W., "Ambiguity resolution in Interferometry", *IEEE Transactions on Aerospace and Electronic Systems*, AES-17, 6 (November 1981).
2. Johnson, D.H., and Dudgeon, D.E., *Array Signal Processing*, Englewood Cliffs, NJ: Prentice Hall, 1993.
3. Compton, R.T., "Adaptive Maximum Likelihood Angle Estimate Bias with a Monopulse Antenna under Ideal Conditions," Technical Report 95-5-4, WPAFB, OH, 1995.
4. Thierrien, C.W., *Discrete Random Signals and Statistical Signal Processing*, Englewood Cliffs, NJ: Prentice Hall, 1992.
5. Penno, R.P. and Pasala, K., "A Theory of Angle Estimation Using a Multi-arm Spiral Antenna", *IEEE Transactions on Aerospace and Electronics Systems*, 37, 1 (January 2001), 123-133.
6. Rumsey, V.H., *Frequency Independent Antennas*, Academic Press, New York & London: 1966.
7. Dyson, J.D., "The Equiangular Spiral Antenna," *IRE Transaction on Antennas and Propagation*, AP-7 (April 1959), 181-187.
8. Dyson, J.D., "The Unidirectional Equiangular Spiral," *IRE Transaction on Antennas and Propagation*, AP-7 (October 1959), 329-334.
9. Cheo, b. R.S., Rumseey, V.H., and Welch, W.J., "A Solution to the Frequency-Independent Antenna Problem," *IRE Transaction on Antennas and Propagation*, AP-9 (November 1961), 527-534.
10. Burdine, B.H., "The Spiral Antenna," Technical Report 2, MIT, 15 April 1955.
11. Curtis, W.L., "Spiral Antennas," *IRE Transaction on Antennas and Propagation*, AP-8 (May 1960), 298-306.
12. Kaiser, J.A., "The Archimedean Two-Wire Spiral Antenna," *IRE Transaction on Antennas and Propagation*, AP-8 (May 1960), 312-323.
13. Corzine, R.G., and Mosko, J.A., *Four-Arm Spiral Antennas*, Norwood, MA: Artech House, 1990.
14. Thiele, G.A., and Stutzman, W.L., *Antenna Theory and Design 2nd Edition*, New York: Wiley & Sons, 1998.

15. Pasala, K., and Penno, R.P., "An Emitter Location Estimator for Evaluation of Different Direction Finding Techniques," Technical Report AFRL-TR-1999-1085, WPAFB, OH, 1998.
16. Adamy, David, *EW 101*, Boston: Artech House, 2001.
17. Schneider, S.W., Penno, R.P., Pasala, K., and Kempel, L., "New Ways to Locate A Threat," *Aircraft Survivability*, Fall 2003, pp. 31-35.
18. Shamansky, H., Dominek, A., Schneider, S.W., Hughes, J., and Breaks, J., "A Phase-Stationary High Performance Antenna Test Body," *Antenna Measurement Techniques Association (AMTA) Annual Symposium proceedings*, 1995.
19. Pasala, K., Penno, R.P., Schneider, S., "Novel Wideband Multimode Hybrid Interferometer System," *IEEE Transactions on Aerospace and Electronics Systems*, 39, 4 (October 2003), 1396-1406.

R002592483

HECKMAN

BINDERY, INC

T 024891 E 6 00



1/19/2006